Doklady Physics, Vol. 50, No. 12, 2005, pp. 619–622. Translated from Doklady Akademii Nauk, Vol. 405, No. 4, 2005, pp. 471–474.

PHYSICS

Radiation of a Symmetric Electric Vibrator Excited by Ultrashort Pulses of the Shape Described by an Atomic Function

M. A. Basarab*, V. F. Kravchenko, and Corresponding Member of the RAS I. B. Fedorov***

Received July 19, 2005

INTRODUCTION

Atomic functions [1, 2] have recently been actively exploited in studies of the ultra-wideband processes of antenna technology [3–5]. In the present paper, we have investigated for the first time properties of a symmetric vibrator excited by ultrashort electric-current pulses whose shape corresponds to an atomic function. For two excitation modes, namely, the traveling-wave regime and the uniform distribution, it is shown that under certain conditions the directivity pattern of ultra-wideband radiators by analogy with the narrow-band case is similar to the derivative of the current distribution.

INITIAL RELATIONSHIPS. THE TRAVELING-WAVE DISTRIBUTION

We consider a symmetric infinitely thin perfectly conducting electric vibrator with a branch length L and with an infinitely small distance between the vibrator shoulders at the feeding point O. We also assume that the vibrator branches are formed by N elementary radiators of the size $\Delta L = \frac{L}{N}$ with the coordinates $L_j = \frac{j + 1/2}{\Delta L}$.

Let an electric-current pulse $J(t)$ be excited in accordance with a certain time law at the point O. Further, the pulse propagates along the vibrator z axis at the velocity c of light (traveling-wave mode). The radiation field of an elementary vibrator segment in the far-field region can be written out in the form

$$E_j(t, \theta) = \frac{Z_0 \sin\theta d}{4\pi r c} \frac{d}{dt} J\left(t - \frac{r}{c} - \frac{L_j}{c}(1 - \cos\theta)\right)\Delta L, \quad (1)$$

where Z_0 is the characteristic impedance of the free space, r is the distance to the far-field region, and θ is the angle between the directions to the observation point and the antenna center. The resulting radiation field is obtained by summing fields (1) excited by elementary radiator segments:

$$E_\Sigma(t, \theta) = \sum_{j=0}^{N-1} E_j(t, \theta)$$

$$= \frac{Z_0 \sin\theta}{4\pi r c} \sum_{j=0}^{N-1} \frac{d}{dt} J\left(t - \frac{r}{c} - \frac{L_j}{c}(1 - \cos\theta)\right)\Delta L. \quad (2)$$

In the limiting case as $N \longrightarrow \infty$, sum (2) transforms into the integral

$$E_\Sigma(t, \theta) = \frac{Z_0 \sin\theta}{4\pi r c} \int_0^L \frac{d}{dt} J\left(t - \frac{r}{c} - \frac{z}{c}(1 - \cos\theta)\right) dz, \quad (3)$$

whence it follows

$$E_\Sigma(t, \theta) = \frac{Z_0 \sin\theta}{4\pi r(1 - \cos\theta)}$$

$$\times \left[J\left(t - \frac{r}{c}\right) - J\left(t - \frac{r}{c} - \frac{L}{c}(1 - \cos\theta)\right)\right]. \quad (4)$$

Usually, a classic distribution (Gaussian, triangular, etc.) is chosen for the function $J(t)$ [6–8]. Here, we can distinguish two ultimate cases: $L \ll c\tau$ and $L \gg c\tau$, in which the parameter τ characterizes the effective pulse duration. For $L \ll c\tau$ (long-wave case), the interference of elementary fields (2), (3) results in the fact that the field $E_\Sigma(t, \theta)$ turns out to be similar to the derivative of the electric-current $J(t)$. This is clearly seen from rela-

* *Moscow State Technical University, Vtoraya Baumanskaya ul. 5, Moscow, 107005 Russia*

** *Institute of Radio Engineering and Electronics, Russian Academy of Sciences, Building 7, ul. Mokhovaya 18, Moscow, 125061 Russia*
e-mail: bmic@mail.ru; kvf@pochta.ru

1028-3358/05/5012-0619$26.00

tionship (4) since, at small values of the ratio $\frac{L}{c}$, the expression entering into the square brackets approximates with an accuracy to a certain constant the first derivative. In the second ultra-wideband case ($L \gg c\tau$), the resulting field $E_\Sigma(t, \theta)$ can be represented as a sum of two fields whose shapes are similar to that of the initial pulse excited at the initial instant of the current-pulse formation and at the instant of its absorption at the vibrator end.

THE CURRENT PULSE IN THE FORM OF AN ATOMIC FUNCTION $h_a(t)$

For $L \gg c\tau$, the difference in square brackets of relationship (4) is equal to the first derivative of a certain function $J_1(t)$:

$$\left[J\left(t-\frac{r}{c}\right)-J\left(t-\frac{r}{c}-\frac{L}{c}(1-\cos\theta)\right)\right] \sim J_1'\left(t-\frac{r}{c}-\frac{L}{2c}(1-\cos\theta)\right), \quad (5)$$

which corresponds to the initial current pulse of the longer duration $\tau_1 \geq \tau$.

We now find the distribution $J(t)$ for which

$$J_1(t) \sim J\left(\frac{t}{a}\right), \quad (6)$$

i.e., the field $E_\Sigma(t, \theta)$ with a certain extension coefficient a, as in the case of $L \ll c\tau$, is similar to the first derivative of the exciting pulse. This problem has a nonunique solution, and for $J(t)$, we may choose an arbitrary atomic function $h_a(t)$ ($a > 1$) [1, 2]. Indeed, the given functions are finite within the interval $|t| < \frac{1}{a-1}$; they belong to the class $C^\infty(\mathbb{R})$ and are the solutions to the functional-differential equations

$$h_a'(t) = \frac{a^2}{2}[h_a(at+1) - h_a(at-1)]. \quad (7)$$

The Fourier transformation for $h_a(t)$ has the explicit form

$$\hat{h}_a(p) = \prod_{i=1}^{\infty} \operatorname{sinc}\frac{p}{a^j}, \quad (8)$$

where $\operatorname{sinc} p \equiv \frac{\sin p}{p}$.

We now assume that

$$\frac{L}{c\tau}(1-\cos\theta) = 2. \quad (9)$$

Then, after replacing into (4) the relationship

$$J(t) = h_a\left(\frac{t}{\tau}\right), \quad (10)$$

we arrive at

$$E_\Sigma(t, \theta) = \frac{Z_0 \sin\theta}{4\pi r(1-\cos\theta)}\left[h_a\left(\frac{t-\frac{r}{c}}{\tau}\right) - h_a\left(\frac{t-\frac{r}{c}}{\tau}-2\right)\right]. \quad (11)$$

With due account for (7), relation (11) implies

$$E_\Sigma(t, \theta) = \frac{Z_0 \sin\theta}{4\pi rc}\frac{1}{a}h_a'\left(\frac{t-\frac{r}{c}-\tau}{a\tau}\right)L. \quad (12)$$

Comparing expressions (12) and (1), we can show that the function $J_1(t)$ entering into (5) and (6) should be of the form

$$J_1(t) = \frac{1}{a}h_a\left(\frac{t}{a\tau}\right). \quad (13)$$

Under the validity of condition (9), the radiation field along the direction $\theta \sim 90°$ in the far-field region is excited by current pulse (10) of the duration $\frac{2\tau}{a-1}$, which propagates along the vibrator, and turns out to be similar to this pulse. Moreover, this field coincides with that excited by the analogous scaling pulse (13) of duration $\frac{2a\tau}{a-1}$. As in the case $L \ll c\tau$, the radiation field is equal to the pulse first derivative. The inverse statement is also true: the long-wave vibrator field is similar to the first derivative of the exciting pulse of the shape given by the atomic function and can be considered as a sum of two fields reiterating the shape of the pulse compressed by a times.

We now consider the electric-current distribution, assuming it to be uniform over the longitudinal coordinate z. In this case, as opposed to the traveling-wave mode, the fields in the far-field region of an elementary vibrator and of the entire radiator [7] are of the form

$$E_j(t, \theta) = \frac{Z_0 \sin\theta}{4\pi rc}\frac{d}{dt}J\left(t-\frac{r}{c}+\frac{L_j}{c}\cos\theta\right)\Delta L, \quad (14)$$

$$E_\Sigma(t, \theta) = \frac{Z_0 \tan\theta}{4\pi r}\left[J\left(t-\frac{r}{c}+\frac{L}{c}\cos\theta\right)-J\left(t-\frac{r}{c}\right)\right]. \quad (15)$$

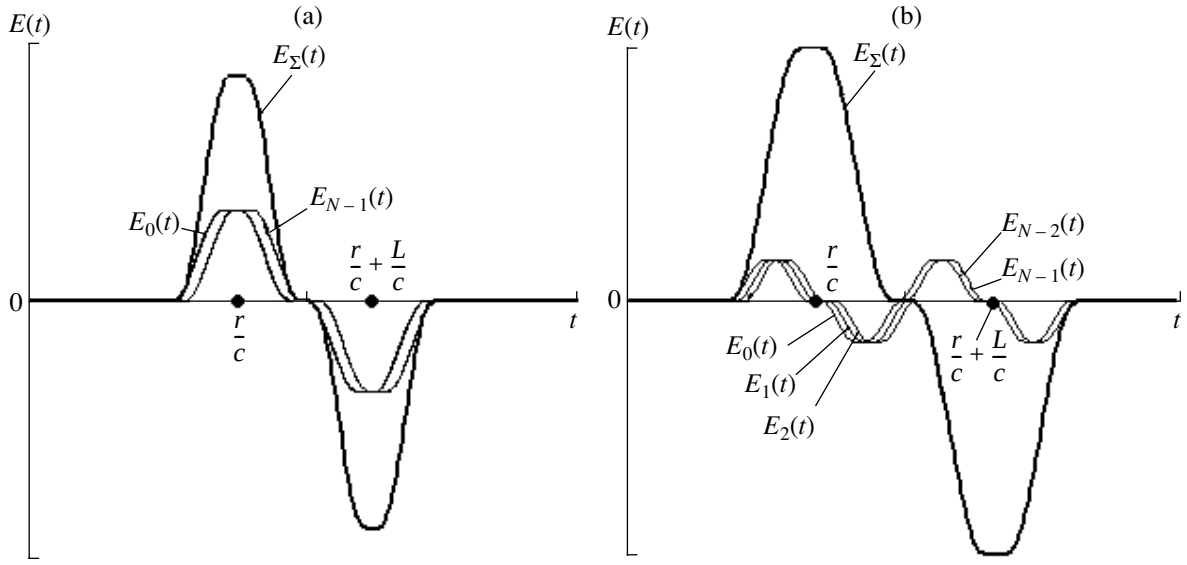

Fig. 1. Radiation field in the far-field region along the direction $\theta = 90°$: (a) $L \ll c\tau$ and (b) $L = 2c\tau$.

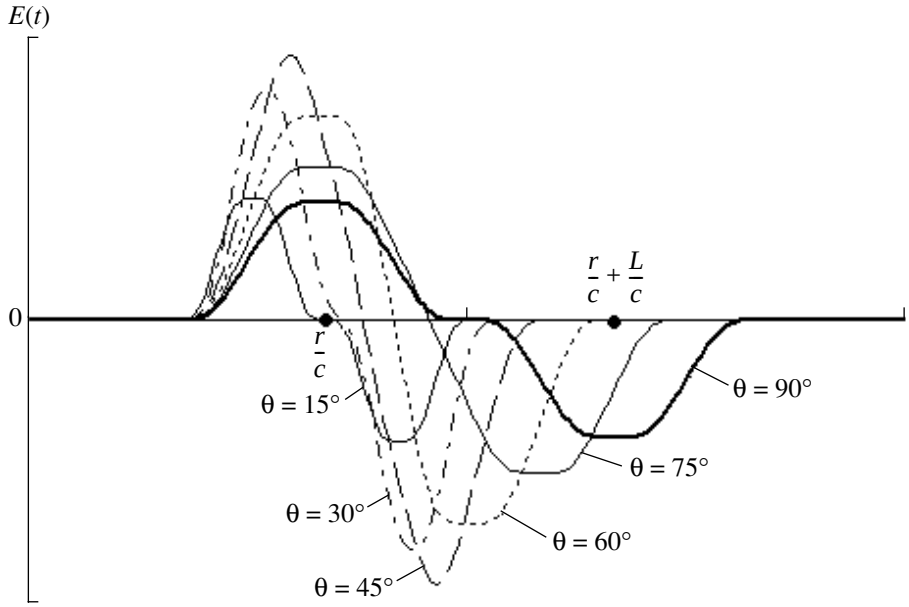

Fig. 2. Radiation field in the far-field region for $L = 2c\tau$ and different observation angles θ.

Independently of the vibrator length, for angles θ close to 90°, the field E_Σ reiterates the shape of the current derivative. As the angle θ tends to zero and for arbitrary functions $J(t)$, directivity pattern (15) is similar to the first derivative of the current only in the ultra-wideband case ($L \ll c\tau$). The exception is the distribution $J(t)$ in the form of atomic function (10). In this case, under the condition

$$\frac{L}{c\tau}\cos\theta = 2, \tag{16}$$

we have

$$E_\Sigma(t, \theta) = \frac{Z_0 \sin\theta}{4\pi r c}\frac{1}{a}h_a'\left(\frac{t - \frac{r}{c} + \tau}{a\tau}\right)L. \tag{17}$$

In other words, current field (10) along the direction $\theta \sim 0°$ coincides with the directivity pattern of a vibrator excited by time distribution (13), which is uniform over the entire vibrator length.

RESULTS OF A NUMERICAL EXPERIMENT

To illustrate, we analyze the atomic function $h_2(t)$ for the carrier (–1, 1), which is denoted as up(t). Figure 1 shows results of the calculation of the radiation field along the direction $\theta = 90°$ for the cases (a) $L \ll c\tau$ and (b) $L = 2c\tau$ in the traveling-wave mode. As is clearly seen in both cases, the field shape in the far-field region is similar to that of both the initial pulse and its derivative in accordance with the functional-differential relationship

$$\mathrm{up}'(t) = 2[\mathrm{up}(2t+1) - \mathrm{up}(2t-1)].$$

Figure 2 presents the field in the far-field region for $L = 2c\tau$ when the angle θ decreases from 90° to zero. When θ approaches zero, the field shape becomes similar to that of the exciting current, whereas the pulse amplitude decreases by virtue of the dominating effect of the multiplier $\sin\theta$ in (4).

CONCLUSIONS

Thus, in this study, we have determined for the first time shapes of the current pulses of an ultra-wideband vibrator. These shapes determine the field behavior in the far-field region, which is similar to that of long-wave radiation. This physical effect is observed due to specific properties of the atomic functions $h_a(t)$. The data for these functions are unique and make it possible to reveal the indicated analogy between ultra-wideband and long-wave radiators. The novel physical effect obtained as a result of the study can be efficiently applied to solve problems of ultra-wideband radars and communication, generation of ultra-wideband radiation pulses, interactions of pulsed beams of charged particles with matter, etc.

REFERENCES

1. V. F. Kravchenko, *Lectures on Theory of Atomic Functions and Their Certain Applications* (Radiotekhnika, Moscow, 2003) [in Russian].
2. V. F. Kravchenko and M. A. Basarab, *Boolean Algebra and Methods of Approximation in Boundary Value Problems of Electrodynamics* (Fizmatlit, Moscow, 2004) [in Russian].
3. Yu. V. Gulyaev, V. F. Kravchenko, and D. V. Smirnov, Usp. Sovrem. Radioelektron., No. 8, 3 (2003).
4. V. F. Kravchenko and D. V. Smirnov, Élektromag. Volny Élektron. Sist. **10** (4), 21 (2005).
5. V. F. Kravchenko, D. V. Smirnov, and I. B. Fedorov, Dokl. Akad. Nauk **403**, 193 (2005) [Dokl. Phys. **50**, 355 (2005)].
6. I. Ya. Immoreev, Vestn. Bauman Mosk. Gos. Tekh. Univ., No. 4, 25 (1998).
7. G. S. Smith, IEEE Antenn. Propag. Mag. **40** (4), 39 (1998).
8. H. F. Harmuth, *Nonsinusoidal Waves in Radio Location and Radio Communication* (Academic, New York, 1981; Radio i Svyaz', Moscow, 1985).

Translated by G. Merzon

Doklady Physics, Vol. 50, No. 12, 2005, pp. 623–626. Translated from Doklady Akademii Nauk, Vol. 405, No. 4, 2005, pp. 475–478.

PHYSICS

Phase Diagram of Ultracold Nonideal Plasma

G. É. Norman

Presented by Academician V.E. Fortov May 12, 2005

Received May 25, 2005

In experiments [1], metastable plasma-like microscopic cesium droplets having a temperature of about 10^2 K and concentration of 10^{18} cm^{-3} were observed. Recent experiments [2, 3] have revealed new regimes of ultracold neutral plasma with a temperature of about 1 K. Although the states observed in [1–3] were relatively short-life, in their lifetime they attained stationary parameters. The results both of numerical simulations based on molecular-dynamics models and of the theory of ultracold plasma were analyzed in [4, 5] alongside the relevant problem of a Rydberg substance (see [6, 7]). Plasma parameters attained in the experiments described in [1–3] and analyzed on the basis of model calculations in [4–6] were related to nonideal plasma in which the number N_D of particles in the Debye sphere could be less than unity, the plasma having remained nondegenerate. Such a plasma should be verified from the standpoint of thermodynamic stability, which was performed in [8] for higher temperatures. However, in [1–7], the analysis for stability was not carried out, which could affect the interpretation of the results of both the experiments and numerical simulations. In the present study, we have extended the approach of [8] to low temperatures under the assumption that one may use the concepts of electron and ion temperatures. In this case, it is not required to discuss ionization equilibrium: neutral atoms either were absent or were not in equilibrium with electrons and ions in the conditions of [1–3].

THE THEORETICAL PHASE DIAGRAM

The diagram for temperature T and the electron concentration n_e is shown in the figure (the possible existence of neutral atoms is not taken into account). The nonideality parameter $\gamma = \dfrac{e^2(2n_e)^{1/3}}{k_B T}$ characterizes the ratio of the Coulomb interaction energy of free electrons and ions and their thermal energy. The value $\gamma \approx 1$ corresponds to line *1*; i.e., plasma becomes strongly nonideal below this line. In such a situation, the potential arises for phase transitions as a result of the competition between the resulting Coulomb attraction of charges to each other, at distances on the order of interparticle distance, and the quantum repulsion of particles, occurring at short distances compared to the mean interparticle distance [8]. This pattern is analogous to the case of the van der Waals equation for which the phase transition is a result of the competition between the long-range attraction of molecules and their short-range repulsion.

The regions of stable and/or metastable states are bounded by the condition of thermodynamic stability

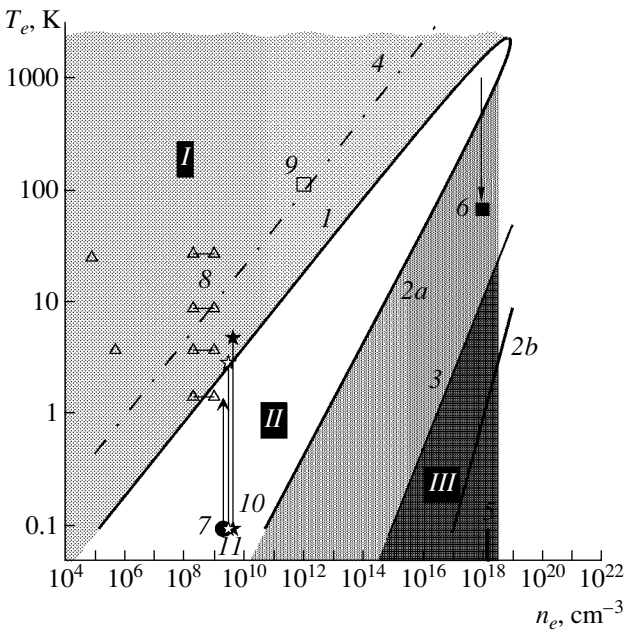

T–n_e diagram. Lines are based on theoretical concepts: (*1*) $\gamma = 1$; (*2a*) $\lambda\kappa = 5$ [asymptotic values *1* and *2a* are connected by a smooth transition line that corresponds to the dependence described by formula (3)]; (*2b*) the asymptotic limit (6); (*3*) the boundary of electron degeneration; (*4*) $N_D = 1$; and (*5*) conditional right boundary of metastability for $\tau = 1$ s. Experimental points: (*6*) [1]; (*7*) [2]; (*8*) [3]; and (*9*) [15] and simulation results: (*10*) [4] and (*11*) [5] are also shown.

Institute of Extreme States,
Joint Institute of High Temperatures,
Russian Academy of Sciences,
Izhorskaya ul. 13/19, Moscow, 125412 Russia
e-mail: henry_n@orc.ru; Norman@ihed.ras.ru

1028-3358/05/5012-0623$26.00

or by a line for which $\left(\frac{\partial P}{\partial V}\right)_T = 0$ (here, P and V are, respectively, pressure and volume). For the van der Waals equation, these regions exist at temperatures lower than the critical temperature T_c. This statement is also true for nonideal plasma: in the figure, these regions are constrained by the lines *1* and *2*. In line *1*, plasma loses its thermodynamic stability with a decrease in temperature; i.e., below line *1*, $\left(\frac{\partial P}{\partial V}\right)_T > 0$. In line *2*, plasma recovers its thermodynamic stability; i.e., below this line, $\left(\frac{\partial P}{\partial V}\right)_T < 0$.

In order to illustrate possible positions of lines *1* and *2*, as well as the spread in estimates of the value of T_c for nonideal plasma, we exploit two approximations of [8] for the free energy of electrons and ions, namely, $F_{1,2} = F_0 - \Delta F_{1,2}$. Here, F_0 is the free energy of perfect gas:

$$\Delta F_1 = F_{\mathrm{DH}}(1 - 0.75C\lambda\kappa), \quad (1)$$

$$\Delta F_2 = F_{\mathrm{DH}}(1 + 0.75C\lambda\kappa)^{-1}, \quad (2)$$

$F_{\mathrm{DH}} = \frac{2}{3}\pi^{1/2}e^3N^{3/2}(k_BTV)^{-1/2}$ is the Debye–Hückel free energy for a classical system of charged particles; $N = 2N_e$ is the number of electrons and ions in the volume V; $N_e = n_eV$; $\lambda = h(3k_BTm)^{-1/2}$ is the electron de-Broglie wavelength; κ is the reciprocal Debye radius; and $C = 0.1$.

The multiplier $(1 \pm 0.75C\lambda\kappa)$ in (1) or (2) allows for the quantum repulsion between charges. Expression (1) is the virial expansion for plasma, which was obtained in [9] in the approximation $\gamma \ll 1$ and $\lambda\kappa \ll 1$. Expression (2) is the Padé approximation that is considered more reliable for the extrapolation to the nonideal region (see, e.g., [10] and references therein). Expressions (1) and (2) coincide with each other for $\gamma \ll 1$ and $\lambda\kappa \ll 1$.

For both Eq. (1) and Eq. (2), the condition $\gamma \gtrsim 1$ corresponds to the sign change for $\left(\frac{\partial P}{\partial V}\right)_T$, i.e., to thermodynamic-stability loss at temperatures much lower than the critical temperature T_c. Line *1* in the figure constrains the stability region from below for both Eq. (1) and Eq. (2). The equivalency of the conditions for the stability loss $\left(\frac{\partial P}{\partial V}\right)_T > 0$ and $\gamma \gtrsim 1$ is retained for nearly all approaches in the thermodynamics of nonideal plasma [8, 10].

Nevertheless, there exists the noticeable difference in the estimate of the condition for which the thermodynamic stability is recovered due to the quantum repulsion between particles [8, 10]. Therefore, the position of line *2* is less determinate than that of line *1*. From the condition $\left(\frac{\partial P}{\partial V}\right)_T = -\left(\frac{\partial^2 F}{\partial V^2}\right)_T = 0$ for Eq. (1), we can find the connection between temperature T and concentration n_e:

$$\pi^{1/2}\gamma^{3/2}(1 - 2C\lambda\kappa) = 2 \quad (3)$$

in the line that separates thermodynamically stable and unstable regions. Dependence (3) has the asymptotic values $\gamma \approx 1$ (line *1*) and

$$\lambda\kappa = (2C)^{-1} \quad (4)$$

(lines *2a*). Both asymptotes are connected in the region of the critical temperature $T_c = 2660$ K in the same manner as that occurring for the van der Waals equation.

From the condition $\left(\frac{\partial P}{\partial V}\right)_T = 0$, for (2), we find a dependence that strongly differs from (3):

$$\pi^{1/2}\gamma^{3/2}(1 + 0.25C\lambda\kappa) = 2(1 + 0.75C\lambda\kappa)^3, \quad (5)$$

this yields the same first asymptote, $\gamma \approx 1$ (line *1*), and a different second asymptote,

$$a_0\kappa = (18\pi^2C^2)^{-1} \quad (6)$$

(line *2b*), where a_0 is the Bohr radius. The smooth connection of lines *1* and *2b* occurs in the vicinity of the critical temperature $T_c = 10^4$ K, which is not shown in the figure. The values of T_c for (1) and (2) were found even in [8]. Since then, the range of values of T_c has been discussed many times; however, it has changed little, having been shifted to values close to 10^4 K [10].

Line *3* constrains from above the region of degenerate plasma. The degeneration of electrons ensures the thermodynamic stability of electron-ion plasma. However, it was noted even in [8] that pair quantum effects in electron-ion interactions, which are characterized by the parameter $\lambda\kappa$, could be an even stronger stabilizing factor. Both line *2a* and, partly, line *2b* are located above line *3*.

Thus, independently of the approximations used, one can separate three regions in the figure. Plasma is ideal or weakly nonideal and thermodynamically stable in region *I* above line *1*, where $\left(\frac{\partial P}{\partial V}\right)_T < 0$. In region I, collisional recombination occurs. Plasma is thermodynamically labile (absolutely unstable) in region *II* between lines *1* and *2*, where $\left(\frac{\partial P}{\partial V}\right)_T > 0$. Comparing the positions of lines *2a* and *2b*, we can see that the

lower boundary of absolutely unstable region *II* is estimated with a noticeable indeterminacy. However, even the most unfavorable approximation (1) (line *2a*) does not cast any doubt on the fact of the existence of region *II*. The condition $\left(\frac{\partial P}{\partial V}\right)_T < 0$ of thermodynamic stability is recovered in region *III* below line *2*. Metastable plasma in this region between lines *2* and *3* is nondegenerate, and the Debye number formally calculated for it turns out to be well below unity.

In accordance with [7], the metastable region is constrained from the side of high densities by the stability loss with respect to the radiative and/or Auger recombination, because the lifetime τ with respect to these processes depends on n_e. The function $\tau(n_e)$ was calculated in [7] for $T = 0$. Vertical line *5* is indicated as a conditional boundary $n_e = 10^{18}$ cm^{-3}, which corresponds to $\tau = 1$ s. The function $\tau(n_e)$ is rather steep. The shadowed region *III* is extended up to the value $n_e = 4 \times 10^{18}$ cm^{-3}, which corresponds to $\tau = 10^{-3}$ s. The estimates of [7] were performed for a crystalline model at $T = 0$. The melting line of such a Rydberg crystal is poorly estimated and is therefore not shown in the figure.

To the left of vertical line *5*, plasma densities correspond to principal quantum numbers exceeding 10, i.e., to hydrogen-like atoms. Therefore, one can expect that the diagram in the figure weakly depends on the type of plasma-forming atoms.

It should be emphasized that the metastability of states in region *III* has a double nature and corresponds to both the radiative and/or Auger recombination [7] and homogeneous nucleation (see [11]). In [11], the stability of metastable nonideal plasma with respect to the collisional recombination was also considered.

DISCUSSION OF EXPERIMENTAL RESULTS

In [1], an experimental setup was developed on the basis of a thermal-field emission transformer. A container with metallic cesium acted as a source of cesium atoms at a temperature T of about 400 K. Cesium atoms were excited as a result of striking the graphite foil (1300 K) that served as an emitter. The flux density of excited atoms attained 10^{15} cm^{-3} s^{-1}. Alongside the separate atoms, clusters containing up to 40000 cesium atoms were registered in the flux. The clusters were captured by a trap cooled by liquid nitrogen. The microscopic droplet formed as a result of this procedure had a diameter of about 0.5 mm and density of 10^{18} cm^{-3}, which was close to the gas density.

Point 6 in the figure corresponds to the final state of cooled condensed cesium microdroplets [1]. The way to obtain the microdroplets is approximately indicated by the arrow. The existence of the stationary state of these microdroplets was confirmed by the series of experiments performed in [12], in which laser generation with the participation of microdroplets was observed. The reliability of the approach used in [1, 12] was verified in the experiments carried out in [13].

The lifetime of the microdroplets for their radiative decay attained several seconds. This time greatly exceeds that for establishing equilibrium over all intrinsic degrees of freedom. Therefore, to describe the microdroplet state, one can use standard thermodynamic parameters, namely, temperature, specific volume, and pressure. Since in the process of the observation of microdroplets after their formation they are not supplied with energy, states of microdroplets can be related to the metastable states considered in thermodynamics. Thus, the presence of point *6* in the thermodynamic diagram is quite correct. This point turned out to be just on the boundary of region III, where, in accordance with [8], the recovery of thermodynamic stability of the metastable states of nonideal plasma can be expected.

The presence of the results of [2–5] in the diagram exhibited in the figure seems more ambiguous. In the experiments performed in [2, 3], nonequilibrium plasma with different temperatures T_e of electrons and T_i of ions was generated by the femtosecond laser excitation of ultracold gas. In the first paper [2], it was reported that the parameters $T_e = 100$ mK and $n_e = 2 \times 10^9$ cm^{-3} had been obtained (point *7*). Later, these parameters were simulated in [4, 5] by molecular-dynamics methods (points *10* and *11*). In [4] and [5], models of the effective electron-ion interaction were different. However, the results obtained turned out to be the same: very rapid (within one plasma oscillation) initial plasma heating up to a state with $\gamma \approx 1$ and the subsequent molecular-dynamic trajectory at a stationary value of γ or of the electron temperature. The authors of [2] then agreed that the same pattern must also be observed in their experiment.

In [4, 5], the rapid initial heating of plasma electrons was related to the process of the establishment of electron-ion correlations, which had been accompanied by a potential-energy transfer to the kinetic energy due to the noncorrelatedness of the initial state of plasma (initial coordinates of ions are random as in the ideal gas). Without a doubt, such a process does take place (see also [14]). At the same time, the process of establishing the electron distribution close to the Maxwellian one lasts only for one-tenth of a fraction of a plasma oscillation [14], i.e., is much shorter than heating time. Therefore, the electron equation of state is valid virtually from the very onset of the heating, and thermodynamic instability must be manifested. Taking into account the long distance of points *7*, *10*, and *11* from line *1*, the difference between T_e and T_i must not affect the instability of plasma states *7*, *10*, and *11*, although the value of $\left(\frac{\partial P}{\partial V}\right)_T$ may slightly differ from its value at $T_e = T_i$. Thus, it seems to us that the rapid relaxation of states *7*, *10*, and *11* in the region $\gamma \approx 1$ is stipulated by

both the disorder-induced heating and spinodal decay. It is of importance the fact that relaxation processes starting from points *10* and *11* end up exactly in the region of line $\gamma \approx 1$ in which the thermodynamic stability is recovered.

It is worth noting that, if, in [1], the stationary state is obtained as a result of stimulated external cooling, then, in [2], it is caused by the spontaneous internal heating.

The authors of [2] have extended their measurements to the region of final states obtained in [4, 5], i.e., to those above region *II* of the absolute instability (points *8* in the figure). In [2, 3], xenon plasma was studied. A similar point was obtained in [15] for cesium plasma. No indications of initial rapid heating were obtained in these studies, although, as in [2], initial ion coordinates were also uncorrelated. In other words, inevitable heating caused by initial chaotic ion distribution is not manifested at once when there is no basis for spinodal decay. Point *9* represents ultimate parameters attained in [15], where, nevertheless, an attempt to condense excited cesium atoms failed. The authors of [15] assumed that in order to do this it was necessary to either elevate the plasma density by two orders of magnitude or to decrease temperature down to fractions of a Kelvin. These estimates do not strongly deviate from the boundary of region *III*.

The region between lines *4* and *1* is of particular interest because, here, the number N_D is less than unity, and nonideality effects can already be observed.

Thus, the possibility of the existence of thermodynamically labile and metastable states of nonideal plasma, which are similar to those considered in analyzing the van der Waals equation, was predicted at the end of the 1960s [8]. Neither the results of recent experiments [1–3] nor those of simulations [4, 5] contradict to the prediction of [8].

In [1], a stationary state existing throughout the period of one second, i.e., a metastable state was experimentally observed. The parameters of this state lay in region *III* of the states that belonged to metastable ones according to the estimates of [8].

The states studied in [2–5], with initial parameters that corresponded to the region of states *II* and that were (according to estimates of [8]) labile, underwent decay. This decay may be interpreted as the spinodal type.

As was shown in the experiments, the states experimentally studied in [3, 15] whose initial parameters corresponded to region *I* and that, according to estimates of [8], had been thermodynamically stable indeed turned out to be stationary.

ACKNOWLEDGMENTS

This work was supported by the program “Thermal Physics and Mechanics of Intense Thermal Actions” of the Presidium of the Russian Academy of Sciences and by the Russian Foundation for Basic Research, project no. 04-02-17065a.

REFERENCES

1. C. Aman, J. B. C. Pettersson, L. Lindroth, and L. Holmlid, J. Mater. Res. **7**, 100 (1992).
2. T. C. Killian, S. Kulin, S. D. Bergeson, *et al.*, Phys. Rev. Lett. **83**, 4776 (1999).
3. S. Kulin, T. C. Killian, S. D. Bergeson, and S. L. Rolston, Phys. Rev. Lett. **85**, 318 (2000).
4. S. Mazevet, L. A. Collins, and J. D. Kress, Phys. Rev. Lett. **88**, 55001 (2002).
5. S. G. Kuzmin and T. M. O’Neil, Phys. Plasmas **9**, 3743 (2002).
6. M. Bonits, B. B. Zelener, B. V. Zelener, *et al.*, Zh. Éksp. Teor. Fiz. **125**, 821 (2004) [JETP **98**, 719 (2004)].
7. É. A. Manykin, M. I. Ozhovan, and P. P. Poluektov, Khim. Fiz. **19** (7), 87 (1999).
8. G. É. Norman and A. N. Starostin, Teplofiz. Vys. Temp. **8**, 413 (1970).
9. A. A. Vedenov and A. I. Larkin, Zh. Éksp. Teor. Fiz. **36**, 1133 (1959) [Sov. Phys. JETP **36**, 806 (1959)].
10. W. Ebeling and G. E. Norman, J. Stat. Phys. **110**, 861 (2003).
11. G. É. Norman, Pis’ma Zh. Éksp. Teor. Fiz. **73**, 13 (2001) [JETP Lett. **73**, 10 (2001)].
12. L. Holmlid, J. Phys. B **37**, 357 (2004).
13. V. I. Yarygin, V. N. Sidel’nikov, I. I. Kasikov, *et al.*, Pis’ma Zh. Éksp. Teor. Fiz. **77**, 330 (2003) [JETP Lett. **77**, 280 (2003)].
14. I. V. Morozov and G. É. Norman, Zh. Éksp. Teor. Fiz. **127**, 412 (2005) [JETP **100**, 370 (2005)].
15. G. Vitrant, J. M. Raimond, M. Gross, and S. Haroche, J. Phys. B **15**, L49 (1982).

Translated by G. Merzon

Doklady Physics, Vol. 50, No. 12, 2005, pp. 627–631. Translated from Doklady Akademii Nauk, Vol. 405, No. 5, 2005, pp. 613–617.

PHYSICS

Propagation of a Radio Pulse in Gyrotropic Plasmas

G. M. Strelkov

Presented by Academician Yu.V. Gulyaev February 18, 2005

Received March 2, 2005

The problem of describing distortions of radio-frequency (radio) pulses in media exhibiting dispersion was formulated almost a century ago and continues as ever to be urgent by virtue of its practical significance. Within the framework of the problem, an important place is occupied by the theory of the propagation of radio pulses through the ionosphere in the presence of magnetic field. Relevant studies are based on the analysis of results of the inverse Fourier transformation of the current frequency spectrum for a propagating signal. Thus, transformation is performed by both analytically and numerically and, as a rule, under noticeable constraints for problem parameters [1–11]. In the present paper, we propose a solution to the problem of the propagation of radio pulses in magneto-active collisional cold plasmas. The solution is not based on frequency conceptions and allows us to analytically describe the space-and-time evolution of a pulse with an initial envelope of a rather general shape.

As is well known, the pulse propagation obeys the wave equation

$$\frac{\partial^2 \mathbf{E}}{\partial z^2} = \frac{1}{c^2}\frac{\partial^2 \mathbf{E}}{\partial t^2} + \frac{4\pi}{c^2}\frac{\partial^2 \mathbf{P}}{\partial t^2}, \tag{1}$$

where **E** is the electric-field strength, c is the speed of light in a medium, z is the pulse propagation direction, t is time, and **P** is the polarization of a unit volume of the medium. Within the model of a medium with free charges (see, e.g., [12, 13]), the quantity **P** is described by the equation

$$\frac{\partial^2 \mathbf{P}}{\partial t^2} + \nu\frac{\partial \mathbf{P}}{\partial t} = \frac{e^2 N}{m}\mathbf{E} - \frac{|e|}{mc}\left[\frac{\partial \mathbf{P}}{\partial t}, \mathbf{H}_0\right]. \tag{2}$$

Here, e, m, and N are the electron charge, mass, and concentration, respectively; ν is the effective collision frequency that allows for the energy loss by electrons in their collisions with neutral molecules and ions; and $\mathbf{H}_0$ is the strength of the homogeneous magnetic field. The solution to the set of equations (1), (2) is found in the long-pulse approximation, with the pulse carrier frequency f and characteristic pulse duration t_p satisfying the inequality $ft_p \gg 1$. This approximation is fulfilled, in particular, for large-basis pulses.

The exact form of the solution is determined by the value of the angle between the vectors of the pulse-propagation and magnetic-field directions. We now introduce the coordinate system (x, y, z) with the unit vectors $\mathbf{i}_0$, $\mathbf{j}_0$, and $\mathbf{k}_0$. We also assume that the pulse propagates along the z axis, i.e., along the magnetic-field direction, so that $\mathbf{H}_0 = \mathbf{k}_0 H_0$. The plane wave impinging onto the half-space boundary $z \geq 0$ can be specified in the form

$$\mathbf{E}(0; t) = \mathbf{A}(0; t)\exp(i\omega t) = \mathbf{i}_0 A(0; t)\exp(i\omega t), \quad t \geq 0 \tag{3}$$

(Here, $\omega = 2\pi f$ and $\mathbf{A}(0; t)$ is the pulse envelope for $z = 0$.)

The leading front of the pulse always propagates at a velocity equal to the speed of light in the medium. Correspondingly, we seek the field **E** in the medium in the form

$$\mathbf{E}(z; t) = \begin{cases} \mathbf{A}\left(z; t - \frac{z}{c}\right)\exp(i(\omega t - kz)), & t - \frac{z}{c} \geq 0, \\ 0, & t - \frac{z}{c} < 0, \end{cases} \tag{4}$$

where $k = \frac{2\pi}{\lambda}$ is the wave number and $\mathbf{A}(z; t) = \mathbf{i}_0 A_x(z; t) + \mathbf{j}_0 A_y(z; t)$.

We change the variables in relationships (1) and (2):

$$z' = z, \quad t' = t - \frac{z}{c}. \tag{5}$$

Institute of Radio Engineering and Electronics, Russian Academy of Sciences, Fryazino Branch, pl. Vvedenskogo 1, Fryazino, Moscow oblast, 141120 Russia
e-mail: strelkov@ms.ire.rssi.ru

1028-3358/05/5012-0627$26.00

Thus, with allowance for expression (4), we arrive at

$$\frac{\partial^2 \mathbf{A}}{\partial (z')^2} - \frac{2}{c}\frac{\partial^2 \mathbf{A}}{\partial z' \partial t'} - 2ik\frac{\partial \mathbf{A}}{\partial z'} = \frac{4\pi}{c^2}\frac{\partial^2 \mathbf{P}}{\partial (t')^2}\exp(-i\omega t'), \quad (6)$$

$$\frac{\partial^2 \mathbf{P}}{\partial (t')^2} + \nu\frac{\partial \mathbf{P}}{\partial t'} = \frac{e^2 N}{m}\mathbf{A}(z'; t')\exp(i\omega t') - \frac{|e|}{mc}\left[\frac{\partial \mathbf{P}}{\partial t'}, \mathbf{H}_0\right]. \quad (7)$$

We now compare the first and third terms on the left-hand side of Eq. (6) with respect to their moduli as applied to the pulse (with the filling) under consideration. For the characteristic pulse duration t_p, the inequality $ft_p \gg 1$ holds true, and the pulse occupies the interval $L_p = ct_p \gg \lambda$ in the z' axis. Therefore, the estimate

$$\left|\frac{\partial^2 \mathbf{A}}{\partial (z')^2}\right| \sim \left|\frac{1}{L_p}\frac{\partial \mathbf{A}}{\partial z'}\right| \ll \left|\frac{4\pi}{\lambda}\frac{\partial \mathbf{A}}{\partial z'}\right|, \quad (8)$$

is valid, and we may ignore the first term on the left-hand side of Eq. (6).

When the pulse propagates along the magnetic field direction, $\mathbf{P} = \mathbf{i}_0 P_x + \mathbf{j}_0 P_y$, and Eq. (7) is equivalent to the set of two scalar equations

$$\frac{\partial^2 P_x}{\partial (t')^2} + \nu\frac{\partial P_x}{\partial t'} = \frac{e^2 N}{m}A_x(z'; t')\exp(i\omega t') - \frac{|e|H_0}{mc}\frac{\partial P_y}{\partial t'}, \quad (9)$$

$$\frac{\partial^2 P_y}{\partial (t')^2} + \nu\frac{\partial P_y}{\partial t'} = \frac{e^2 N}{m}A_y(z'; t')\exp(i\omega t') + \frac{|e|H_0}{mc}\frac{\partial P_x}{\partial t'}. \quad (10)$$

As the position and velocity of an electron cannot be changed instantaneously, the following condition holds in cold plasma at the moment of pulse arrival at the point z':

$$P_x(z'; 0) = P_y(z'; 0) = 0, \quad \left.\frac{\partial P_x}{\partial t'}\right|_{t' = 0} = \left.\frac{\partial P_y}{\partial t'}\right|_{t' = 0} = 0. \quad (11)$$

We now substitute the solution to the set of Eqs. (9), (10), which was obtained for initial conditions (11), into Eq. (6). With due regard for estimate (8), we arrive at the following set of equations for the envelope components $A_x(z'; t')$ and $A_y(z'; t')$:

$$\frac{\partial^2 A_x}{\partial z' \partial t'} + i\omega\frac{\partial A_x}{\partial z'} = -\frac{\omega_0^2}{2c}\Bigg[A_x(z'; t') - \frac{\nu + i\omega_H}{2}\int_0^{t'} A_x(z'; \theta)\exp(-(\nu + i\omega_H + i\omega)(t' - \theta))d\theta - \frac{\nu - i\omega_H}{2}\int_0^{t'} A_x(z'; \theta) \times \exp(-(\nu - i\omega_H + i\omega)(t' - \theta))d\theta - \frac{\nu + i\omega_H}{2}\int_0^{t'} A_y(z'; \theta)\exp(-(\nu + i\omega_H + i\omega)(t' - \theta))d\theta + \frac{\nu - i\omega_H}{2}\int_0^{t'} A_y(z'; \theta)\exp(-(\nu - i\omega_H + i\omega)(t' - \theta))d\theta\Bigg], \quad (12)$$

$$\frac{\partial^2 A_y}{\partial z' \partial t'} + i\omega\frac{\partial A_y}{\partial z'} = -\frac{\omega_0^2}{2c}\Bigg[A_y(z'; t') - \frac{\nu + i\omega_H}{2}\int_0^{t'} A_y(z'; \theta)\exp(-(\nu + i\omega_H + i\omega)(t' - \theta))d\theta - \frac{\nu - i\omega_H}{2}\int_0^{t'} A_y(z'; \theta) \times \exp(-(\nu - i\omega_H + i\omega)(t' - \theta))d\theta + \frac{\nu + i\omega_H}{2}\int_0^{t'} A_x(z'; \theta)\exp(-(\nu + i\omega_H + i\omega)(t' - \theta))d\theta - \frac{\nu - i\omega_H}{2}\int_0^{t'} A_x(z'; \theta)\exp(-(\nu - i\omega_H + i\omega)(t' - \theta))d\theta\Bigg]. \quad (13)$$

In Eqs. (12) and (13), denotations are used: $\omega_0^2 = \frac{4\pi e^2 N}{m}$ (ω_0 is the plasma frequency) and $\omega_H = \frac{|e|H_0}{mc}$ is the electron gyromagnetic frequency.

The solution to the set of Eqs. (12), (13) is found by the operator method. Omitting the rather cumbersome

intermediate calculations, we obtain the final result ($\delta = \delta(z') = \frac{\omega_0^2 z'}{2c}$: hereinafter, $J_k(x)$ is the Bessel function):

$$A_x(z'; t') = A(0; t') - \frac{1}{2}\int_0^{t'} \sqrt{\frac{\delta}{t'-\theta}} J_1(2\sqrt{\delta(t'-\theta)}) \times \exp(-(\nu + i\omega_H + i\omega)(t'-\theta))A(0; \theta)d\theta - \frac{1}{2}\int_0^{t'} \sqrt{\frac{\delta}{t'-\theta}} J_1(2\sqrt{\delta(t'-\theta)}) \times \exp(-(\nu - i\omega_H + i\omega)(t'-\theta))A(0; \theta)d\theta; \quad (14)$$

$$A_y(z'; t') = -\frac{i}{2}\int_0^{t'} \sqrt{\frac{\delta}{t'-\theta}} J_1(2\sqrt{\delta(t'-\theta)}) \times \exp(-(\nu + i\omega_H + i\omega)(t'-\theta))A(0; \theta)d\theta + \frac{i}{2}\int_0^{t'} \sqrt{\frac{\delta}{t'-\theta}} J_1(2\sqrt{\delta(t'-\theta)}) \times \exp(-(\nu - i\omega_H + i\omega)(t'-\theta))A(0; \theta)d\theta. \quad (15)$$

The solution obtained can be represented in the vector form as

$$\mathbf{A}(z'; t') = \mathbf{A}_o(z'; t') + \mathbf{A}_e(z'; t') = A_o(z'; t')(\mathbf{i}_0 + i\mathbf{j}_0) + A_e(z'; t')(\mathbf{i}_0 - i\mathbf{j}_0), \quad (16)$$

where the denotation

$$A_o(z'; t') = 0.5\left[A(0; t') - \int_0^{t'} \sqrt{\frac{\delta}{t'-\theta}} J_1(2\sqrt{\delta(t'-\theta)}) \times \exp(-(\nu + i\omega_H + i\omega)(t'-\theta))A(0; \theta)d\theta\right] \quad (17)$$

is used, and the expression for $A_e(z'; t')$ is obtained from the expression for $A_o(z'; t')$ provided that we have replaced $+\omega_H$ by $-\omega_H$ on the right-hand side of expression (17). The result (16) implies that a pulse propagating along the magnetic-field direction is the sum of two pulses with the circular and counter-wise polarizations. Following the standard terminology in the theory of plane waves in plasmas (see [12]), it is natural to define these pulses as ordinary and extraordinary. Their projections onto the x axis were denoted above as $A_o(z'; t')$ and $A_e(z'; t')$.

We can illustrate the solution obtained by the example of distortions of a biexponential pulse with the initial envelope

$$A(0; t) = A_0\left(\exp\left(-\frac{\alpha t}{t_p}\right) - \exp\left(-\frac{\beta t}{t_p}\right)\right) \quad (18)$$

(A_0, α, and β are numbers). Substituting (18) into (14) and (15) and replacing the variable $\mu = \sqrt{\frac{\theta}{t'}}$ in the expressions obtained, we arrive at the relationships

$$A_x(z'; t') = A_x(z'; t'; \alpha) - A_x(z'; t'; \beta), \quad (19)$$

$$A_y(z'; t') = A_y(z'; t'; \alpha) - A_y(z'; t'; \beta), \quad (20)$$

where the α-dependent terms have the form

$$A_x(z'; t'; \alpha) = A_0\exp\left(-\frac{\alpha t'}{t_p}\right)\left[1 - \frac{1}{2}\int_0^1 J_1(2\mu\sqrt{\delta t'}) \times \exp\left(-\left(\nu - \frac{\alpha}{t_p} + i\omega_H + i\omega\right)t'\mu^2\right)(2\sqrt{\delta t'})d\mu - \frac{1}{2}\int_0^1 J_1(2\mu\sqrt{\delta t'}) \times \exp\left(-\left(\nu - \frac{\alpha}{t_p} - i\omega_H + i\omega\right)t'\mu^2\right)(2\sqrt{\delta t'})d\mu; \quad (21)$$

$$A_y(z'; t'; \alpha) = -\frac{i}{2}\int_0^1 J_1(2\mu\sqrt{\delta t'}) \times \exp\left(-\left(\nu - \frac{\alpha}{t_p} + i\omega_H + i\omega\right)t'\mu^2\right)(2\sqrt{\delta t'})d\mu + \frac{i}{2}\int_0^1 J_1(2\mu\sqrt{\delta t'}) \times \exp\left(-\left(\nu - \frac{\alpha}{t_p} - i\omega_H + i\omega\right)t'\mu^2\right)(2\sqrt{\delta t'})d\mu, \quad (22)$$

and the terms depending on the parameter β are found from equalities (21) and (22), respectively, by replacing in them α by β. The decay process for the initial biexponential pulse, as can be observed in the case when the signal is received by an electric dipole oriented along the x axis [see (19)], is illustrated in the figure. Initially, the ordinary and extraordinary pulses mutually interfere with each other so that the envelope observed (curve *2*) can noticeably differ from the initial one (curve *1*). With penetration deep into the medium, the extraordinary pulse follows the ordinary one, retarding more and more from it and undergoing relatively stronger absorption (curve *3*).

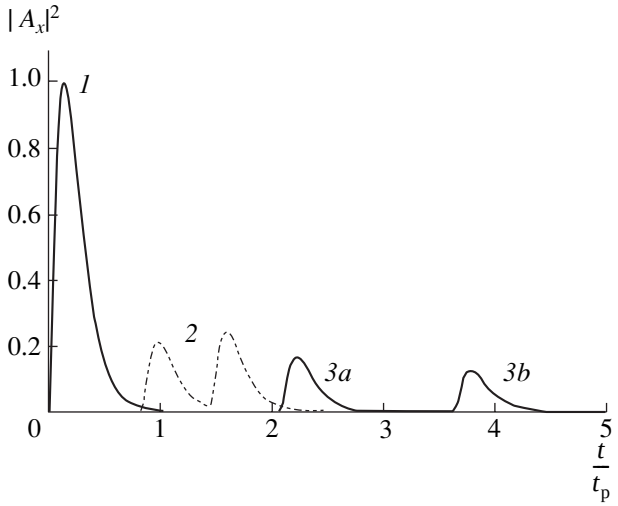

Decay of biexponential pulse in cold gyrotropic plasma ($N = 10^5$ cm^{-3}; $\nu = 10^3$ s^{-1}; $f_0 = \frac{\omega_0}{2\pi} = 2.84$ MHz; $H_0 = 0.5$ Oe; $f = 10$ MHz; $t_p = 10^{-4}$ s; $\alpha = 4$; $\beta = 10$; $A_0 = 3.07$): (*1*) initial envelope, $z = 0$; (*2*) $z = 800$ km and $\delta t_p = 4.24 \times 10^7$; and (*3a*) ordinary and (*3b*) extraordinary pulses, $z = 2000$ km and $\delta t_p = 1.06 \times 10^8$.

Analytical expressions for the propagation velocities of the ordinary and extraordinary pulses can be derived on the basis of any of the terms entering into the expressions for A_x and A_y [see (19) and (20)]. For example, we make use of expression (21) for the term $A_x(z'; t'; \alpha)$. Sequentially applying the relationship $\frac{d(J_{k+1}(x)x^{k+1})}{dx} = J_k(x)x^{k+1}$, we calculate the integrals in (21) by parts for an infinite number of times. As a result, we arrive at

$$A_x(z'; t'; \alpha) = 0.5A_0\exp\left(-\frac{\alpha t'}{t_p}\right)$$

$$\times\left[\exp\left(-\left(\nu - \frac{\alpha}{t_p} + i\omega_H + i\omega\right)t'\right)\right.$$

$$\times\sum_{k=0}^{\infty}\left(\left(\nu - \frac{\alpha}{t_p} + i\omega_H + i\omega\right)\sqrt{\frac{t'}{\delta}}\right)^k J_k(2\sqrt{\delta t'})$$

$$+\exp\left(-\left(\nu - \frac{\alpha}{t_p} - i\omega_H + i\omega\right)t'\right)$$

$$\left.\times\sum_{k=0}^{\infty}\left(\left(\nu - \frac{\alpha}{t_p} - i\omega_H + i\omega\right)\sqrt{\frac{t'}{\delta}}\right)^k J_k(2\sqrt{\delta t'})\right]. \quad (23)$$

We assume the validity of the inequality $2\sqrt{\delta t_p} \gg 1$, which is usual for ionospheric routes (see caption to the figure), and use the asymptotic representation of the Bessel functions for large arguments [14]:

$$J_k(2\sqrt{\delta t'}) \simeq \frac{1}{\sqrt{\pi\sqrt{\delta t'}}}\cos\left(2\sqrt{\delta t'} - \frac{k\pi}{2} - \frac{\pi}{4}\right). \quad (24)$$

After the substitution of expression (24) into relationship (23) and the summation of the series, the expression for $A_x(z'; t'; \alpha)$ takes the form

$$A_x(z'; t'; \alpha) \simeq 0.5A_0\exp\left(-\frac{\alpha t'}{t_p}\right)(\pi\sqrt{\delta t'})^{-1/2}$$

$$\times\left[\exp\left(-\left(\nu - \frac{\alpha}{t_p} + i\omega_H + i\omega\right)t'\right)\right.$$

$$\left.\times\frac{\cos\left(2\sqrt{\delta t'} - \arctan\left(\left(\nu - \frac{\alpha}{t_p} + i\omega_H + i\omega\right)\sqrt{\frac{t'}{\delta}}\right) - \frac{\pi}{4}\right)}{\sqrt{1 + \left(\nu - \frac{\alpha}{t_p} + i\omega_H + i\omega\right)^2\frac{t'}{\delta}}}\right]$$

$$+\left[\exp\left(-\left(\nu - \frac{\alpha}{t_p} - i\omega_H + i\omega\right)t'\right)\right.$$

$$\left.\times\frac{\cos\left(2\sqrt{\delta t'} - \arctan\left(\left(\nu - \frac{\alpha}{t_p} - i\omega_H + i\omega\right)\sqrt{\frac{t'}{\delta}}\right) - \frac{\pi}{4}\right)}{\sqrt{1 + \left(\nu - \frac{\alpha}{t_p} - i\omega_H + i\omega\right)^2\frac{t'}{\delta}}}\right]. \quad (25)$$

Thus, the pulse is concentrated in the vicinity of two points in the z' axis, which correspond to the minima of the moduli of subradical expressions in the denominators of the right-hand side of expression (25). The coordinates of these points satisfy the condition

$$1 = \frac{t'}{\delta}\left(-\left(\nu - \frac{\alpha}{t_p}\right)^2 + (\omega \pm \omega_H)^2\right), \quad (26)$$

whence it follows that the ordinary and extraordinary

pulses propagate at the velocities

$$V_o = \frac{c}{1 + \dfrac{0.5\omega_0^2}{(\omega + \omega_H)^2 - \left(\nu - \dfrac{\alpha}{t_p}\right)^2}}, \quad (27)$$

$$V_e = \frac{c}{1 + \dfrac{0.5\omega_0^2}{(\omega - \omega_H)^2 - \left(\nu - \dfrac{\alpha}{t_p}\right)^2}}, \quad (28)$$

respectively. According to formulas (27) and (28), collisions occurring in plasma can affect the pulse propagation velocity if the collision frequency ν is comparable with the carrier frequency. For the parameters indicated in the figure caption for the medium and the pulse, the inequality $(\omega \pm \omega_H)^2 \gg \max\left\{\left(\nu - \dfrac{\alpha}{t_p}\right)^2; \left(\nu - \dfrac{\beta}{t_p}\right)^2\right\}$ is fulfilled, which characterizes the situation that is typical for the ionosphere (see, e.g., [15]). In this case, the expressions for the propagation velocity are considerably simplified, namely,

$$V_o = \frac{c}{1 + \dfrac{0.5\omega_0^2}{(\omega + \omega_H)^2}} \text{ and } V_e = \frac{c}{1 + \dfrac{0.5\omega_0^2}{(\omega - \omega_H)^2}}.$$

REFERENCES

1. Sh. Kozaki and Y. Mushiake, IEEE Trans. Antennas Propag. **AP-1** (5), 686 (1969).
2. Sh. Kozaki and Y. Mushiake, IEEE Trans. Antennas Propag. **AP-18** (2), 259 (1970).
3. K. C. Chen and J.-L. Yen, Radio Sci. **7** (6), 681 (1972).
4. K. C. Chen and J.-L. Yen, Radio Sci. **8** (1), 51 (1973).
5. E. Brookner, IEEE Trans. Antennas Propag. **AP-26** (2), 307 (1978).
6. E. Bahar and B. S. Agraval, IEEE Trans. Antennas Propag. **AP-27** (2), 225 (1979).
7. R. E. McIntosh and A. Malaga, Radio Sci. **15** (3), 645 (1980).
8. D. C. D. Chang and R. A. Helliwell, IEEE Trans. Antennas Propag. **AP-28** (2), 170 (1980).
9. D. Y. Zhang and K. K. Tshu, Radio Sci. **22** (4), 635 (1987).
10. D. K. Kalluri, IEEE Trans. Antennas Propag. **3** (12), 1638 (1989).
11. N. V. Kretov, T. E. Ryzhkina, and L. V. Fedorova, Radiotekh. Elektron. (Moscow) **36** (1), 1 (1991).
12. V. L. Ginzburg, *Propagation of Electromagnetic Waves in Plasmas*, 2nd ed. (Nauka, Moscow, 1967; Pergamon Press, Oxford, 1970).
13. E. A. Pamyatnykh and E. A. Turov, *Foundations of Electrodynamics in Material Media: Variable and Heterogeneous Media* (Nauka, Moscow, 2000) [in Russian].
14. B. G. Korenev, *Introduction to Theory of Bessel Functions* (Nauka, Moscow, 1971) [in Russian].
15. V. V. Kirillov and V. N. Kopeĭkin, Izv. Vyssh. Uchebn. Zaved., Radiofiz. **46** (1), 1 (2003).

Translated by G. Merzon

Doklady Physics, Vol. 50, No. 12, 2005, pp. 632–633. Translated from Doklady Akademii Nauk, Vol. 405, No. 6, 2005, pp. 753–754.

PHYSICS

The Field Theory of Gravitation and the Rest Mass of Particles

Academician S. S. Gershteĭn, Academician A. A. Logunov, and M. A. Mestvirishvili

Received July 12, 2005

The relativistic theory of gravity (RTG) as a field theory considers the gravitational field as a physical field with spins 2 and 0 propagating in the Minkowski space. The source of this field is a universal conserved quantity, namely, the energy momentum tensor of all the fields of the matter including the gravitational field. This very approach to gravity leads to a field-generated effective Riemannian space. Note that the effective Riemannian space has only a trivial topology. A test body moves in the Minkowski space under the action of a gravitational field, which is equivalent to the motion of the test body along a geodesic line of the effective Riemannian space. In the framework of this approach, the principle of least action implies the following complete system of equations of RTG [1, 2]:

$$R^{\mu\nu} - \frac{1}{2}g^{\mu\nu}R + \frac{m^2}{2}\left[g^{\mu\nu} + \left(g^{\mu\alpha}g^{\nu\beta} - \frac{1}{2}g^{\mu\nu}g^{\alpha\beta}\right)\gamma_{\alpha\beta}\right] = 8\pi T^{\mu\nu}, \quad (1)$$

$$D_\nu \tilde{g}^{\mu\nu} = 0. \quad (2)$$

Since the gravitational field acts in the Minkowski space with a metric tensor $\gamma_{\mu\nu}$, it should keep the motion of the test body inside the null cone of the Minkowski space. This is ensured by the causality conditions

$$g_{\mu\nu}U^\mu U^\nu = 0, \quad (3)$$

$$\gamma_{\mu\nu}U^\mu U^\nu \geq 0. \quad (4)$$

Here, U^μ is the isotropic four-vector of velocity in the effective Riemannian space, which corresponds to physical fields with zero rest mass.

Institute for High Energy Physics, ul. Pobedy 1, Protvino, Moscow oblast, 142284 Russia
e-mail: Anatoly.Logunov@ihep.ru

The time-like four-vector of velocity in the Riemannian space satisfying the relation

$$g_{\mu\nu}U^\mu U^\nu = 1, \quad U^\nu = \frac{dx^\nu}{ds},$$

where ds is an interval of the effective Riemannian space, corresponds to physical fields with nonzero rest mass.

The particle four-momentum is determined by the well-known equality

$$p^\nu = mcU^\nu.$$

According to the causality conditions (3) and (4), any time-like vector in the effective Riemannian space

$$g_{\mu\nu}U^\mu U^\nu = 1 \quad (5)$$

should also remain a time-like vector in the Minkowski space, i.e.,

$$\gamma_{\mu\nu}U^\mu U^\nu > 0. \quad (6)$$

Insofar as conditions (3) and (4) should also be valid for weak gravitational fields, in this case, according to the perturbation theory, we have

$$g_{\mu\nu} = \gamma_{\mu\nu} - \phi_{\mu\nu} + \frac{1}{2}\gamma_{\mu\nu}\phi, \quad \phi = \gamma_{\mu\nu}\phi^{\mu\nu}. \quad (7)$$

For a weak gravitational field such as a weak gravitational wave, condition (3) takes the form

$$\gamma_{\mu\nu}U^\mu U^\nu = \phi_{\mu\nu}\overset{0}{U}{}^\mu \overset{0}{U}{}^\nu. \quad (8)$$

Here, we take into account the equality $\gamma_{\mu\nu}\overset{0}{U}{}^\mu \overset{0}{U}{}^\nu = 0$. The right-hand side of equality (8) is not positive definite. Therefore, condition (4) may be violated. This is the reason why it is necessary to preclude the possibility that the equality

$$g_{\mu\nu}U^\mu U^\nu = 0 \quad (9)$$

will hold for any field, because this equality contradicts the causality conditions, which must be valid for all physical fields due to the universality of the gravitational field.

1028-3358/05/5012-0632$26.00

The causality principle was discussed in papers [3–6]. However, in that discussion, the counterarguments raised in papers [3–4] were not disposed of in full. In order to preclude any possibility of the violation of the causality principle, it is necessary to formulate the following general physical conclusion: all free physical fields including the electromagnetic field have a nonzero rest mass. This general physical conclusion of the RTG is in good agreement with the main Minkowski axiom [7]: "The space and time being properly defined, a substance located at any worldpoint can always be considered as staying at rest."

The axiom states that, at any worldpoint, the expression

$$c^2dt^2 - dx^2 - dy^2 - dz^2$$

is always positive or, in other words, that any velocity v is always less than c. Accordingly, c is the upper limit for supersubstantial velocities. This is the more profound meaning of the quantity c.

By virtue of our general physical conclusion, the causality conditions (3) and (4) are reduced to the following conditions:

$$g_{\mu\nu}U^\mu U^\nu = 1, \tag{10}$$

$$\gamma_{\mu\nu}U^\mu U^\nu > 0. \tag{11}$$

These very conditions were mentioned in paper [5] without due regard for equality (8).

In the case of a weak gravitational field, this gives us

$$\gamma_{\mu\nu}U^\mu U^\nu = 1 + \underset{0}{U}{}^\mu \underset{0}{U}{}^\nu\left(\phi_{\mu\nu} - \frac{1}{2}\gamma_{\mu\nu}\phi\right) > 0. \tag{12}$$

Here, $\underset{0}{U}{}^\nu = \dfrac{dx^\nu}{d\sigma}$ and $d\sigma$ is an interval of the Minkowski space

$$\gamma_{\mu\nu}\underset{0}{U}{}^\mu \underset{0}{U}{}^\nu = 1. \tag{13}$$

Thus, in accordance with (12), the time-like vector U^ν in the effective Riemannian space also remains time-like in the Minkowski space. This means that the null cone of the effective Riemannian space is contained within the null cone of the Minkowski space. Therefore, constant c involved in the expression for the interval of the Minkowski space

$$d\sigma^2 = c^2dt^2 - dx^2 - dy^2 - dz^2 \tag{14}$$

is a universal constant combining the space and time into a unified space-time continuum. It always remains an unattainable upper limit for the velocity of motion of any kind of matter. The fact that this conclusion follows from the RTG is due to the universality of gravity, which implies that its physical requirements should hold for all free physical fields.

ACKNOWLEDGMENTS

The authors express their gratitude to V.A. Petrov, A.N. Tavkhelidze, N.E. Tyurin, and Yu.V. Chugreev for fruitful discussions.

REFERENCES

1. A. A. Logunov and M. A. Mestvirishvili, *The Relativistic Theory of Gravitation* (Nauka, Moscow, 1989) [in Russian].
2. A. A. Logunov, *The Theory of Gravitational Field* (Nauka, Moscow, 2001) [in Russian]; *The Theory of Gravity* (Nauka, Moscow, 2001); gr-qc/0210005 (2002).
3. J. B. Pitts and W. C. Schieve, Gen. Relativ. Gravit. **33**, 1319 (2001).
4. J. B. Pitts and W. C. Schieve, gr-qc/0111004 (2001).
5. A. A. Logunov and M. A. Mestvirishvili, gr-qc/0106055 (2001).
6. Yu. V. Chugreev, Teor. Mat. Fiz. **138** (2), 349 (2004).
7. H. Minkowski, Phys. Z. Sowjetunion **10**, 104 (1909); in *The Principle of Relativity* (Dover, New York, 1952; Atomizdat, Moscow, 1973).

Translated by A. Pankrat'ev

Doklady Physics, Vol. 50, No. 12, 2005, pp. 634–638. Translated from Doklady Akademii Nauk, Vol. 405, No. 6, 2005, pp. 755–759.

PHYSICS

Genome as a Two-Dimensional Walk

S. A. Larionov, A. Yu. Loskutov, and E. V. Ryadchenko

Presented by Academician A.R. Khokhlov April 22, 2005

Received April 26, 2005

The problem of the identification and biological significance of chromosome fragments and complete genomes is approached on the basis of the representation of a sequence of DNA nucleotides as a two-dimensional walk. Self-similarity properties have been analyzed; similar fragments of chromosomes, as well as some known functional and structural elements, have been distinguished. Completely and partially decoded chromosomes have been considered; in particular, fragments of the 22nd chromosome of a human and a chimpanzee have been compared.

It is well known that DNA is a macromolecular complex in the form of a double helix consisting of two strands of nucleotides that are connected via hydrogen bonds. Nucleotides are low-molecular compounds that consist of nitrogen bases (purines and pyrimidines), carbohydrates (ribose or deoxyribose), and a phosphate group. Molecules of DNA contain two different purines, namely, adenine (*A*) and guanine (*G*), as well as two pyrimidines, namely, cytosine (*C*) and thymine (*T*). Each pair of nucleotides on opposite complementary strands is associated by hydrogen bonds: a guanine–cytosine pair, by three hydrogen bonds; an adenine–thymine, by two bonds. The phosphate groups run along the outside, while nitrogen bases run inside, so that their planes are perpendicular to the axis of the molecule. Each branch of the helix consists of nucleotide units linked together to form a long polynucleotide strand, which is conventionally represented as a string of characters drawn from the so-called nucleotide alphabet *ATTGCCAA*… and considered as the DNA sequence. A double-strand molecule of DNA linked with some proteins and organized in a certain hierarchical manner forms a chromosome.

The term genome is used for the complete set of the whole-cell DNA, i.e., the complete sequence of nucleotides.

It is conventionally assumed that the main function of DNA is to carry, process, and reproduce information, as well as to adapt to a dynamic environment by means of evolution. Moreover, these processes should operate on the basis of the information carried by the very same sequence; this imposes specific restrictions on the organization of DNA.

The organization of sequences of various DNA fragments and their functional meaning is currently an important and urgent problem. The point is that, by now, a considerable number of sequenced chains of genomes have been obtained; however, the functional organization of these sequences has yet to be explained.

In this paper, we suggest a method that makes it possible to present the whole chromosome (even if it contains more than one million nucleotides) in a compact form, to easily find similar fragments, to identify functional and structural elements, and to detect the self-similarity of some fragments of the DNA sequence. The method is based on the representation of DNA as a plane walk of a particle.

Represent the sequence of nucleotides as a plane walk on a square lattice starting from the origin (0, 0) in the following way. Read the nucleotide chain in the order of appearance of the bases *A*, *T*, *G*, and *C*. In encountering adenine (*A*), make a step right, when thymine (*T*), a step left, when guanine (*G*), a step up, and when cytosine (*C*), a step down. Denote these coordinates by *AGTC* moving counterclockwise from the *x*-axis. Then, the original sequence of nucleotides corresponds to a certain *walking trajectory* on the plane *AGTC*. This representation of DNA is composed of two sequences *A–T* and *G–C*, which cannot be reduced to each other. The sequences may be considered separately and, moreover, may be represented as time series. The series, in turn, may be studied by well-known methods of calculus, such as wavelet transformation.

This method seems to be mentioned for the first time in 1962 by S.W. Golomb, one of the pioneer investigators of the genome, in [1], where he represented the DNA sequence on the complex plane by associating the nucleotide types with the coordinate vectors. However, at the time, the DNA code had not been discovered in full. Twenty years later, small sequences of the decoded DNA were considered as plane walks [2, 3]. There, the choice of the coordinates *G–C* and *A–T* was determined by considerations of the complementarity of the strands by the balance of hydrogen bonds along the strand. This

Moscow State University,
Vorob'evy gory, Moscow, 119992 Russia
e-mail: Loskutov@chaos.phys.msu.ru

1028-3358/05/5012-0634$26.00

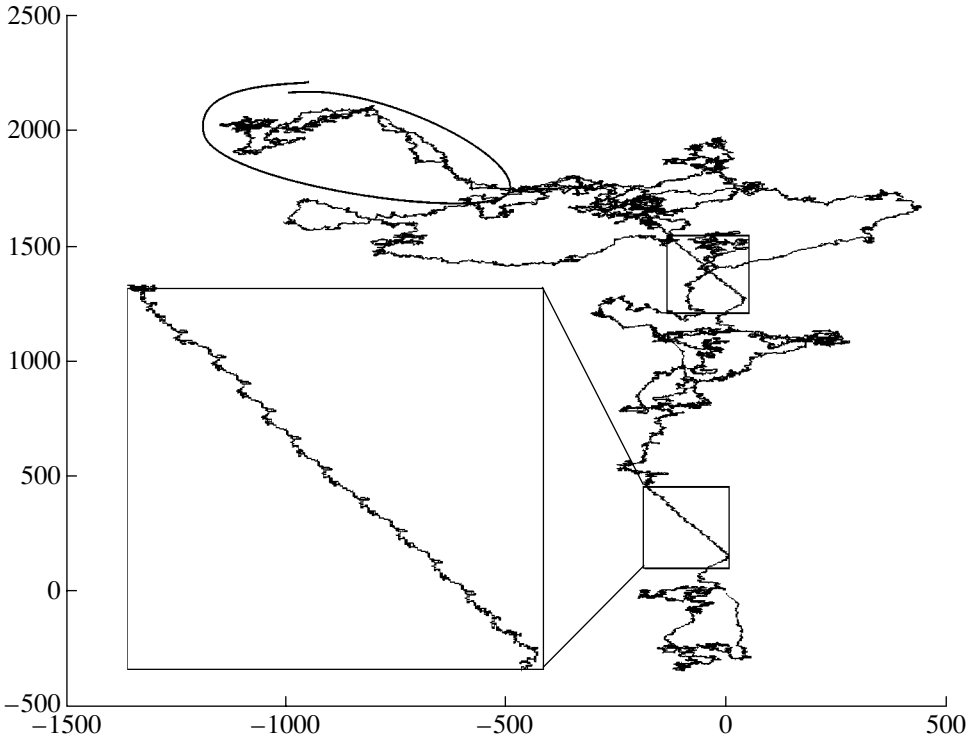

Fig. 1. *AGTC*-representation of the first chromosome of *S. cerevisiae.*

approach was subsequently provided with a strict justification (see, for instance, [5]).

Obviously, there are many sequences that may be considered as plane walks; then, there arise fractal structures that may be studied, etc. (see [6, 7] and references therein). However, as applied to DNA, functional and structural fragments of a chromosome may be distinguished by a typical walk "pattern" only for a sufficiently large number of units. Moreover, the number of units in the sequence of nucleotides may be of the same order of magnitude as the length of the sequence of the whole chromosome. Earlier, it seemed impossible to perform identification by this method with the use of only small fragments of chromosomes. The other methods of identification based on the alignment algorithms are rather labor-intensive and are not so demonstrative. It is from this viewpoint that *ATGC* sequences are considered in this paper.

Moreover, modern computer techniques allow automated processing by this method. One tentative attempt has already been made by a group of researchers (see [4]), who considered a somewhat different version of the plane walk. The authors formally used the method of a two-dimensional walk to construct an algorithm for comparing sequences. However, typical walk patterns, which might be crucial for understanding the organization of the structure of the sequence of chromosomes and its properties, had not been analyzed.

Today there are only a few species of living organisms for which the sequences of DNA of all their chromosomes have been completely decoded. Among them is the yeast cell *Saccharomyces cerevisiae*, by whose example we illustrate the analysis of the *AGTC* map.

Figure 1 shows the first of its 16 chromosomes, which contains approximately 230000 nucleotides. Almost identical large fragments (the square selections) are seen by the naked eye. Moreover, it follows from the construction that these fragments are passed in the opposite directions. This suggests that the fragments are complementary. Note that the length of each fragment is approximately 4000 units, which means that the use of another method (such as the alignment) for distinguishing these fragments would require incomparably greater investigative resources. These fragments are representatives of the family of flocculation genes FLO1 and FLO9 in the subtelomeric region.

Consider one of these fragments in more detail (see the insert to Fig. 1). It is seen to have an almost periodic spatial structure. Decompose this fragment into components (*A*–*T*) and (*G*–*C*). The wavelet transformation applied to these components explicitly shows that the selected fragment also possesses the property of self-similarity.

Employing the method of two-dimensional walk, one can easily find huge palindromes with a considerable share of pseudorandom inclusions. One of these is selected at the top left of Fig. 1. Its total length

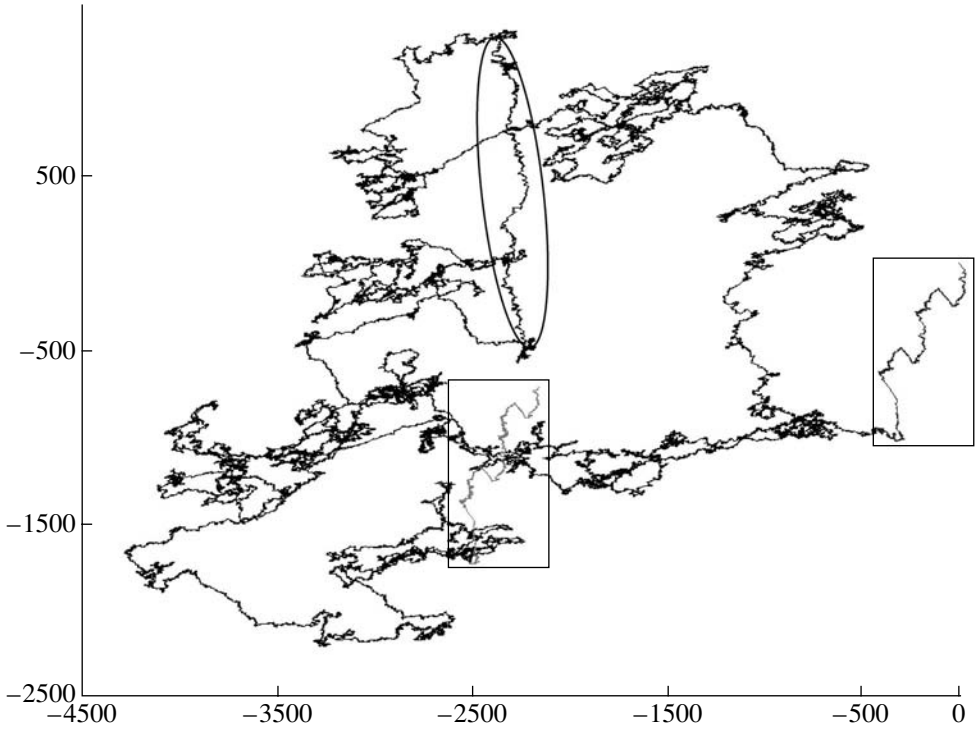

Fig. 2. Telomeres (the rectangles) of the 12th chromosome of *S. cerevisiae* and the cluster of ribosomal RNAs (the ellipse).

is 35000 nucleotides. Such a fragment cannot be identified by other methods; and even if it could, it would then require, at the least, an additional careful examination. This is the region with mobile genome transpositions represented by the *Ty*-family of retrotransposons.

Moreover, it is easy to identify telomeres. Figure 2 shows the 12th chromosome of the same yeast cell *Saccharomyces cerevisiae*. The telomeres are located at its ends; they are selected by rectangles. Each fragment has a size of approximately 20000 nucleotides. It is not difficult to visually detect similar fragments in other chromosomes without performing any statistical analysis. Note that these fragments are complementary.

The most indicative elements of this representation are the fragments in which the trajectory concentrates within a certain domain of the *ATGC* plane, skews, and long curved fragments of various shapes (see Figs. 1 and 2).

It is obvious that, throughout long skews, certain nucleotides dominate in the sequence. This is clearly seen in Fig. 2, where such a fragment is selected by an ellipse (here, the cluster of ribosomal RNAs is located). What is identified here is either satellite sequences or the averaged selected concentration of nucleotides without specific motifs, which may be seen by scaling up the observed fragment. In view of the different concentrations of purines and pyrimidines, the slope of this fragment suggests that the complementary strands of the DNA helix are of unequal weight (size) and anisotropic. Therefore, it appears interesting to investigate the length and directional distribution of the skews.

Fix a frame of the size N nucleotides with due regard for the appropriate scale and consider the motion of this frame along the walking trajectory on the *AGTC*-plane with the step of one nucleotide. Construct the diagram of such a motion in the coordinate system *AGTC* as follows. At each step of the motion, fix the radius vector that joins the beginning and the end of the frame. This radius vector is characterized by its length and direction. Plot the end of this radius vector on the diagram. Then, moving the frame by one step, we obtain a new radius vector. Plot its end on the diagram and proceed further in the same way. We thus obtain a plane diagram (Fig. 3). Each point i of this diagram ($0 < i < M - N$; M is the number of nucleotides in the sequence; and N is the size of the frame) shows how far and in which direction the representative point has moved from the beginning of the ith segment in N steps. This construction makes it possible to easily distinguish fragments of the domination of certain nucleotides. In particular, the outliers (see Fig. 3) characterize the direction and the length of the observed skews. Obviously, for each sequence, there exists a specific indicative size of the frame.

Finally, with the use of the above representation, one can easily compare sufficiently long fragments of chromosomes of different organisms. For a human and a chimpanzee, such a comparison has recently been made by a team of authors [8] by means of alignment.

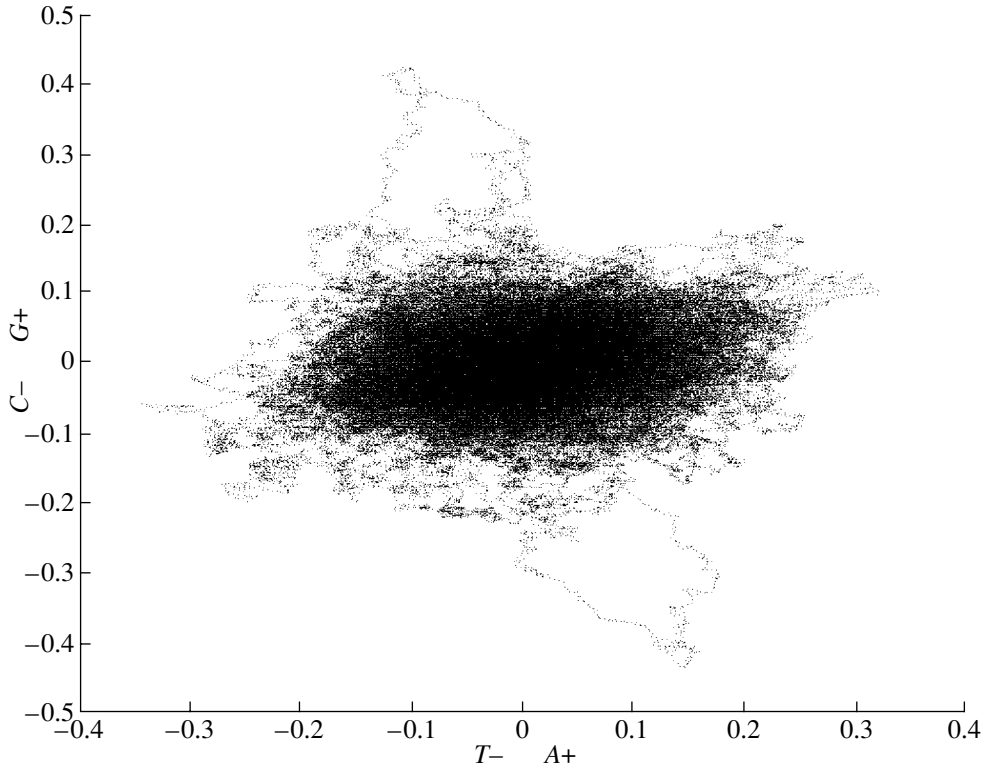

Fig. 3. Normalized length distribution of the 12th chromosome of *S. cerevisiae.*

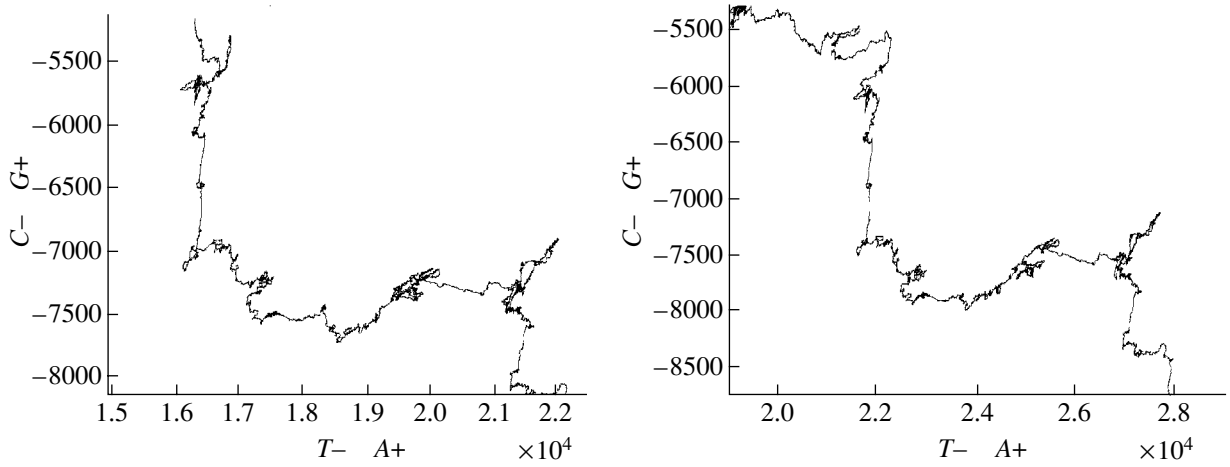

Fig. 4. Fragment (1934000–2134000) of the human 22nd chromosome (on the left) and the fragment (2176500–2376500) of the chimpanzee 22nd chromosome (on the right). They are seen to be almost identical.

Although the method of alignment constants is rather efficient, detection of similar fragments turns out to be quite labor-intensive, especially with account for the large number of missing fragments. At the same time, the above-described method enables us to easily render the general sequence fragmented for further alignment. Figure 4 presents the fragment (1934000–2134000) of the human 22nd chromosome compared with the fragment (2176500–2376500) of the chimpanzee 22nd chromosome. These fragments are seen to be almost identical.

The application of the above-described treatment of DNA as a random walk is much broader than simply the identification and comparison of fragments. Combined with other modern methods (such as fractal and Fourier analysis [9], wavelet transformation [10], the sliding

window method, etc.), it enables one to carry out a detailed fragmenting and, being rather demonstrative, becomes an instrument for advancing and testing the hypotheses on the organization of complete genomes and their properties.

REFERENCES

1. S. W. Golomb, in *Mathematical Problems in the Biological Sciences*, Ed. by R. Bellman (Amer. Math. Soc., Providence, 1962; Mir, Moscow, 1966).
2. M. A. Gates, Nature **316**, 219 (1985).
3. M. A. Gates, J. Theor. Biol. **119**, 319 (1986).
4. P. Vincens, L. Buff, C. Andre, *et al*., Bioinformatics **14**, 715 (1998).
5. Ch. Berthelsen, J. A. Glazier, and M. H. Skolnik, Phys. Rev. A **45**, 8902 (1992).
6. G. Abramson, P. A. Alemany, and H. A. Cerdeira, Phys. Rev. E **58**, 914 (1998).
7. A. Rosas, E. Nogueira, and J. F. Fontanari, cond-mat/0209396.
8. H. Watenabe, A. Fujiyama, M. Hattori, *et al.*, Nature **429**, 382 (2004).
9. V. V. Lobzin and V. R. Chechetkin, Usp. Fiz. Nauk **170**, 57 (2000) [Phys. Usp. **43** (1), 55 (2000)].
10. A. Arneodo, Y. D. Aubenton-Carafa, B. Audit, *et al.*, Physica A (Amsterdam) **249**, 439 (1998).

Translated by A. Pankrat'ev

Doklady Physics, Vol. 50, No. 12, 2005, pp. 639–643. Translated from Doklady Akademii Nauk, Vol. 405, No. 6, 2005, pp. 760–764.

TECHNICAL PHYSICS

Laws of the Synthesis and a Model of the Growth of Single-Walled Carbon Nanotubes in a Jet of Laser Ablation Products

G. I. Kozlov and V. A. Kuznetsov

Presented by Academician D.M. Klimov June 7, 2005

Received March 29, 2005

The development of efficient methods for the self-organized synthesis of single-walled carbon nanotubes (SWCNTs) and other functional molecular structures with given characteristics is of great interest. An SWCNT is a unique fiber molecular structure with an extreme strength capacity, high heat conductivity, and high electrical conductivity and is considered to be a key element of nanotechnology [1–7]. At present, the potential areas of their application require the production of large amounts of SWCNTs with given properties (semiconducting, thermal mechanical, etc.). However, the solution to this problem directly depends on an understanding of the mechanisms of the nucleation and growth of SWCNTs, which are not yet clear.

In this paper, we present the results of an experimental investigation into the optimum conditions for the synthesis of SWCNTs in a jet of products of the laser ablation of graphite with a catalyst. Among the available methods for the synthesis of SWCNTs, the laser ablation method stands out due to an increased content and primarily to the high crystallinity and quality of SWCNTs. The optimization of the synthesis of SWCNTs in a laser torch makes it possible not only to increase the efficiency of this process, but also to propose new approaches to determining mechanisms of the nucleation and growth of SWCNTs. In particular, a mechanism of the growth of nanotubes that is based on their self-organized formation by a wave of a strong electric field localized at the edge of a growing nanotube is proposed for the first time. Such a model of the process enables one to derive an analytical expression for the nanotube growth rate.

In our experiments concerning the synthesis of SWCNTs by the laser ablation method, the radiation of a CW gas-discharge 2-kW CO_2 laser passed through a salt window inside the helium-filled quartz reaction tube and was focused by a lens on the end surface of the cylindrical graphite target containing a catalyst [4]. Owing to the action of CW laser radiation, the target is gasified with the formation of a jet of the ablation products. As this jet expands and the vapor–gas–plasma flow is correspondingly cooled, the saturation state is achieved in the jet at a certain time, and then, with further cooling, vapor in the flow becomes supersaturated. Since the state of supersaturated vapor is instable with respect to the formation of the condensed phase, the liquid disperse phase is synthesized in the form of nanosized droplets of the catalyst metal with carbon, which provides favorable conditions for the nucleation of SWCNTs. Condensate particles formed in the vapor–gas phase were precipitated on substrates placed in the reaction tube. Figure 1 shows a microphotograph of such a condensate, which was obtained by a scanning electron microscope. This photograph is very informative and its analysis raises many questions, primary among which are the following: Why do SWCNTs grow predominantly in the form of bundles? What is the role of the catalyst metal? What are the factors deter-

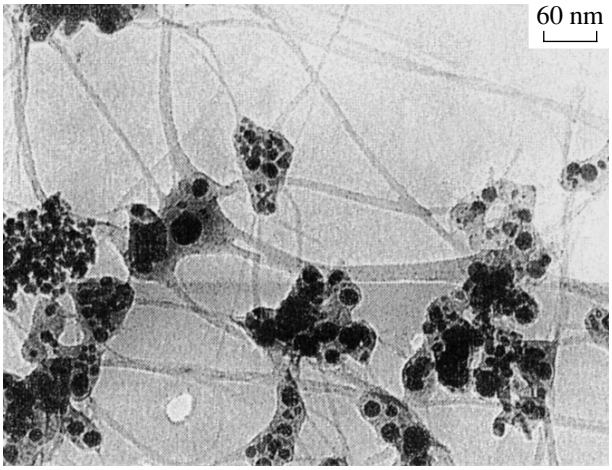

Fig. 1. Microphotograph of single-walled nanotubes that was obtained by a scanning electron microscope.

Institute for Problems in Mechanics,
Russian Academy of Sciences,
pr. Vernadskogo 101, Moscow, 119526 Russia
e-mail: kozlov@ipmnet.ru

1028-3358/05/5012-0639$26.00

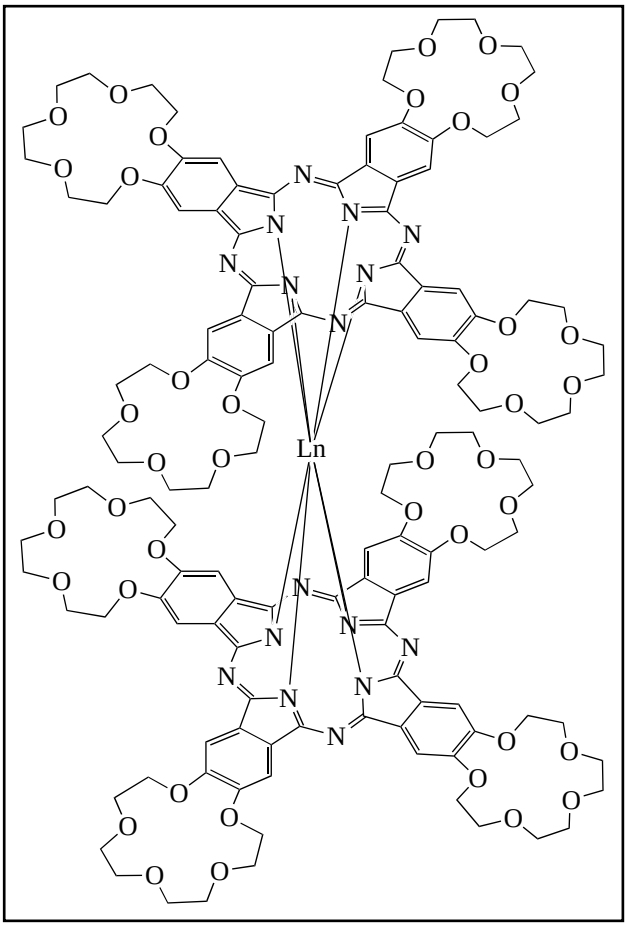

Fig. 2. Schematic picture of the structure of a synthesized supramolecular system.

mining the diameter and chirality of SWCNTs? What is the mechanism of growing SWCNTs?

According to the analysis of microphotographs, the sequence of processes leading to the synthesis of SWCNTs is as follows. First, in the process of expansion, condensation nuclei are formed from clusters in the cooled vapor–gas–plasma flow and grow up to liquid supercritical-size drops 10–30 nm in diameter. At the next, most important, stage in the development of the process, these drops are crystallized with the formation of seed particles. Since the molecular structure of these particles is of fundamental importance, the further careful electron microdiffraction study of this structure is planned. It is assumed that this structure is similar to that of so-called supramolecular systems. Figure 2 schematically shows the molecular structure of one such complex that has been synthesized to date. The characteristic structural feature of these complexes is that the atoms of the transition metal elements that are located at the center of a complex tend to surround themselves with complex molecular circular blocks formed from nonmetal atoms, e.g., carbon. Some of these blocks that appear on the seed particle surface in the process of crystallization are catalytically active and promote the nucleation and initial growth of SWCNTs. The parameters of these blocks likely determine the diameter and chirality of synthesized SWCNTs and their distinctive growth in the form of bundles. Thus, the catalyst metal without which SWCNTs do not grow is necessary only for the nucleation of a nanotube and then the structure grows according to the program that is determined by the configuration of the coupling orbitals localized at the edge of the growing nanotube and is sequentially cloned itself.

In general, on these catalytically active centers, other carbon modifications, along with SWCNTs, including disordered amorphous carbon, fibers, polyhedral particles, etc., can be formed depending on the realized conditions. However, it appears that favorable conditions for the synthesis of SWCNTs arise only in the case of relatively small catalyst particles with diameters of 10–20 nm. As the size of particles increases, the growth of multiwalled nanotubes first occurs and then carbon fibers begin to grow [7]. This behavior implies an important conclusion: when synthesizing SWCNTs, it is necessary to avoid the formation of large drops, which requires large supersaturations in the vapor–gas jet in short time intervals even at the initial stage in the development of the process in order to synthesize numerous small droplets in the jet. Analysis of the Raman spectra of the synthesized material [8–10] shows that the diameter of nanotubes is determined only by the type of the catalyst and is independent of its dispersion and its content in the mixture. This indirectly corroborates our conclusion that the nucleation and parameters of formed SWCNTs are determined by the molecular structure of seed particles.

When using the laser ablation method, the optimum conditions for synthesizing SWCNTs with a mean diameter of 1.3–1.4 nm are ensured by using the $Ni:Y_2O_3$:C catalyst mixture with the component weight ratio 1 : 1 : 6 and buffer gaseous helium at a pressure of 700 mbar [4, 9]. When the content of nickel decreases below the above-indicated ratio, the intensity of the *D* mode in the Raman spectrum of the synthesized material increases, indicating that carbon is disordered and the content of the amorphous phase increases. It was found that the 1 : 1 ratio of Ni and Y_2O_3 in the mixture is favorable for the optimum content of yttrium oxide in the catalyst mixture. An increase in the content of yttrium oxide does not affect the quality of SWCNTs and a decrease in this content in the mixture gives rise to an increase in the formation of amorphous carbon. Instead of nickel and yttrium oxide, other transition metals can evidently be used. In particular, if Pd or Fe is used as the catalyst, the diameter of the synthesized SWCNTs decreases. Unfortunately, this decrease is accompanied by a decrease in the content of carbon nanotubes in the synthesized material. For example, their content in the condensate reaches 20% when

nickel is used as the catalyst, whereas the yield of SWCNTs does not exceed 5% if iron is used as the catalyst.

As was mentioned above, when SWCNTs are synthesized by the method of the laser ablation of the carbon target containing the catalyst, a slightly ionized vapor–gas jet is formed. Seed nanoparticles appearing in the laser torch are effective electron-capture centers, but the charge gained by them cannot be large in contrast to micron and submicron particles. A question arises as to how these charges affect the laws of the self-organized growth of SWCNTs. In the present work, a model of growing SWCNTs in the vapor–gas flame is proposed for the first time that allows for the evaluation of the nanotube growth rate, which is very important for realizing the controlled synthesis of SWCNTs.

We consider how a nanotube can grow in the laser torch. Let seed particles be formed in the periphery jet region, where temperature decreases and condensation occurs. Electrons appearing in the jet adhere to these particles and are distributed over their surface and edge. Charges localized at the circular edge of the growing nanotube generate the following electric field in the surrounding space:

$$E = \frac{e}{4\pi\varepsilon_0 r^2}, \quad (1)$$

where ε_0 is the permittivity of free space, r is the distance from the nanotube edge, and charges are assumed to be quite uniformly distributed over the cylindrical section of the nanotube with a density of one elementary charge e per several structural hexagons. Estimates show that the field even from one elementary charge at a distance of 10 Å from the section of the nanotubes is equal to 1.5×10^9 V/m; i.e., it is very strong. It decreases rapidly but remains quite strong even at a distance of, e.g., 100 Å (approximate intermolecular spacing in the vapor–gas jet). Thus, the strong electric field, which provides two functions important for growing nanotubes, is localized on the section of the growing nanotube. First, it induces the following dipole moment in neighboring molecules:

$$p_e = \alpha\varepsilon_0 E. \quad (2)$$

Here, α is the polarizability of molecules, which is related to the dielectric constant ε as $\varepsilon = 1 + \alpha n$, where n is the carbon molecular density. Second, in the nonuniform electric field, an electric dipole is drawn to the stronger field region, i.e., towards the edge of the growing nanotube. Thus, the drift of carbon molecules and their clusters with induced electric dipoles in the gradient electric field creates a flow of dipoles to the section of the nanotube channel and determines its growth rate. Dipoles, as well as gas molecules, have a disordered velocity. We assume that the drift velocity after the collision of a dipole with a molecule is equal to zero and that, between collisions, the dipole is accelerated by the electric field and moves as in high vacuum. In this case, the drift velocity v_d of the dipole with mass m in the electric field can be determined from the equation of motion of the dipole toward the edge of the growing SWCNT:

$$m\frac{dv_d}{dt} = \alpha\varepsilon_0 E\frac{dE}{dr}. \quad (3)$$

Integrating this equation, we arrive at the following expression for the drift velocity:

$$v_d = \sqrt{\frac{\alpha\varepsilon_0}{m}}E = \mu E. \quad (4)$$

Here, μ is the mobility of molecules with the induced dipole moment. We emphasize that graphite is thermodynamically instable and dissociates in a laser torch at temperatures above 2600 K. In this case, single bonds in the graphene layer are broken with the formation of either C_2 or C_3 molecules [11]. However, we assume for simplicity that the basic component in the laser torch is C_2 molecules. The inclusion of C_3 molecules does not change the main conclusions.

Since molecules move chaotically, i.e., all spatial directions are identical for them, it may be thought that only one-sixth of all carbon molecules on average move toward the edge of the nanotube. It follows from the kinetic theory of gases that the fraction of these molecules that undergo collisions in the mean free path λ is equal to 0.63. Therefore, the flux j of the carbon molecules drifting in the direction of the edge of the nanotube with radius r_t is represented as

$$j = 0.63\frac{n}{6}\pi r_t^2 v_d. \quad (5)$$

Let all the molecules of this flux be placed by molecular forces into a newly forming section of the nanotube, as is schematically shown in Fig. 3. Since the bond length, i.e., the distance between carbon atoms in the nanotube structure, is equal to $a = 1.42$ Å, $\frac{2\pi r_t}{a}$ carbon atoms are required for the formation of one atomic layer of the growing nanotube. Correspondingly, the linear growth rate of a SWCNT in the laser torch is given by the expression

$$u = 0.1 n r_t v_d a^2. \quad (6)$$

Since the electric field decreases rapidly as the distance from the nanotube edge increases, it is reasonable

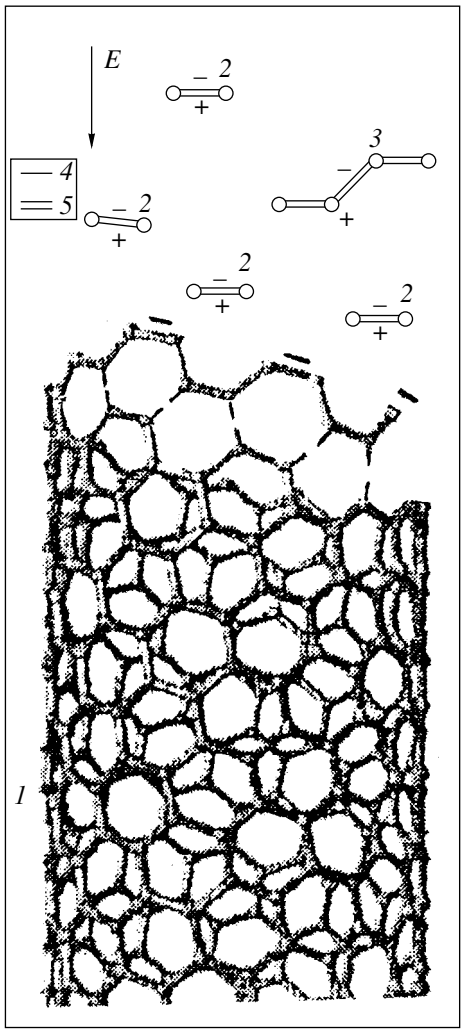

Fig. 3. Schematic picture of the process of the self-organized integration of molecules and clusters into the newly formed section of a growing nanotube: (*1*) growing single-walled nanotube, (*2*) C_2 radical, (*3*) molecular clusters, (*4*) electrons adhere to nanotubes, and (*5*) forming molecular bonds.

to replace v_d depending on the distance from the edge by the average drift velocity $\bar{v}_d$ of a molecule in the distance range from a to λ:

$$\bar{v}_d = \frac{1}{\lambda}\int_a^\lambda v_d(r)dr. \quad (7)$$

Substituting Eqs. (1) and (4) into this expression and performing the integration, we obtain

$$\bar{v}_d = \frac{B}{\lambda a}, \quad B = \frac{e}{4\pi}\sqrt{\frac{\alpha}{m\varepsilon_0}}. \quad (8)$$

Substituting the expression obtained for the average drift velocity into Eq. (6), we arrive at the following final expression for the growing velocity of the SWCNT in the laser torch jet:

$$u = 0.025\frac{ear_t}{\pi\lambda}\sqrt{\frac{n(\varepsilon-1)}{m\varepsilon_0}}. \quad (9)$$

This formula expresses fundamental relations between various parameters determining the self-organized synthesis of carbon nanotubes. It is interesting to estimate the nanotube growth rate for the conditions of our experiment [4, 6] concerning the synthesis of carbon nanotubes by the method of laser ablation of graphite with a catalyst for a pressure of 1 atm and a temperature of about 2000 K in the reaction space. Unfortunately, we do not know the polarizability or mean free path of C_2 molecules. For this reason, we obtained the below estimates with the respective values ε and λ for nitrogen molecules. In addition, the carbon molecule density in the vapor–gas flame was assumed to be 50% and the parameters entering into Eq. (9) were taken as $e = 1.62 \times 10^{-19}$ C, $\varepsilon = 1.00059$, $\lambda = 5.9 \times 10^{-5}$ cm, $\varepsilon_0 = 8.85 \times 10^{-12}$ C^2/(N m^2), $m = 24 \times 1.66 \times 10^{-27}$ kg, $r_t = 0.7 \times 10^{-9}$ m, $a = 1.42 \times 10^{-10}$ m, and $n = 2 \times 10^{24}$ m^{-3}.

Formula (9) with these parameters yields a value of about 1.3×10^{-3} cm/s. Unfortunately, direct measurements of the linear growth rate for SWCNTs have not yet been reported. In our experiments on the synthesis of SWCNTs, the length of the reaction zone was equal to 2–3 cm and the average velocity of the ablation product flux was equal to 5×10^{-2} s. For this time, the length of synthesized nanotubes may increase with the above-calculated rate to 6.5×10^2 nm, which is in good agreement with the maximum length of nanotubes in the photograph shown in Fig. 1. The comparison of calculation and experiment evidently requires direct measurements of the growth rate of SWCNTs in the process of synthesis, but these measurements are very difficult and will not likely be performed in the near future. For this reason, the most realistic way to determine the nanotube growth kinetics is to determine the length of synthesized SWCNTs as a function of the reaction time. We will solve this problem at the next stage of the study. In conclusion, we note that, in the framework of the above model, the cessation of the growth of nanotubes can be caused by the neutralization of charges at the edge of a growing nanotube due to recombination processes.

ACKNOWLEDGMENTS

This work was supported in part by the Russian Foundation for Basic Research (project no. 02-01-00452).

REFERENCES

1. S. Iijima, Nature **354**, 56 (1991).
2. A. Thess, R. Lee, P. Nikolaev, *et al.*, Science **273**, 483 (1996).
3. W. K. Maser, E. Munoz, A. M. Benito, *et al.*, Chem. Phys. Lett. **292**, 587 (1998).
4. G. I. Kozlov and I. G. Assovskiĭ, Zh. Tekh. Fiz. **73** (11), 76 (2003) [Tech. Phys. **48**, 1436 (2003)].
5. I. G. Assovskiĭ and G. I. Kozlov, Dokl. Akad. Nauk **388** (3), 349 (2003).
6. G. I. Kozlov, Pis'ma Zh. Tekh. Fiz. **29** (18), 88 (2003) [Tech. Phys. Lett. **29**, 272 (2003)].
7. E. G. Gamaly and T. W. Ebbesen, Phys. Rev. B **52**, 2083 (1995).
8. H. Kataura, Y. Kumazawa, Y. Maniwa, *et al.*, Carbon **38**, 1691 (2000).
9. A. C. Ferrari and J. Robertson, Phys. Rev. B **61** (20), 14095 (2000).
10. V. N. Bezmel'nitsyn, A. G. Dolmatovskiĭ, A. V. Eletskiĭ, *et al.*, Fiz. Tverd. Tela (St. Petersburg) **44** (4), 630 (2002) [Phys. Solid State **44**, 656 (2002)].
11. A. G. Whittaker, Science **200**, 763 (1978).

Translated by R. Tyapaev

Doklady Physics, Vol. 50, No. 12, 2005, pp. 644–649. Translated from Doklady Akademii Nauk, Vol. 405, No. 4, 2005, pp. 479–483.

MECHANICS

Modeling of a Weak Inhomogeneity in the Eulerian Description of a Continuum

D. V. Georgievskiĭ

Presented by Academician D.M. Klimov June 7, 2005

Received June 9, 2005

We describe the process of the deformation of a weakly inhomogeneous (at the initial instant) continuum by an asymptotic method with the process in the homogeneous medium taken as the zeroth approximation. Our primary interest is in the deviation of the particle trajectories in the disturbed process from those in the corresponding undisturbed process. Deviation measures and a classification of the disturbed motion in terms of these measures are proposed. The trajectory approach is illustrated through the example of the plane problem of spreading of a radially inhomogeneous incompressible ideally plastic tube under the pressure drop between the inner and outer surfaces.

1. An inhomogeneous medium is known to refer to a medium whose density and material functions of the constitutive relations are coordinate-dependent. If these dependences are discontinuous in coordinates, then the body is a composite [1]. Denote some material function characterizing the continuum by $\Lambda(\mathbf{x}, t)$; this function may be a time-dependent field—scalar, vector, or tensor. In the Eulerian description of the motion, the coordinate dependence of the material functions can be of two types. Let us focus on these two types in more detail.

1°. The quantity $\Lambda(\mathbf{x}, t)$, as well as density $\rho(\mathbf{x}, t)$, is a known function of $\mathbf{x}$ and t. This takes place in the following case. The material functions may depend on external fields, e.g., temperature, humidity, radiation dose, and electromagnetic quantities. For instance, there are many known empirical temperature dependences of the dynamic viscosity of a fluid or empirical dependences of the Young modulus of an elastic material on the radiation exposure intensity. If these external fields are given, then the material functions are also known. In this case, the closed system of N equations (the equations of motion, the continuity equation, the constitutive relations, etc.) involving N unknowns and describing the medium deformation within a certain time-dependent domain Ω_t with a boundary $\Sigma_t = \partial\Omega_t$ (system A_N) is closed in Ω_t.

2°. The physical and mechanical properties of the medium at each point $\mathbf{x}$ of the space at instant t are the properties of the Lagrangian particle that resides at this point at this instant [2]. Since either the law of motion or the particle trajectories are not known in advance, the dependences of the density and material functions on $\mathbf{x}$ and t are also unknown. For an incompressible medium, the continuity equation and the incompressibility condition imply the equation $\dfrac{d\rho}{dt} = 0$ with the first integral

$$\rho(\mathbf{x}, t) = \rho(\mathbf{x}_0, 0) \equiv \rho^0(\mathbf{x}_0). \tag{1}$$

Assume that function $\Lambda(\mathbf{x}, t)$, as well as the density of the incompressible material, is preserved under the mass transfer [3–5], that is

$$\Lambda(\mathbf{x}, t) = \Lambda(\mathbf{x}_0, 0) \equiv \lambda(\mathbf{x}_0). \tag{2}$$

Then, the equalities of system A must be supplemented with the following three equations:

$$\frac{d\mathbf{x}}{dt} = \mathbf{v}(\mathbf{x}, t), \quad \mathbf{x}(0) = \mathbf{x}_0, \tag{3}$$

which determine the law of motion of the particles

$$\mathbf{x} = \mathbf{x}(\mathbf{x}_0, t). \tag{4}$$

Reversing this law, we can determine the inverse law of motion

$$\mathbf{x}_0 = \mathbf{x}_0(\mathbf{x}, t) \tag{5}$$

and substitute it into Eqs. (2) and (3) with the result that the functions $\rho^0(\mathbf{x}_0(\mathbf{x}, t))$ and $\lambda(\mathbf{x}_0(\mathbf{x}, t))$ become known. Then, the values to be determined are supplemented with the vector $\mathbf{x}(\mathbf{x}_0, t)$ or $\mathbf{x}_0(\mathbf{x}, t)$, so that the total system includes $N + 3$ equations (system B_{N+3}). Note that system B_{N+3} cannot be divided into the independent subsystems A_N and (4) owing to the fact that ρ and Λ

Moscow State University, Leninskie Gory, Moscow, 119992 Russia
e-mail: georgiev@mech.math.msu.su

1028-3358/05/5012-0644$26.00

present in the equations of subsystem A_N are not known and are determined from Eqs. (1) and (2), which involve the inverse law of motion.

In order to formulate the initial-boundary value problem for the inhomogeneous flow of a continuum, the equations of system B_{N+3} in Ω_t should be supplemented with boundary conditions on Σ_t and with initial conditions at $t = 0$. Since the objects to be determined include the law of motion of the particles, the approach considered in item 2° is actually a Lagrangian–Eulerian one (the law of motion being known, it is not difficult to pass from the Eulerian to the Lagrangian description and vice versa).

Note the case of a plane motion of an incompressible medium when the velocity field $\mathbf{v}(\mathbf{x}, t)$ is solenoidal and it is possible to introduce a scalar stream function $\psi(\mathbf{x}, t)$ such that the Cartesian components v_1 and v_2 can be presented in the form $v_1 = \psi_{,2}$ and $v_2 = -\psi_{,1}$. In view of Eq. (3), we obtain

$$\frac{dx_1}{dt} = \frac{\partial \psi}{\partial x_2}, \quad \frac{dx_2}{dt} = -\frac{\partial \psi}{\partial x_1}. \tag{6}$$

The two equations (6) are mathematically identical to the Hamilton canonical equations for a system with a single degree of freedom, the role of the Hamilton function being played by the stream function (for this reason, it is sometimes called the Hamiltonian) and the role of the generalized coordinates and the momentum, by the Cartesian coordinates $x_1(t)$ and $x_2(t)$. Equations (6) hold for any plane incompressible continuum flow. Therefore, certain qualitative conclusions of Hamiltonian mechanics are quite applicable in continuum mechanics [6].

2. The fact that the material function Λ in the system of equations B_{N+3} is not specified as a function of the Eulerian coordinates and time but is determined from the inverse law of motion makes the problem of inhomogeneous flow rather complicated. If the initial distribution $\lambda(\mathbf{x_0})$ is slightly different from a certain function $\lambda^0(\mathbf{x_0})$, so that

$$\begin{aligned} \lambda(\mathbf{x_0}) &= \lambda^0(\mathbf{x_0}) + \alpha\lambda^1(\mathbf{x_0}) + \ldots, \\ \alpha &= \sup_{\mathbf{x_0} \in \Omega_0} \frac{\|\lambda(\mathbf{x_0}) - \lambda^0(\mathbf{x_0})\|}{\|\lambda^0(\mathbf{x_0})\|} \ll 1, \end{aligned} \tag{7}$$

where $\lambda^0(\mathbf{x_0})$, $\lambda^1(\mathbf{x_0})$, … are given, then one can use the asymptotic approach based on the expansion of all unknowns of system B_{N+3} as power series in a small parameter α, for example, $\mathbf{v}(\mathbf{x}, t) = \mathbf{v^0}(\mathbf{x}, t) + \alpha\mathbf{v^1}(\mathbf{x}, t) + \ldots$. The direct (4) and inverse (5) laws of motion can also be presented in the form of the series:

$$\mathbf{x}(\mathbf{x_0}, t) = \mathbf{X^0}(\mathbf{x_0}, t) + \alpha\mathbf{X^1}(\mathbf{x_0}, t) + \ldots, \tag{8}$$

$$\mathbf{x_0}(\mathbf{x}, t) = \mathbf{X_0^0}(\mathbf{x}, t) + \alpha\mathbf{X_0^1}(\mathbf{x}, t) + \ldots. \tag{9}$$

In these series,

$$\begin{aligned} \mathbf{X^0}(\mathbf{x_0}, 0) \equiv \mathbf{x_0}, \quad \mathbf{X^1}(\mathbf{x_0}, 0) \equiv 0; \\ \mathbf{X_0^0}(\mathbf{x}, 0) \equiv \mathbf{x}, \quad \mathbf{X_0^1}(\mathbf{x}, 0) \equiv 0; \end{aligned} \tag{10}$$

$$\frac{\partial \mathbf{X^0}}{\partial \mathbf{x_0}} \cdot \frac{\partial \mathbf{X_0^0}}{\partial \mathbf{x}} = \mathbf{I}, \quad \frac{\partial \mathbf{X^0}}{\partial \mathbf{x_0}} \cdot \frac{\partial \mathbf{X_0^1}}{\partial \mathbf{x}} = -\frac{\partial \mathbf{X^1}}{\partial \mathbf{x_0}} \cdot \frac{\partial \mathbf{X_0^0}}{\partial \mathbf{x}}, \tag{11}$$

where $\mathbf{I}$ is the second-rank identity tensor.

In view of Eq. (9), each of the known coefficients of series (7) can be expanded in a Taylor series, for example,

$$\begin{aligned} \lambda^0(\mathbf{x_0}) &= \lambda^0(\mathbf{X_0^0}(\mathbf{x}, t)) \\ &+ \alpha\frac{\partial \lambda^0}{\partial \mathbf{x_0}}(\mathbf{X_0^0}(\mathbf{x}, t)) \cdot \mathbf{X_0^1}(\mathbf{x}, t) + \ldots \end{aligned} \tag{12}$$

If the zeroth approximation in α for the function $\lambda^0(\mathbf{x_0})$ is a constant, then the medium under consideration is weakly inhomogeneous in the narrow sense. For the sake of generality, we assume that $\lambda^0(\mathbf{x_0})$ need not be identically equal to a constant. Such a medium will be called weakly inhomogeneous in the wide sense.

The system of equations in the $N + 3$ unknowns with zero superscript (system B^0_{N+3}) is identical in Ω_t with system B_{N+3} and corresponds to the deformation of a homogeneous body with the material constant λ^0 for a weak inhomogeneity in the narrow sense or with the material function $\lambda^0(\mathbf{x_0})$ for a weak inhomogeneity in the wide sense. We assume that the initial-boundary value problem for system B^0_{N+3} is easy to solve.

For the $N + 3$ unknowns with superscript 1, we have an already linearized system C^1_{N+3} involving quantities with zero superscript as known coefficients. This system corresponds to the deviation from the basic (undisturbed) process due to the initial disturbance of the medium by a weak inhomogeneity. It can be seen from Eq. (12) that all the material functions and their gradients in C^1_{N+3} are taken on the trajectories $\mathbf{X_0^0}(\mathbf{x}, t)$ determined from the basic process for the homogeneous material. Moreover, if $\lambda^0 \equiv \text{const}$, then system C^1_{N+3} can be divided into a subsystem D^1_N that is free of the components of vector $\mathbf{X_0^1}(\mathbf{x}, t)$ and three equations corresponding to Eq. (3), namely,

$$\begin{aligned} \frac{d\mathbf{X^1}}{dt}(\mathbf{x_0}, t) &= \mathbf{v^1}(\mathbf{X^0}(\mathbf{x_0}, t), t) \\ &+ \frac{\partial \mathbf{v^0}}{\partial \mathbf{x}}(\mathbf{X^0}(\mathbf{x_0}, t), t) \cdot \mathbf{X^1}(\mathbf{x_0}, t), \\ \mathbf{X^1}(\mathbf{x_0}, 0) &= 0. \end{aligned} \tag{13}$$

Solving the initial-boundary value problem for subsystem D_N^1, we determine the disturbed kinematic field $\mathbf{v^1}$; then, we integrate the linear inhomogeneous Cauchy problem (13) and determine the vector

$$\mathbf{X^1}(\mathbf{x_0}, t) = \int_0^t \mathbf{K}(\mathbf{x_0}, t, \tau) \cdot \mathbf{v}^1(\mathbf{X^0}(\mathbf{x_0}, \tau), \tau) d\tau, \quad (14)$$

where

$$\mathbf{K}(\mathbf{x_0}, t, \tau) = \exp \int_\tau^t \frac{\partial \mathbf{v^0}}{\partial \mathbf{x}}(\mathbf{X^0}(\mathbf{x_0}, \xi), \xi) d\xi. \quad (15)$$

Expression (15) for the tensor kernel $\mathbf{K}$ includes only the parameters of the undisturbed process; that is, it depends only on the kinematics of deformation of the homogeneous medium. This kernel can be explicitly written for different simple types of deformation such as extension and compression, source and sink flows, and pure shears and their combinations.

If the material function $\lambda(\mathbf{x_0})$ is not identically equal to a constant, then the right-hand side of Eq. (12) contains the vector $\mathbf{X_0^1}$, so that system C_{N+3}^1 cannot be divided into subsystems D_N^1 and (13). Thus, in the case of a weak inhomogeneity in the wide sense, the formulation of the problem in terms of disturbances becomes interconnected and thereby more complicated.

Of interest is the degree of deviation of the particle trajectories in a weakly inhomogeneous medium from the corresponding trajectories in the homogeneous medium. The first approximation in α for this deviation is described by the vector $\mathbf{X_0^1}$ (14). For each $\mathbf{x_0} \in \bar{\Omega}_0$, we denote

$$\begin{aligned} \Xi^0(\mathbf{x_0}) &= \sup_{t>0} \left\| \mathbf{X^0}(\mathbf{x_0}, t) \right\|, \\ \Xi^1(\mathbf{x_0}) &= \sup_{t>0} \left\| \mathbf{X^1}(\mathbf{x_0}, t) \right\|, \end{aligned} \quad (16)$$

$$\begin{aligned} \omega_0^0 &= \{\mathbf{x_0} \in \bar{\Omega}_0 : \Xi^0(\mathbf{x_0}) = \infty\}, \\ \omega_0^1 &= \{\mathbf{x_0} \in \bar{\Omega}_0 : \Xi^1(\mathbf{x_0}) = \infty\}, \end{aligned} \quad (17)$$

where $\|\cdot\|$ is a certain norm in the vector space.

Let us classify three cases of a disturbed motion.

1°. $\omega_0^1 = \varnothing$; that is, there exists a constant $\Xi_*^1 < \infty$ such that

$$\sup_{\mathbf{x_0} \in \bar{\Omega}_0} \Xi^1(\mathbf{x_0}) < \Xi_*^1. \quad (18)$$

Then, the initial weak inhomogeneity of order α yields the deviation of the trajectories of all particles by quantities of the same order α or higher.

2°. $\omega_0^1 \neq \varnothing$ but, for any particle $\mathbf{x_0} \in \omega_0^1$, the following inequality holds:

$$\sup_{t>0} \frac{\left\| \mathbf{X^1}(\mathbf{x_0}, t) \right\|}{\left\| \mathbf{X^0}(\mathbf{x_0}, t) \right\|} < \infty. \quad (19)$$

3°. $\omega_0^1 \neq \varnothing$ and there exist particles $\mathbf{x_0}$ that do not satisfy inequality (19).

The first two cases correspond to the stability of the process of deformation of a homogeneous medium under a small perturbation of the inhomogeneity parameter. In the third case, the deviation of the particle trajectories under such perturbation has a finite measure and the asymptotic approach used in this study is adequate only on a finite time interval $0 < t < T$, where T can be up to order $\frac{1}{\alpha}$ (temporal boundary layer). The instability of motion under a small perturbation of the inhomogeneity can be treated as the onset of mixing of a weakly inhomogeneous continuum.

3. The trajectory approach described above was developed in [4] for weakly inhomogeneous viscous flows and in [5] for the deformation of weakly inhomogeneous viscoplastic solids; the latter study contains general statements of the problems in the first approximation in α and solutions to some of these problems. Let us present the results of the solution of the plane problem of spreading of a weakly inhomogeneous (in the wide sense) incompressible ideally plastic tube under the action of pressures applied to its inner and outer surfaces.

The only material function present in the constitutive relations for an ideally plastic material satisfying the von Mises–Hencky plasticity criterion is the yield limit $\sigma_s(\mathbf{x}, t)$, for which Eq. (2) can be rewritten as follows:

$$\sigma_s(\mathbf{x}, t) = \sigma_s(\mathbf{x_0}, 0) \equiv \Sigma(\mathbf{x_0}). \quad (20)$$

Introduce a polar coordinate system (r, θ) fitted to the center of the tube cross-section. We assume that the initial distribution of function $\Sigma(\mathbf{x_0})$ is slightly different from the radial distribution

$$\Sigma(r_0, \theta_0) = \Sigma^0(r_0) + \alpha \Sigma^1(r_0, \theta_0) + \ldots \quad (21)$$

In the region $a^0(t) < r < b^0(t)$, the solution corresponding to the plane inertialess spreading of an ideally plastic tube, which is inhomogeneous only in the radial

direction, with a yield limit $\Sigma^0(r_0)$ at $t = 0$ takes the form [7]

$$v_r^0 = \frac{c}{r}, \quad v_\theta^0 \equiv 0,$$

$$s_{rr}^0 = -\frac{1}{\sqrt{2}}\Sigma^0\left(\sqrt{r^2 - 2ct}\right), \quad s_{r\theta}^0 \equiv 0, \tag{22}$$

$$p^0 = p_a - \frac{1}{\sqrt{2}}\Sigma^0\left(\sqrt{r^2 - 2ct}\right) - \sqrt{2}\int_{a^0(t)}^{r}\Sigma^0\left(\sqrt{\xi^2 - 2ct}\right)\frac{d\xi}{\xi},$$

where v_r^0 and v_θ^0 are the components of the velocity vector, s_{rr}^0 and $s_{r\theta}^0$ are the components of the stress deviator, p^0 is the pressure, p_a and p_b are the pressures specified on the tube surfaces ($p_a > p_b$), and $c > 0$ is an arbitrary constant.

The condition of full plasticity has the form:

$$p_a - p_b = \sqrt{2}\int_{a^0(t)}^{b^0(t)}\Sigma^0\left(\sqrt{\xi^2 - 2ct}\right)\frac{d\xi}{\xi} \equiv \sqrt{2}\int_{a(0)}^{b(0)}\frac{\eta\Sigma^0(\eta)d\eta}{\eta^2 + 2ct}. \tag{23}$$

In the case of a homogeneous plastic material with the yield limit σ_s, this condition implies the well-known relation between the pressure drop and the tube geometry at each time instant [7]

$$p_a - p_b = \sqrt{2}\sigma_s \ln\frac{b(t)}{a(t)}. \tag{24}$$

In Eqs. (22) and (23), the law of motion of Lagrangian particles along the rays

$$r(r_0, \theta_0, t) = \sqrt{r_0^2 + 2ct} \equiv R^0(r_0, t), \quad \theta(r_0, \theta_0, t) = \theta_0, \tag{25}$$

and the inverse law of motion

$$r_0(r, \theta, t) = \sqrt{r^2 - 2ct} \equiv R_0^0(r, t), \quad \theta_0(r, \theta, t) = \theta \tag{26}$$

are used.

We note that the distribution of the yield limit $\Sigma^0(r_0)$ can be arbitrary and, in particular, discontinuous, which corresponds to the spreading of a plastic composite tube [1].

Similarly to Eqs. (8) and (9), we present the laws of motion for a weakly inhomogeneous flow in the form

$$r(r_0, \theta_0, t) = R^0(r_0, t) + \alpha R^1(r_0, \theta_0, t) + \ldots, \quad \theta(r_0, \theta_0, t) = \theta_0 + \alpha\Theta^1(r_0, \theta_0, t) + \ldots; \tag{27}$$

$$r_0(r, \theta, t) = R_0^0(r, t) + \alpha R_0^1(r, \theta, t) + \ldots, \quad \theta_0(r, \theta, t) = \theta + \alpha\Theta_0^1(r, \theta, t) + \ldots \tag{28}$$

The linearized system C_7^1 of seven equations in seven unknown disturbances with superscript 1 is as follows:

$$-p_{,r}^1 + \frac{1}{r^2}(r^2 s_{rr}^1)_{,r} + \frac{s_{r\theta,\theta}^1}{r} = 0, \quad -p_{,\theta}^1 - s_{rr,\theta}^1 + \frac{1}{r}(r^2 s_{r\theta}^1)_{,r} = 0; \tag{29}$$

$$v_{r,r}^1 + \frac{v_r^1}{r} + \frac{v_{\theta,\theta}}{r} = 0; \tag{30}$$

$$2s_{rr}^0 s_{rr}^1 = \Sigma^0(R_0^0)\left[\Sigma^1(R_0^0, \theta) + \frac{\partial\Sigma_0}{\partial r_0}(R_0^0)R_0^1(r, \theta, t)\right]; \tag{31}$$

$$s_{r\theta}^1 = \frac{\Sigma^0(R_0^0)}{v_u^0}v_{r\theta}^1; \tag{32}$$

$$\frac{dR^1}{dt} = v_r^1(R^0, \theta_0, t) + \frac{\partial v_r^0}{\partial r}(R^0)R^1(t), \quad R^1(0) = 0, \quad \frac{d\Theta^1}{dt} = \frac{1}{R^0}v_\theta^1(R^0, \theta_0, t), \quad \Theta^1(0) = 0. \tag{33}$$

For the sake of brevity, in Eqs. (31) and (32), the arguments r and t of R_0^0 are omitted.

We also write two boundary conditions on each surface of the tube carried over to the undisturbed circles $r = a^0(t)$ and $r = b^0(t)$:

$$-p^1 + s_{rr}^1 = \left(\frac{\partial p^0}{\partial r} - \frac{\partial s_{rr}^0}{\partial r}\right)b^1, \tag{34}$$

$$s_{r\theta}^1 = (-p^0 - s_{rr}^0 + p_b)\frac{1}{b^0}\frac{\partial b^1}{\partial\theta}. \tag{35}$$

Now, we pass to the analysis of system (29)–(33) with boundary conditions (34) and (35). Algebraic

equation (31) and formulas (22) immediately imply an expression for the component s_{rr}^1:

$$s_{rr}^1 = -\frac{1}{\sqrt{2}}\left[\Sigma^1(R_0^0(r,t),\theta) + \frac{\partial\Sigma^0}{\partial r_0}(R_0^0(r,t))R_0^1(r,\theta,t)\right] \quad (36)$$

We will seek the disturbance of the velocity field v_r^1, v_θ^1 in the form of a Fourier series in angle θ

$$v_r^1 = \frac{1}{r}\sum_{m=0}^{\infty} c_m\cos m\theta, \quad v_\theta = v_\theta^1(r),$$

$$v_{rr}^1 = -\frac{1}{r^2}\sum_{m=0}^{\infty} c_m\cos m\theta, \quad (37)$$

$$v_{r\theta}^1 = \frac{1}{2}\left(v_\theta^{1'} - \frac{1}{r^2}\sum_{m=0}^{\infty} mc_m\sin m\theta\right),$$

where v_θ is an unknown function and c_m = const. Thus, the incompressibility condition (30) is automatically satisfied.

After the expressions for v_r^0 (22) and v_r^1 (37) are substituted into the first equation of (33), the latter can be rewritten in the form

$$\frac{dR^1}{dt} + \frac{cR^1}{r_0^2 + 2ct} = \frac{\sum_{m=0}^{\infty} c_m\cos m\theta_0}{\sqrt{r_0^2 + 2ct}}, \quad R^1(0) = 0. \quad (38)$$

The exact solution to the Cauchy problem (38)

$$R^1(r_0,\theta_0,t) = \frac{t\sum_{m=0}^{\infty} c_m\cos m\theta_0}{\sqrt{r_0^2 + 2ct}} \equiv \frac{t\sum_{m=0}^{\infty} c_m\cos m\theta_0}{R^0(r_0,t)} \quad (39)$$

enables us to easily determine R_0^1:

$$R_0^1(r,\theta,t) = -\frac{t\sum_{m=0}^{\infty} c_m\cos m\theta}{\sqrt{r^2 - 2ct}} \equiv -\frac{t\sum_{m=0}^{\infty} c_m\cos m\theta}{R_0^0(r,t)}. \quad (40)$$

Expression (40) can be substituted into Eq. (36) with the result that the component s_{rr}^1 becomes a known function of the Eulerian coordinates r and θ and time t for any given distribution of the yield limit Σ^1.

Then, Eqs. (37) and (32) imply that

$$s_{r\theta}^1 = \frac{\Sigma^0}{2v_u^0}\left(v_\theta^{1'} - \frac{1}{r^2}\sum_{m=0}^{\infty} mc_m\sin m\theta\right). \quad (41)$$

With account for Eq. (41), the first equilibrium equation (29) gives

$$p_{,r} = s_{rr,r}^1 + \frac{2s_{rr}^1}{r} - \frac{\Sigma^0}{2v_u^0 r^3}\sum_{m=0}^{\infty} m^2c_m\cos m\theta, \quad (42)$$

the right-hand side of Eq. (42) being known. Integrating Eq. (42) with respect to r with the boundary condition (34), where we substitute

$$b^1 = \frac{t}{b^0}\sum_{m=0}^{\infty} c_m\cos m\theta, \quad (43)$$

we arrive at an expression for the pressure disturbance

$$p^1 = s_{rr}^1 - 2\int_r^{b^0} s_{rr}^1(\xi,\theta,t)\frac{d\xi}{\xi} + \frac{1}{2\sqrt{2}c}\sum_{m=0}^{\infty} m^2c_m\cos m\theta\int_r^{b^0}\Sigma^0\left(\sqrt{\xi^2 - 2ct}\right)\frac{d\xi}{\xi} + \frac{\sqrt{2}t}{b^{0^2}}\Sigma^0(b_0)\sum_{m=0}^{\infty} c_m\cos m\theta. \quad (44)$$

Substituting $r = a^0(t)$ into Eq. (44), we obtain

$$\frac{p_a - p_b}{4c}\sum_{m=0}^{\infty} m^2c_m\cos m\theta - 2\int_{a^0}^{b^0} s_{rr}^1(\xi,\theta,t)\frac{d\xi}{\xi} = \sqrt{2}t\left(\frac{\Sigma^0(a_0)}{a^{0^2}} - \frac{\Sigma^0(b_0)}{b^{0^2}}\right)\sum_{m=0}^{\infty} c_m\cos m\theta. \quad (45)$$

This is the condition of realizability of a plastic flow with kinematics (37), which is analogous to Eq. (23) for a radial motion. Analyzing the dependence of both sides of Eq. (45) on θ and expanding Σ^1 in a Fourier series in the same set $\cos m\theta$ with coefficients d_m, we can express d_m in terms of c_m.

The last unknown stress component $s_{r\theta}^1$ is determined by integrating the second equation (42) with

respect to r with the boundary condition (35). Then, $v_\theta^1(r)$ is found from Eq. (41) and the function $\Theta^1(r_0, \theta_0, t)$, from the second equation (33).

ACKNOWLEDGMENTS

This work was supported by the Russian Foundation for Basic Research (projects nos. 05-01-00397 and 05-01-00401).

REFERENCES

1. B. E. Pobedrya, *Mechanics of Composition Materials* (Mosk. Gos. Univ., Moscow, 1984) [in Russian].
2. A. A. Il'yushin, *Mechanics of Continuum Media* (Mosk. Gos. Univ., Moscow, 1990) [in Russian].
3. D. V. Georgievskiĭ and D. M. Klimov, Izv. Akad. Nauk, Mekh. Zhidk. Gaza, No. 2, 56 (2000).
4. D. V. Georgievskiĭ, D. M. Klimov, and A. G. Petrov, Vestn. Mosk. Gos. Univ., Ser. 1: Mat., Mekh., No. 2, 37 (2002).
5. D. V. Georgievskiĭ, D. M. Klimov, and A. G. Petrov, Izv. Akad. Nauk, Mekh. Zhidk. Gaza, No. 3, 17 (2003).
6. A. G. Petrov, Dokl. Akad. Nauk **382** (1), 15 (2002) [Dokl. Phys. **47**, 742 (2002)].
7. A. A. Il'yushin, V. A. Lomakin, and A. P. Shmakov, *Problems and Exercises on Mechanics of Continuum Media* (Mosk. Gos. Univ., Moscow, 1979) [in Russian].

Translated by M. Lebedev

Doklady Physics, Vol. 50, No. 12, 2005, pp. 650–654. Translated from Doklady Akademii Nauk, Vol. 405, No. 4, 2005, pp. 484–488.

MECHANICS

On the Optimal Shapes of Bodies Moving in Dense Media

G. Ye. Yakunina

Presented by Academician S.S. Grigoryan February 10, 2005

Received March 9, 2005

Within the framework of the model of local interaction between a moving body and a medium and under the assumption that the tangential stress on the body surface is described by the mixed model of friction, the shapes of the bodies that have a given area of base and afford, for a rectilinear motion in the medium, a minimum to the resistance or a maximum to the length of the trajectory of an inertial motion are found. The parameters of the optimal body shape are related with the medium characteristics and the body velocity.

STATEMENT OF THE PROBLEM

Consider a rectilinear inertial motion of a body in a medium opposite to vector **x**. Neglecting the gravity, write the equation of motion for a body of mass m and the medium resistance force D in the form

$$m\frac{dU}{dt} = -D, \quad D = \iint_S [\sigma_n(\mathbf{n}\cdot\mathbf{x}) + \sigma_\tau(\boldsymbol{\tau}\cdot\mathbf{x})]dS. \quad (1)$$

Here, t is time, U is the motion velocity, σ_n and σ_τ are the normal and tangential stresses exerted on a body surface element, **n** and τ are the unit vectors of inward normal and tangent to the surface element (vector $\boldsymbol{\tau}$ is directed in the line of the particles' slide over the surface), and the integration is taken over the surface S of contact between the body and the medium.

We consider the interaction between the medium and surface S within the framework of the model of local interaction (MLI) and write σ_n as the sum of the dynamic and strength terms:

$$\sigma_n = A_1U^2\alpha^2 + B_1, \quad \alpha = (\mathbf{n}\cdot\mathbf{x}). \quad (2)$$

In (2), positive constants A_1 and B_1 are parameters of the model determined by the characteristics of the medium. Under certain assumptions, expression (2) describes σ_n on the surface of a body that moves in a gas or in dense media such as soil, concrete, or metal.

We write σ_τ with the use of the mixed model of friction, which is suggested in paper [1] and that generalizes both the Coulomb model of friction and the model of constant friction:

$$\sigma_\tau = \begin{cases} \mu_0\sigma_n, & \text{if} \quad \mu_0\sigma_n \le \tau_S, \\ \tau_S, & \text{if} \quad \mu_0\sigma_n > \tau_S. \end{cases} \quad (3)$$

Here, μ_0 is a constant coefficient and τ_S is the shear yield point of the medium. As a result, σ_τ is described, similar to σ_n, by the two-term formula

$$\sigma_\tau = A_2U^2\alpha^2 + B_2. \quad (4)$$

Moreover, according to (2) and (3), if

$$\alpha \le \alpha_k, \quad \alpha_k = \alpha_k(\lambda) = \sqrt{\left(\frac{C}{\mu_0} - 1\right)\frac{1}{\lambda}},$$
$$\lambda = \lambda(U) = \frac{A_1U^2}{B_1}, \quad C = \frac{\tau_S}{B_1}, \quad (5)$$

then σ_τ is calculated by the Coulomb model of friction and

$$A_2 = \mu_0A_1, \quad B_2 = \mu_0B_1. \quad (6)$$

Otherwise, σ_τ involves the model of constant friction and

$$A_2 = 0, \quad B_2 = \tau_S. \quad (7)$$

Within the framework of MLI, vector $\boldsymbol{\tau}$ is assumed to be coplanar to vectors **U** and **n** and surface S is defined by the condition

$$0 \le \alpha \le 1.$$

Suppose that, at the initial time instant, $U = U_0$. Taking into account (1)–(7), we write the resistance $D =$

Baranov Central Institute of Aviation Motors, ul. Aviamotornaya 2, Moscow, 111116 Russia
State University of Management, Ryazanskiĭ pr. 99, Moscow, 109542 Russia
e-mail: galina_yakunina@mail.ru

1028-3358/05/5012-0650$26.00

$D_0 = D(U_0)$ of the body and the total length H_0 of its trajectory in the form

$$D_0 = B_1 \iint_S f(\alpha)\alpha\, dS, \quad f(\alpha) = \lambda_0 g_1(\alpha) + g_2(\alpha), \quad (8)$$

$$H_0 = \frac{m}{2A_1}\int_0^{\lambda_0} \frac{d\lambda}{\lambda D_1 + D_2}, \quad D_i = \iint_S g_i(\alpha)\alpha\, dS, \quad (9)$$

$$i = 1, 2,$$

$$g_1(\alpha) = \alpha^2\left(1 + \frac{\nu B\gamma}{\alpha}\right), \quad g_2(\alpha) = 1 + \frac{B\gamma}{\alpha},$$

$$B = \frac{B_2}{B_1}.$$

Here, $\lambda_0 = \lambda(U_0)$, $\gamma = (\boldsymbol{\tau}\cdot\mathbf{x}) = \sqrt{1-\alpha^2}$, and the friction parameters B and ν depend on α and α_k:

$$B = \mu_0, \quad \nu = 1, \quad \text{if} \quad \alpha \le \alpha_k, \quad (10)$$

$$B = C, \quad \nu = 0, \quad \text{if} \quad \alpha > \alpha_k. \quad (11)$$

Model (2)–(7) represents a particular case of writing the stresses in the framework of MLI. Given the characteristics of the medium and velocity U_0, it makes it possible to represent D_0 and H_0 in the form of functionals of the shape of surface S. This makes it possible to apply methods of variational calculus when determining the shapes of the bodies that afford the minimum $D^* = \min(D_0)$ or the maximum $H^* = \max(H_0)$.

For the generalized MLI, it has been demonstrated [2] that, velocity U_0 being fixed, in the class of three-dimensional configurations, for a flow without separation past a body with a given area of base S_b, the minimum D^* is attained on the bodies such that the condition

$$\alpha = \alpha^* = \text{const} \quad (12)$$

is satisfied at each point of the body surface.

In [2], methods for constructing three-dimensional configurations satisfying condition (12) have been developed. These methods are based on blending the patches of the surfaces of the optimal cone with half-angle $\beta^* = \arcsin\alpha^*$ and the tangent planes. It has been shown that, for a specified S_b and under given constraints on the length and lateral dimensions of the body, one can construct infinitely many three-dimensional bodies having the same resistance D^*; they have been called absolutely optimal bodies (AOB).

Below, in the framework of model (2)–(7), by known characteristics of the medium and given values of U_0 and S_b, we find the α^* that determines, according to (2) and (12), the optimal angle of incidence between the flow of the medium and the normal to the element of the AOB surface. It is demonstrated that the maximum H^* of the trajectory length is attained on the bodies that also satisfy condition (12), but, in the general case, they are not the bodies of the minimal resistance and their value of α^* is different.

OPTIMAL SHAPES OF THE BODIES

For an AOB, value α^* in (12) is the value of α at which the positive function $f(\alpha)$ present in (8) has the minimum on the segment [0, 1]. The values of B and ν for functions $g_i(\alpha)$, i = 1,2, present in (8) are calculated in accordance with (10) and (11) at $\alpha_k = \alpha_k(\lambda_0)$ and function $f(\alpha)$ is seen to be continuous and independent of S_b. Hence, the minimum of $f(\alpha)$ and value α^* are determined only by velocity U_0 and parameters of model (2)–(7).

If values D_i, i = 1, 2, in expression (9) are independent of λ, which is the case for constant B and ν, then one can integrate expression (9) and write H_0 in the form

$$H_0 = \frac{m}{2A_1D_1}\ln\left(1 + \frac{\lambda_0 D_1}{D_2}\right).$$

This expression may be used when σ_τ presented in (4) is calculated by the Coulomb model of friction (6) or by the model of constant friction (7) and parameters A_2 and B_2 in (4) are constant. It has been shown [3] that, parameters A_i and B_i, i = 1, 2, being constant, in the class of three-dimensional configurations, for a flow without separation and for given U_0, S_b, and m, the maximum H^* is attained on the bodies such that condition (12) is satisfied at each point of their surface. This means that, in this case, the shapes of the bodies with the longest trajectory have the same structure as AOB; however, they have a different α^*, which is the value of $\alpha \in [0, 1]$ that affords a maximum to the function

$$h_0(\alpha) = \frac{\ln(1+q)}{q\left(1 + \frac{B\gamma}{\alpha}\right)}, \quad q = \lambda_0\alpha^2\frac{\alpha + \nu B\gamma}{\alpha + B\gamma}. \quad (13)$$

Here, constants B and ν are determined by expressions (10) or (11) for the models of friction (6) and (7), respectively.

For the mixed model of friction, according to (5), (10), and (11), values B, ν, and D_i, i = 1, 2, depend on λ and, for an arbitrary shape of the body, expression (9) for H_0 cannot be integrated. Nevertheless, this does not preclude the use of the methods of variational calculus when searching for the extremum of H_0 and, following

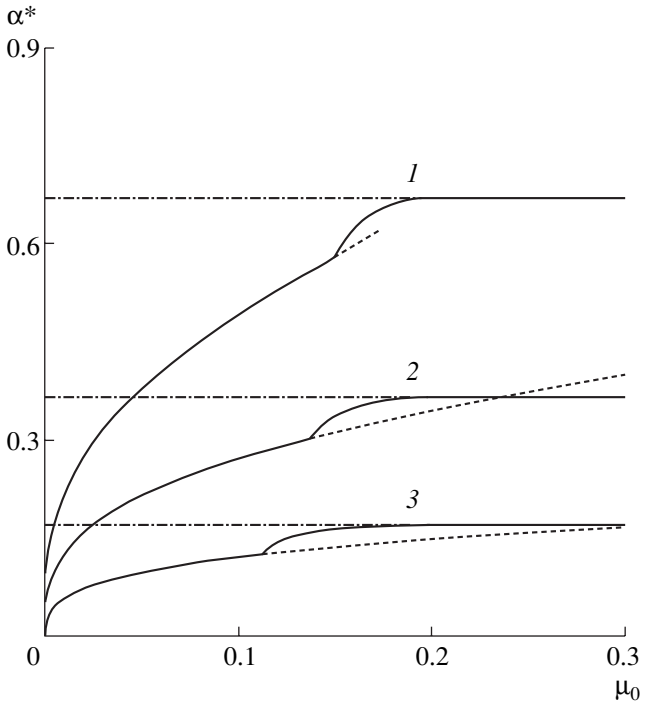

Fig. 1. The μ_0-dependence of the values α^* for the bodies with the longest trajectory in the case $C = 0.2$ given for $\lambda_0 =$ 1, 5, and 50 by curves *1*, *2*, and *3*, respectively. The solid lines correspond to the mixed model of friction, the dashed lines, to the Coulomb model of friction, and the dot-and-dash lines, to the model of constant friction.

the technique employed in [3], one can show that, in this case, again, the bodies that afford the maximum H^* are constructed under condition (12) just as AOBs are, and their α^* is the value of $\alpha \in [0, 1]$ at which the function

$$h(\alpha) = \frac{h_1(\alpha) + h_2(\alpha)}{\lambda_0 \alpha^2}, \tag{14}$$

$$h_1(\alpha) = \frac{\ln(\lambda_1 \alpha^2 + 1)}{1 + \dfrac{\mu_0 \gamma}{\alpha}}, \quad h_2(\alpha) = \ln \frac{\lambda_0 \alpha^2 + \dfrac{C\gamma}{\alpha} + 1}{\lambda_1 \alpha^2 + \dfrac{C\gamma}{\alpha} + 1}$$

attains its maximum. Here, λ_1 depends on α and λ_0. However, for $C < \mu_0$, the second condition in (3) is always true and σ_τ is calculated throughout by model (7). In this case, $\lambda_1 = 0$, $h_1(\alpha) = 0$, and function $h(\alpha) = h_0(\alpha)$ with B and ν given in (11). When $C \geq \mu_0$, if $\frac{1}{\alpha^2}\left(\frac{C}{\mu_0} - 1\right) < \lambda_0$, then $\lambda_1 = \frac{1}{\alpha^2}\left(\frac{C}{\mu_0} - 1\right)$; otherwise, $\lambda_1 = \lambda_0$. In the latter case, condition (5) is always valid, σ_τ is calculated by the Coulomb model (6), $h_2(\alpha) = 0$, and function $h(\alpha) = h_0(\alpha)$ with B and ν defined in (10). This case is realized, in particular, for $\lambda_0 \leq \frac{C}{\mu_0} - 1$.

Thus, there is a domain of values of C, μ_0, and λ_0 such that $h(\alpha) = h_0(\alpha)$ and, hence, in this domain, $h(\alpha)$ and $h_0(\alpha)$ have the same α^*. Curves *1*, *2*, and *3* in Fig. 1 show the μ_0-dependence of values α^* for function $h(\alpha)$ when $C = 0.2$ and $\lambda_0 = 1$, 5, and 50, respectively. The values of α^* obtained for $h_0(\alpha)$ by models (6) and (7) for the same C, λ_0, and μ_0, are shown in Fig. 1 by dashed and dot-and-dash lines, respectively. It can be seen that, for small μ_0, the values of α^* calculated for $h(\alpha)$ coincide with those obtained for $h_0(\alpha)$ with B and ν defined in (10) and, when $\mu_0 \geq C$, these values coincide with α^* obtained for $h_0(\alpha)$ with B and ν defined in (11).

We search for the minimum of $f(\alpha)$ and maximum of $h(\alpha)$ among their local and boundary extrema. The local extrema are attained at $\alpha = \alpha_m$ and satisfy the equations $f'(\alpha) = 0$ or $h'(\alpha) = 0$. The boundary minimum of $f(\alpha)$ and maximum of $h(\alpha)$ may occur at $\alpha = 1$. Hence, the values of α^* for $f(\alpha)$ and $h(\alpha)$ are such that

$$f(\alpha^*) = \min(f(\alpha_m), f(1)), \quad f(1) = 1 + \lambda_0,$$

$$h(\alpha^*) = \max(h(\alpha_m), h(1)), \quad h(1) = \frac{\ln(1 + \lambda_0)}{\lambda_0}.$$

Write the equations for $f(\alpha)$ and $h_0(\alpha)$ at $\alpha = \alpha_m$ in the form

$$2\lambda_0 \alpha^3 \gamma + \nu B \lambda_0 \alpha^2 (\gamma^2 - \alpha^2) - QB = 0. \tag{15}$$

Here, we take $Q = 1$ when searching for the minimums of $f(\alpha)$ and

$$Q = \frac{q^2}{(q+1)\ln(q+1) - q} \tag{16}$$

for the maximums of $h_0(\alpha)$. It can be shown that, when $\frac{\lambda_0 \alpha^2}{3} \ll 1$, the value Q in (16) is close to a constant: $Q \approx 2$. Then, in the slender-body approximation, assuming that

$$\alpha^2 \ll 1, \tag{17}$$

one can write solutions to Eq. (15) in the form

$$\alpha = \alpha_m, \quad \alpha_m = \left(\frac{QB}{2\lambda_0}\right)^{1/3}, \tag{18}$$

where $Q = 1$ for the minimums of $f(\alpha)$ and $Q = 2$ for the maximums of $h_0(\alpha)$.

It can be demonstrated that, for a fixed λ_0 and small B, the values $\alpha^* = \alpha_m$. However, according to (18), the values α_m grow with increasing B. In this case, the values $f(\alpha_m)$ increase and the values $h_0(\alpha_m)$ decrease. The growth of $f(\alpha_m)$ when $\alpha^* = \alpha_m$ is bounded by the value $f(1)$ attained at $B = B^*$ and $\alpha_m = \alpha_m^* : f(\alpha_m^*) = f(1)$. Taking into account formulas (8) and (15), one can write the following expressions for B^* and α_m^*:

$$B^* = \frac{\lambda_0}{2\sqrt{1+\lambda_0\nu}}, \quad \alpha_m^* = \frac{1}{\sqrt{2+\lambda_0\nu}}.$$

Figure 2 shows B^* related to λ_0 for the bodies of the minimal resistance (curves *1* and *2* constructed for models (6) and (7), respectively) and for the bodies with the longest trajectory (curves *3* and *4* constructed for models (6) and (7), respectively). For the function $h_0(\alpha)$, the values of B^* and α_m^* such that $h_0(\alpha_m^*) = h_0(1)$ are obtained with the use of (13) and (15). One can see that, for $h_0(\alpha)$, as well as for $f(\alpha)$, $\alpha_m^* \le \frac{1}{\sqrt{2}}$. The value $\alpha_m \le \alpha_m^* \le \frac{1}{\sqrt{2}}$ and since, for $B < B^*$, the value $\alpha^* = \alpha_m$, in this case, we always have $\beta^* < 45°$. If $B \ge B^*$, then $\alpha^* = 1$, $\beta^* = 90°$, and the optimal body is the cylinder with the end face of a given area. As far as, for most media, $B \le 0.3$, it can be shown that the latter case is realized for comparatively slow motions, when the shape of the body exerts little influence on the resistance and the length of its trajectory.

It was demonstrated above that there are values of C, μ_0, and λ_0 such that $h(\alpha) = h_0(\alpha)$ and, hence, for these values, the local maximums of $h(\alpha)$, as well as of $h_0(\alpha)$, are attained in approximation (17) at $\alpha = \alpha_m$ (see (18)). Figure 1 shows the values $\alpha^* = \alpha_m$ related to μ_0 for $C = 0.2$. One can see that, parameters C and λ_0 being fixed, there is a range of values of μ_0 such that $h(\alpha)$ and $h_0(\alpha)$ have different α^*. However, in this range, the values of α^* for $h(\alpha)$ may be approximated by the values of α^* for function $h_0(\alpha)$ with B and ν defined in (11).

It can easily be shown that, for the mixed model of friction, functions $f(\alpha)$ and $h(\alpha)$ have at most two local extrema and, since, for $B < B^*$, the values $\alpha^* = \alpha_m$, in this case, α^* is determined in approximation (17) by the relations

$$\alpha^* = \begin{cases} \alpha_1 & \text{for} \quad \lambda_0 \le \lambda_k, \\ \alpha_2 & \text{for} \quad \lambda_0 > \lambda_k, \end{cases} \tag{19}$$

$$\alpha_1 = \left(\frac{Q\mu_0}{2\lambda_0}\right)^{1/3}, \quad \alpha_2 = \left(\frac{QC}{2\lambda_0}\right)^{1/3}.$$

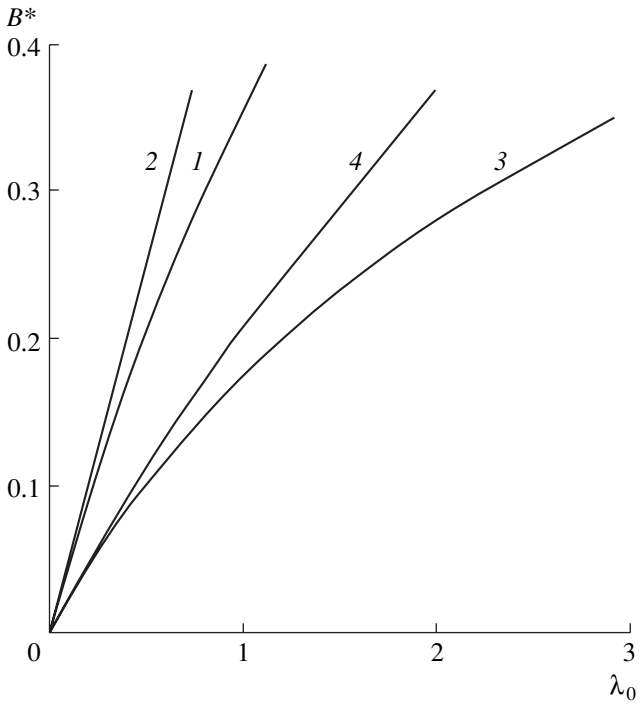

Fig. 2. Limiting values of the friction parameter B^* related to λ_0 for the bodies of the minimal resistance (curves *1* and *2*) and for the bodies with the longest trajectory (curves *3* and *4*) constructed for the Coulomb model of friction (curves *1* and *3*) and for the model of constant friction (curves *2* and *4*).

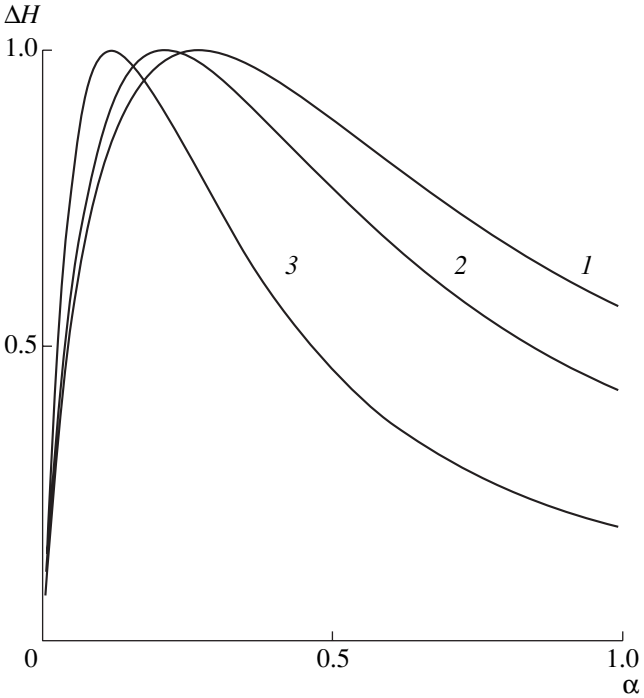

Fig. 3. The α-dependence of the values of $\Delta H = \frac{H_0(\alpha)}{H^*}$ presented for the mixed model of friction in the case $C = 0.2$ and $\mu_0 = 0.1$ by curves *1*, *2*, and *3* constructed for $\lambda_0 = 5$, 10, and 50, respectively.

Here, we take

$$Q = 1, \quad \lambda_k = \frac{27}{2\mu_0^2}\left(\left(\frac{C}{\mu_0}\right)^{2/3} - 1\right)^3 \qquad (20)$$

for the bodies of the minimal resistance and

$$Q = 2, \quad \lambda_k = \frac{1}{\mu_0^2}\left(\frac{C}{\mu_0} - 1\right)^3 \qquad (21)$$

for the bodies with the longest trajectory.

One can demonstrate that, for $\lambda_0 \in [3, 50]$ and $B \le 0.3$, approximation (19)–(21) allows constructing bodies such that D_0 and H_0 differ from D^* and H^* by less than 3%. Such λ_0 and B correspond to the cases of the motion in soil, concrete, and metal, when the shape of the body exerts an essential influence on its motion characteristics and the optimal bodies exhibit significant advantages over other bodies in terms of resistance and trajectory length. For instance, curves *1*, *2*, and *3* in Fig. 3 show the α-dependence of the values $\Delta H = \frac{H_0(\alpha)}{H^*}$ for $\lambda_0 = 5$, 10, and 50, respectively, when $C = 0.2$ and $\mu_0 = 0.1$. Here, $H_0(\alpha)$ is the length of the trajectory of the cones with half-angle $\beta = \arcsin\alpha$ having the same initial velocity, mass, and area of base as the optimal body. For $\alpha > 0.3$, the advantages of the optimal bodies are seen to grow with increasing α and λ_0 and, for $\lambda_0 = 50$, the trajectory of the optimal body is almost five times longer than that of the cylinder having $\alpha = 1$ on the front face.

CONCLUSIONS

Within the framework of model (2)–(7), the shapes of the bodies that have a given area of base and afford, for a rectilinear motion in a medium, a minimum to the resistance or a maximum to the length of the trajectory of an inertial motion have been found. For a flow without separation, the angle of incidence between the flow of the medium and the normal to the element of the surface of the optimal body has been shown to be constant throughout the body surface. In approximation (17), formulas (19)–(21) relate this angle with the characteristics of the medium and the velocity of the body. Note that, within the framework of model (2)–(7), condition (12) holds on the surface of the optimal bodies. Therefore, these bodies may be constructed with the use of the methods developed earlier [2] for constructing AOBs, which allows constructing optimal three-dimensional bodies of various configurations.

ACKNOWLEDGMENTS

This work was supported by the Russian Foundation for Basic Research (project no. 04-01-00771).

REFERENCES

1. S. S. Grigoryan, Dokl. Akad. Nauk SSSR **244** (4), 846 (1979) [Sov. Phys. Dokl. **24** (2), 110 (1979)].
2. G. Ye. Yakunina, Prikl. Mat. Mekh. **64**, 605 (2000).
3. G. Ye. Yakunina, Dokl. Akad. Nauk **376** (6), 768 (2001) [Dokl. Phys. **46** (2), 140 (2001)].

Translated by A. Pankrat'ev

Doklady Physics, Vol. 50, No. 12, 2005, pp. 655–662. Translated from Doklady Akademii Nauk, Vol. 405, No. 5, 2005, pp. 618–624.

MECHANICS

Calculation of the Parameters of a Turbulent Boundary Layer with Suction Using Data for an Impermeable Plate

I. I. Vigdorovich

Presented by Academician G.G. Chernyĭ June 22, 2005

Received June 27, 2005

A theory based on the asymptotic analysis of Reynolds-averaged Navier–Stokes equations and dimensional analysis is proposed for obtaining a complete solution to the problem of the turbulent boundary layer on a plate with uniform suction without involving any special closure hypotheses. The profiles of velocity and shear stress, the friction distribution over the wall, and the integral characteristics in the entire possible region of the parameters are calculated using only the velocity profile known for an impermeable plate. The results are presented in the scaling variables.

1. We consider the flow of an incompressible fluid in the turbulent boundary layer on a flat smooth plate streamed by a uniform flow with the velocity U_e constant along the plate length at the outer boundary of the layer and constant suction velocity v_w directed along the normal to the surface. We assume that the turbulent flow is developed directly from the leading edge of the plate. We assume that the level of turbulent pulsations in the free stream is negligibly small and does not affect the flow in the boundary layer.

All mean quantities including the gradient of the longitudinal velocity, turbulent shear stress, and the boundary-layer thickness Δ are functions of the Cartesian coordinates x and y and determining parameters of the problem

$$\frac{\partial u}{\partial y} = F_1(x, y, \nu, v_w, U_e),$$
$$\langle u'v' \rangle = F_2(x, y, \nu, v_w, U_e), \quad \Delta = F_3(x, \nu, v_w, U_e). \tag{1}$$

Here, ν is the kinematic viscosity coefficient and the origin of the Cartesian coordinate system is on the leading edge of the plate. The quantity Δ that is a certain transverse scale of the flow in the boundary layer will be defined below.

Central Institute of Aviation Motors,
ul. Aviamotornaya 2, Moscow, 111116 Russia
e-mail: ivigdorovich@ciam.ru

The substitution of x and U_e expressed from the first and third of Eqs. (1) into the second of Eqs. (1) yields

$$\langle u'v' \rangle = F_4\left(y, \nu, v_w, \Delta, \frac{\partial u}{\partial y}\right).$$

Applying dimensional considerations to this relation, we obtain

$$\langle u'v' \rangle = -\left(y\frac{\partial u}{\partial y}\right)^2 S(R_l, \beta, \eta), \quad R_l = \frac{y^2}{\nu}\frac{\partial u}{\partial y},$$
$$\beta = \frac{v_w}{R_l y \partial u/\partial y}, \quad \eta = \frac{y}{\Delta}. \tag{2}$$

The function S, as well as the functions $F_1, \ldots, F_4$, is universal for the class of flows under consideration that depend on the three parameters ν, v_w, and U_e. We assume that the function S is continuous for $0 \le R_l \le \infty$, $-\infty \le \beta \le 0$, and $0 \le \eta < \infty$ and is differentiable with in this region, which physically corresponds to usual assumptions according to which viscosity is significant only in a thin near-wall region (viscous sublayer), where the outer scale (boundary layer thickness) does not affect the flow. In addition, we assume that $S(\infty, 0, 0) \neq 0$. As was shown in [1], this is the existence condition for the logarithmic velocity profile in the boundary layer over the impermeable plate.

The flow under consideration is described by the boundary layer equations with zero pressure gradient under the corresponding boundary conditions on the wall. Taking into account closure relation (2), we arrive at the boundary value problem for the mean velocity field. Below, we will give the asymptotic solution of this boundary value problem for large Reynolds numbers.

In the boundary layer equation that is written for the stream function of the mean flow ψ, we change to new variables by the formulas [2]

$$\psi = U_e \Delta \Psi(\xi, \eta), \quad \Lambda(\xi) = \frac{dR_\Delta}{dR_x}, \quad \xi = \ln R_\Delta,$$
$$R_x = \frac{U_e x}{\nu}, \quad R_\Delta = \frac{U_e \Delta}{\nu}.$$

1028-3358/05/5012-0655$26.00

In addition to the dimensionless stream function $\Psi(\xi, \eta)$, we introduce the second unknown function $\Lambda(\xi)$, which has the physical meaning of the rate of the longitudinal variation of the transverse scale Δ. For $\Psi(\xi, \eta)$ and $\Lambda(\xi)$, we obtain the equation [2]

$$\begin{aligned}\Lambda[\Psi_\eta\Psi_{\xi\eta} - \Psi_{\eta\eta}(\Psi + \Psi_\xi)] \\ = [(\eta\Psi_{\eta\eta})^2 S(R_l, \beta, \eta) + e^{-\xi}\Psi_{\eta\eta}]_\eta,\end{aligned} \quad (3)$$

where

$$R_l = e^\xi \eta^2 \Psi_{\eta\eta}, \quad \beta = B(\eta R_l \Psi_{\eta\eta})^{-1};$$

$$\xi > -\infty, \quad \eta = 0: \quad \Psi_\eta = 0, \quad \Lambda(\Psi + \Psi_\xi) = -B; \quad (4)$$

$$\eta \longrightarrow \infty: \quad \Psi_\eta \longrightarrow 1, \quad \eta\Psi_{\eta\eta}\sqrt{S(R_l, \beta, \eta)} \longrightarrow 0. \quad (5)$$

Here, $B = \dfrac{v_w}{U_e}$ is the suction factor. Relations (4) and (5) specify the conditions on the plate and the outer boundary of the boundary layer, respectively. Two conditions (for the velocity and shear stress) are imposed at the outer boundary taking into account the order of the differential equation.

We seek the asymptotic representation of the solution of the problem given by Eqs. (3)–(5) for $\xi \longrightarrow \infty$. Let us introduce the small parameter ε and new independent variable $\zeta = \varepsilon\xi$ such that $\dfrac{1}{\zeta} = O(1)$. Thus, the small parameter ε is the reciprocal of the logarithm of the Reynolds number calculated in terms of the characteristic transverse scale of the flow.

The suction velocity on the wall is specified as

$$B = \varepsilon^2 b, \quad b = O(1), \quad (6)$$

i.e., we assume that the transverse velocity at the wall is a small quantity of the second order in ε.

2. In the transverse direction, it is necessary to consider two characteristic regions: outer and near-wall regions of the boundary layer. The flow in the near-wall region was studied in [1, 3]. In particular, it was shown that, for arbitrary suction, the profiles of the velocity and shear stress can be evaluated using only the velocity profile in the boundary layer on an impermeable plate.

In what follows, we consider only the outer region of the boundary layer, where $\dfrac{1}{\eta} = O(1)$. According to [4, 5], two characteristic regions along the flow are generally formed in the boundary layer with suction. In the initial section of the plate, the moderate suction regime is realized such that the shear stress at the wall is of the same order as that in the outer region. At a constant suction velocity and increasing Reynolds number, the moderate suction region is followed by the strong-suction region, where the shear stress at the wall is much larger than the value in the outer region. The solution obtained in [4] for the moderate-suction case has a singularity at $\zeta = 2\kappa(-b)^{-1/2}$, which corresponds to vanishing of the leading term of the expansion of the function $\Lambda(\xi)$.

Then, we consider the vicinity of this singular point, where strong suction occurs. We change to the new variable $s = O(1)$ by the formula [5]

$$s = \varepsilon^{-1}[\zeta - 2\kappa(-b)^{-1/2}] - 2k\ln\varepsilon - k\ln(-b), \quad (7)$$

where k is a constant to be determined.

For moderate suction, the function $\Lambda(\xi)$ is on the order of ε and, as was mentioned above, vanishes in the leading term at the singular point [4]. For this reason, the solution in the strong-suction case is sought in the form [5]

$$\Lambda(\xi) = -\varepsilon^2 b\lambda(s) + O(\varepsilon^3), \quad (8)$$

$$\Psi(\xi, \eta) = \Psi_w(\xi) + \eta - \varepsilon^2 b g(s, \eta) + O(\varepsilon^3). \quad (9)$$

Here, $\Psi_w(\xi)$ is the stream function on the wall and, therefore, $g(s, 0) = 0$. In view of Eqs. (6) and (8), from the second of conditions (4) on the wall, we obtain

$$\Psi_w(\xi) + \frac{d\Psi_w(\xi)}{d\xi} = \frac{1}{\lambda(s)} + O(\varepsilon). \quad (10)$$

Substituting expansions (8)–(10) into Eq. (3), taking into account Eq. (7), and performing the passage to the limit as $\varepsilon \longrightarrow 0$ such that $s = O(1)$ and $\dfrac{1}{\eta} = O(1)$, we arrive at the following partial differential equation for the functions $g(s, \eta)$ and $\lambda(s)$:

$$[(\eta g_{\eta\eta})^2 S]_\eta + (1 + \eta\lambda)g_{\eta\eta} = \lambda g_{s\eta}, \quad (11)$$

where

$$g(s, 0) = g_\eta(s, \infty) = 0, \quad \lim_{\eta\to\infty} \eta g_{\eta\eta}\sqrt{S} = 0$$

and $S = S(\infty, 0, \eta)$.

The case of moderate suction corresponds to the following passage to limit in Eq. (11):

$$s \longrightarrow -\infty, \quad \lambda(s) \longrightarrow \infty, \quad g(s, \eta) \longrightarrow \lambda(s) f(\eta), \quad (12)$$

where the function $f(\eta)$ satisfies the following boundary value problem for the ordinary differential equation:

$$[(\eta f'')^2 S]' + \eta f'' = 0, \quad f(0) = f'(\infty) = 0, \quad \lim_{\eta \to \infty} \eta f'' \sqrt{S} = 0. \tag{13}$$

The solution of boundary value problem (13) has the form

$$f'(\eta) = -\int_\eta^\infty \frac{\Phi d\eta}{2\eta\sqrt{S}}, \quad \Phi(\eta) = \int_\eta^\infty \frac{d\eta}{\sqrt{S}}. \tag{14}$$

The function $f'(\eta)$ specifies the velocity profile in the boundary layer on the impermeable plate [2]. According to Eq. (14), its asymptotic expression at the wall has the form

$$f'(\eta) = \frac{F_1}{\kappa}(\ln\eta + A_0 - \ln F_1) + O(\eta^\alpha), \quad \eta \longrightarrow 0, \tag{15}$$

where

$$\alpha > 0, \quad F_1 \equiv \sqrt{-f(\infty)} = \frac{\Phi(0)}{2},$$

and A_0 is a constant.

Another limiting case, $\lambda = 0$, corresponds to the asymptotic suction boundary layer with suction, i.e., a one-dimensional flow, where all mean quantities depend only on the distance from the wall [6]. Such a flow on the plate is achieved in a far downstream region of the flow. Setting $\lambda = 0$ in Eq. (11), we find that the function g satisfies the ordinary differential equation

$$[(\eta g'')^2 S]' + g'' = 0; \quad g(0) = g'(\infty) = 0, \quad \lim_{\eta \to \infty} \eta g'' \sqrt{S} = 0 \tag{16}$$

and can be represented in the form

$$g' = -\frac{h^2}{4}, \quad h(\eta) = \int_\eta^\infty \frac{d\eta}{\eta\sqrt{S}}. \tag{17}$$

Here, the function $h(\eta)$ has the following logarithmic asymptotic behavior on the wall:

$$h(\eta) = -\frac{1}{\kappa}(\ln\eta + A_\infty - \ln F_1) + O(\eta^\alpha), \quad \eta \longrightarrow 0, \quad \alpha > 0, \tag{18}$$

where A_∞ is a constant.

Thus, the solutions of Eq. (11) describe the entire family of velocity profiles in the turbulent boundary layer with suction, including the limiting cases of the impermeable plate and asymptotic boundary layer.

Then, we consider the function $\gamma(s, \eta)$ related to $g(s, \eta)$ as

$$g_\eta = -\frac{\gamma^2}{4} - \gamma\sqrt{G}, \tag{19}$$

where

$$G(s) = -\lambda(s)\left[g(s, \infty) + \frac{d}{ds}g(s, \infty)\right]. \tag{20}$$

From Eq. (11), the asymptotic expression for $\gamma(s, \eta)$ on the wall is found in the form

$$\gamma(s, \eta) = -\frac{1}{\kappa}[\ln\eta + A(s) - \ln F_1] + O(\eta^\alpha), \quad \eta \to 0, \quad \alpha > 0, \tag{21}$$

where $A(s)$ is a certain function.

3. The skin-friction coefficient is sought in the form [5]

$$\frac{c_f}{2} = -\varepsilon^2 b + \varepsilon^4 b^2 t(s) + O(\varepsilon^5). \tag{22}$$

As was shown in [5], the asymptotic matching of the solutions for the outer and near-wall regions with the use of asymptotic representation (21) provides $k = -\frac{1}{2}$ and two equalities

$$A(s) - \ln F_1 - 2\kappa\sqrt{G(s)} = s + C_0, \tag{23}$$

where $C_0 = 2.05$ is the additive constant in the logarithmic law for the velocity profile near an impermeable wall [1], and

$$t(s) = G(s). \tag{24}$$

Relation (23) makes it possible to close the boundary value problem given by Eqs. (11) for two desired functions $g(s, \eta)$ and $\lambda(s)$. Relation (24), together with Eq. (20), is the representation of skin-friction in terms of the solution of this boundary value problem.

To solve the boundary value problem specified by Eqs. (11) with additional condition (23), it is necessary to know only the function $S(\infty, 0, \eta)$. In view of Eq. (13), this function is unambiguously related to $f'(\eta)$ and can be expressed in quadratures in terms of the latter function as

$$S = \frac{f - f(\infty) - \eta f'}{(\eta f'')^2}.$$

Since the function $f'(\eta)$ specifies the velocity profile in the boundary layer on the impermeable plate, it is well known from experimental data. To calculate this function, we use the Coles empirical formula [7]

$$\frac{f'(\eta)}{F_1} = \frac{1}{\kappa}[\ln\eta - 0.55(1+\cos(\pi\eta))],$$
$$0 < \eta \le 1, \quad F_1 = \frac{1.55}{\kappa}.$$

Here, Δ is the distance from the wall at which the longitudinal component of the mean velocity differs from U_e by 0.5%. It is the general definition of the transverse scale Δ.

Solving Eq. (19) as a quadratic equation with respect to γ and taking into account Eq. (24), we obtain

$$\frac{2(U_e-u)}{U_e\left(\sqrt{\frac{1}{2}c_f+B}+\sqrt{\frac{1}{2}c_f+\frac{Bu}{U_e}}\right)} = \gamma(q,\eta)+O(\sqrt{c_f}),$$
$$q \equiv \frac{B}{\sqrt{\frac{1}{2}c_f+B}} = -\frac{1}{\sqrt{t}}+O(\sqrt{-B}), \quad -\infty \le q \le 0. \tag{25}$$

Relation (25) shows that velocity profiles in the boundary layer with suction beyond the viscous sublayer can be described by the family of curves depending on one parameter q. For $q = 0$, scaling rule (25) expresses the well-known velocity defect law for an impermeable plate. According to Eqs. (12), (20), and (24), $\gamma(0, \eta) = -\frac{f'(\eta)}{F_1}$. Another limiting case $q = -\infty$ corresponds to the asymptotic boundary layer when $\gamma(-\infty, \eta) = h(\eta)$.

To represent the results, it is convenient to use the transverse scale

$$\Delta_* = \int_0^\infty \frac{2(U_e-u)}{U_e\left(\sqrt{\frac{1}{2}c_f+B}+\sqrt{\frac{1}{2}c_f+\frac{Bu}{U_e}}\right)}dy.$$

For a particular case of an impermeable plate, this quantity is equal to $\delta^*\left(\sqrt{\frac{1}{2}c_f}\right)^{-1}$ and is the boundary layer thickness introduced by Clauser [8].

Turbulent shear stress also satisfies the one-parameter scaling law. The substitution of Eq. (19) into Eq. (2) yields

$$\frac{\sqrt{-\langle u'v'\rangle}}{U_e\left(\sqrt{\frac{1}{2}c_f+B}-B\right)}$$
$$= \frac{\eta\gamma_\eta(q,\eta)}{1-q}\left(\frac{q\gamma(q,\eta)}{2}-1\right)\sqrt{S(\infty,0,\eta)}+O(\sqrt{c_f}),$$

where

$$-\infty \le q \le 0.$$

This relation should also be satisfied everywhere beyond the viscous sublayer.

In [5, 9], a universal friction law was found, which can be represented as

$$\ln Z^*_{\begin{Bmatrix}\delta^*\\ x\end{Bmatrix}} = \Phi_{\begin{Bmatrix}1\\2\end{Bmatrix}}(q)+O(\sqrt{c_f}), \tag{26}$$

$$Z^*_{\begin{Bmatrix}\delta^*\\ x\end{Bmatrix}} \equiv \sqrt{\frac{1}{2}c_f}(-B)^{\mp 1}\exp\left(\frac{2\kappa\sqrt{\frac{1}{2}c_f}}{B}\right)R_{\begin{Bmatrix}\delta^*\\ x\end{Bmatrix}},$$

where

$$\Phi_1 = -g(s,\infty)e^s, \quad \Phi_2 = \int_{-\infty}^{s}\frac{e^s}{\lambda(s)}ds$$

and R_{δ^*} is the Reynolds number based on the displacement thickness. According to Eq. (26), the friction distributions over the plate for various suction velocities and various Reynolds numbers can be described by one universal curve in scaling variables.

4. In Eq. (11), we make the substitution

$$g_\eta = \lambda f' - \frac{h^2}{4} + \varphi_\eta \tag{27}$$

and change the variable s to the independent variable $\tau = \frac{1}{\lambda}$. A pair of functions $\varphi(\tau, \eta)$ and

$$\Omega(\tau) = -\frac{d\lambda}{ds} = \frac{d\tau}{\tau^2 ds} \tag{28}$$

satisfies the boundary value problem

$$(\Phi+\tau h)(\eta\sqrt{S}\varphi_{\eta\eta})_\eta + \tau[(\eta\sqrt{S}\varphi_{\eta\eta})^2]_\eta$$
$$= \Omega(\tau^2\varphi_{\tau\eta}-f'), \tag{29}$$

$$\varphi(\tau,0) = \varphi_\eta(\tau,\infty) = 0, \quad \lim_{\eta\to\infty}\eta\sqrt{S}\varphi_{\eta\eta} = 0, \tag{30}$$

$$s(\tau) = A(\tau) - \ln F_1 - C_0 - 2\kappa\sqrt{t(\tau)},$$
$$0 \le \tau < \infty, \tag{31}$$

$$t(\tau) = \frac{F_1^2}{\tau^2}+\frac{F_1 D}{\kappa\tau}-\frac{F_1^2\Omega(\tau)}{\tau}-\frac{\varphi(\tau,\infty)}{\tau}$$
$$-\tau\Omega(\tau)\frac{d\varphi(\tau,\infty)}{d\tau}, \tag{32}$$

where

$$D = A_0 - A_\infty.$$

Expression (32) is Eq. (20) rewritten with regard to Eq. (27).

The asymptotic expression for the desired functions for small τ values has the form

$$\Omega(\tau) = \frac{1}{2\kappa F_1} + O(\tau^2), \quad \varphi(\tau, \eta) = \varphi_0(\eta) + O(\tau), \quad (33)$$

where φ_0, according to Eq. (29), satisfies the linear ordinary differential equation

$$\Phi(\eta\sqrt{S}\varphi_0'')' + \frac{f'}{2\kappa F_1} = 0. \quad (34)$$

This equation has the following solution satisfying conditions (30) in the free stream:

$$\varphi_0' = \frac{hN_1 - N_2}{2\kappa}, \quad (35)$$

where

$$N_1 = -\int_\eta^\infty \frac{f'd\eta}{F_1\Phi}, \quad N_2 = -\int_\eta^\infty \frac{hf'd\eta}{F_1\Phi}.$$

Asymptotic expression (33) enables one to obtain the expansion of the function γ for a regime close to the moderate-suction regime:

$$\gamma(q, \eta) = -\frac{f'(\eta)}{F_1} + q\gamma_1(\eta) + O(q^2), \quad q \longrightarrow -0, \quad (36)$$

where

$$\gamma_1 = \frac{f'^2}{4F_1^2} - \frac{h^2}{4} + \frac{[N_1(0) - D]f'}{2\kappa F_1} + \frac{hN_1 - N_2}{2\kappa}.$$

According to the last expression,

$$\gamma_1(0) = \frac{2DN_1(0) - D^2}{4\kappa^2} - \frac{N_2(0)}{2\kappa}.$$

Thus, the first term of expansion (36) has the logarithmic asymptotic behavior and the next terms have no singularities on the wall.

The expansion of the functions Φ_1 and Φ_2 given by Eqs. (26) has the form

$$\Phi_1(q) = \frac{2\kappa}{q} - \ln(-q) + A_0 - C_0 + b_1 q + O(q^2),$$

$$\Phi_2(q) = \frac{2\kappa}{q} + \ln(-q) + A_0 - C_0 + \left(b_1 + \frac{1}{\kappa}\right)q + O(q^2),$$

$$q \longrightarrow -0,$$

$$b_1 = \kappa\gamma_1(0) + \frac{N_1(0) - D - 1}{2\kappa}.$$

5. To analyze the other limiting case $\lambda \longrightarrow 0$, i.e., the flow regime close to the asymptotic boundary layer, in Eq. (11) we make the substitution

$$g_\eta = -\frac{h^2}{4} + \lambda\psi_\eta \quad (37)$$

and change s to the independent variable λ. A pair of functions $\psi(\lambda, \eta)$ and

$$\Omega_1(\lambda) = -\frac{d\lambda}{ds} = \Omega(\lambda^{-1}) \quad (38)$$

satisfies the boundary value problem

$$h(\eta\sqrt{S}\psi_{\eta\eta})_\eta + \lambda[(\eta\sqrt{S}\psi_{\eta\eta})^2]_\eta + \lambda\eta\psi_{\eta\eta} + \Omega_1(\lambda\psi_{\lambda\eta} + \psi_\eta) + \frac{h}{2\sqrt{S}} = 0, \quad (39)$$

$$\psi(\lambda, 0) = \psi_\eta(\lambda, \infty) = 0, \quad \lim_{\eta\to\infty} \eta\sqrt{S}\psi_{\eta\eta} = 0, \quad (40)$$

$$s(\lambda) = A(\lambda) - \ln F_1 - C_0 - 2\kappa\sqrt{t(\lambda)}, \quad 0 \le \lambda < \infty,$$

$$t(\lambda) = \frac{F_1 D}{\kappa}\lambda + \lambda\psi(\lambda, \infty)[\Omega_1(\lambda) - \lambda] + \lambda^2\Omega_1(\lambda)\frac{d\psi(\lambda, \infty)}{d\lambda}. \quad (41)$$

According to Eq. (39), the function $\psi_0(\eta) \equiv \psi(0, \eta)$ satisfies the ordinary differential equation

$$h(\eta\sqrt{S}\psi_0'')' + \frac{\omega\psi_0'}{F_1} + \frac{h}{2\sqrt{S}} = 0, \quad \omega = F_1\Omega_1(0),$$
$$\psi_0(0) = \psi_0'(\infty) = 0, \quad \lim_{\eta\to\infty} \eta\sqrt{S}\psi_0'' = 0, \quad (42)$$

whose solution near the wall can be represented in the form

$$\psi_0' = F_1 Z_1(\omega)h + Z_2(\omega) + O(\eta^\alpha), \quad \eta \longrightarrow 0, \quad \alpha > 0. \quad (43)$$

Here, $Z_1(\omega)$ and $Z_2(\omega)$ are certain functions. Therefore, ψ_0' has the logarithmic asymptotic behavior on the wall.

Solving Eq. (19) as a quadratic equation with respect to γ and taking into account Eq. (37), we obtain

$$\gamma = \sqrt{h^2 - 4\lambda\psi_\eta + 4t} - 2\sqrt{t}.$$

Taking into account asymptotic representations (18), (21), and (43), from this expression we obtain

$$A = A_\infty + 2\kappa F_1 \lambda Z_1(\omega) + 2\kappa\sqrt{t} + O(\lambda^2), \quad \lambda \longrightarrow 0. \quad (44)$$

Substituting this expression into closure condition (41), differentiating the resulting equality with respect to the variable λ, and taking into account Eq. (38), we arrive at the following equation for the parameter ω:

$$2\kappa\omega Z_1(\omega) + 1 = 0. \quad (45)$$

Thus, the eigenvalue problem given by Eqs. (42) and (45) is obtained for determining the leading terms of the asymptotic representation of the desired functions. The numerical solution of Eq. (42) shows that Eq. (45) has an infinite number of roots on the positive semiaxis and has no root on the negative semiaxis. The smallest root is equal to $\omega = 1.423$.

Thus, the desired asymptotic representation cannot be unambiguously determined by analyzing the solution of the boundary value problem given by Eqs. (39)–(41) for a parabolic equation near $\lambda = 0$. The ω value will be finally chosen due to the numerical solution of the problem with the initial conditions at $\lambda = \infty$.

The asymptotic representation of the functions Φ_1 and Φ_2 has the form

$$\Phi_1 = D_1 + \ln\frac{D}{\kappa} - \frac{\kappa}{\omega D q^2} + O(q^{-4}),$$
$$e^{\Phi_2} = \frac{2e^{D_1}}{\omega}\ln(-q) + O(1), \quad D_1 = A_\infty - C_0, \quad (46)$$
$$q \longrightarrow -\infty.$$

Excluding the parameter q from Eq. (46) and taking into account Eq. (26), we obtain the displacement thickness as a function of the longitudinal coordinate:

$$Z^*_{\delta^*} = \frac{D}{\kappa}e^{D_1} - \frac{1}{\omega}\exp(D_1 - \omega e^{D_1} Z^*_x) + \ldots, \quad Z^*_x \longrightarrow \infty.$$

The resulting expressions show that the asymptotic boundary layer regime is achieved only in the limit $R_x \longrightarrow \infty$ rather than at a finite distance from the leading edge. In this case, the quantity $\frac{1}{2}c_f + B$ and difference between the current and limiting values of the displacement thickness tend to zero exponentially.

6. For numerical calculations, two formulations of the boundary value problem are used. The problem given by Eqs. (29)–(31) is first solved in the interval $0 \le \tau \le a$ ($0.8 \le a \le 1.5$) and the problem given by Eqs. (39)–(41) is then solved in the interval $0 < \lambda < \frac{1}{a}$.

We represent Eq. (29) in the form

$$(\eta\sqrt{S}\varphi_{\eta\eta})_\eta = G_1,$$
$$G_1(\tau, \eta) = \frac{\Omega(\tau^2\varphi_{\tau\eta} - f')}{\Phi + \tau h + 2\tau\eta\sqrt{S}\varphi_{\eta\eta}} \quad (47)$$

and solve Eq. (47) as the second order equation with the known right-hand side. Taking into account conditions (36) on the outer boundary of the layer, we arrive at the integro-differential equation

$$\varphi_\eta(\tau, \eta) = \int_\eta^\infty [h(\eta) - h(\eta_1)] G_1(\tau, \eta_1) d\eta_1.$$

For the desired function to have no singularity on the wall, we make the change $\varphi_\eta = hy$. As a result, we obtain the following equation for $y(\tau, \eta)$:

$$y(\tau, \eta) = \int_\eta^\infty \left[1 - \frac{h(\eta_1)}{h(\eta)}\right] G_2(\tau, \eta_1) d\eta_1, \quad (48)$$

where

$$G_2(\tau, \eta) = \frac{\Omega(\tau^2 h y_\tau - f')}{\Phi + \tau h + 2\tau\eta\sqrt{S}h y_\eta - 2\tau y}.$$

From Eq. (31), there follows the closure condition

$$\Omega(\tau) = \left[2\kappa F_1 + 2\kappa\tau^2\frac{dy(\tau, 0)}{d\tau}\right]^{-1}. \quad (49)$$

The system of Eqs. (48) and (49) for two functions $y(\tau, \eta)$ and $\Omega(\tau)$ is numerically solved by the iteration method. With a given function $\Omega(\tau)$ [$\Omega(\tau) \equiv \Omega(0)$] at the first step of iterations, in order to determine $y(\tau, \eta)$ from Eq. (48) in each layer in the variable τ, the integral is changed to the sum according to the Gregory formula (modified trapezoid formula, which is exact for the third order polynomials), which allows for the calculation of the desired function by an explicit formula sequentially for all η values. In order to approximate the partial derivative with respect to τ, the function values in the current and preceding layers in τ are used. After the determination of $y(\tau, \eta)$, new $\Omega(\tau)$ values are calculated from Eq. (49) using numerical differentia-

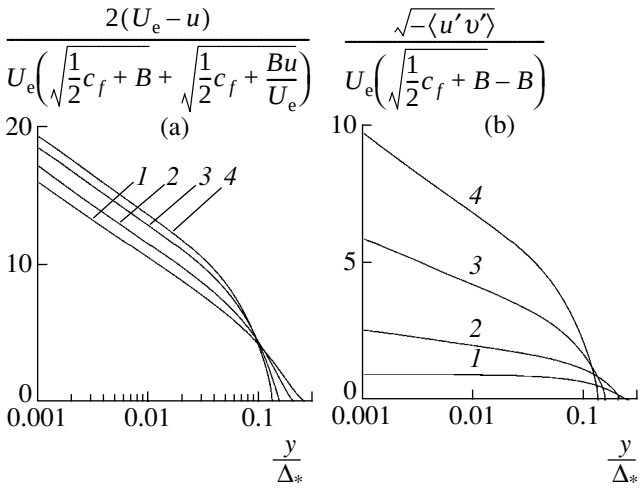

Fig. 1. Profiles calculated for (a) velocity and (b) turbulent shear stress in the boundary layer for q = (*1*) 0, (*2*) –0.25, (*3*) –1.5, and (*4*) –∞.

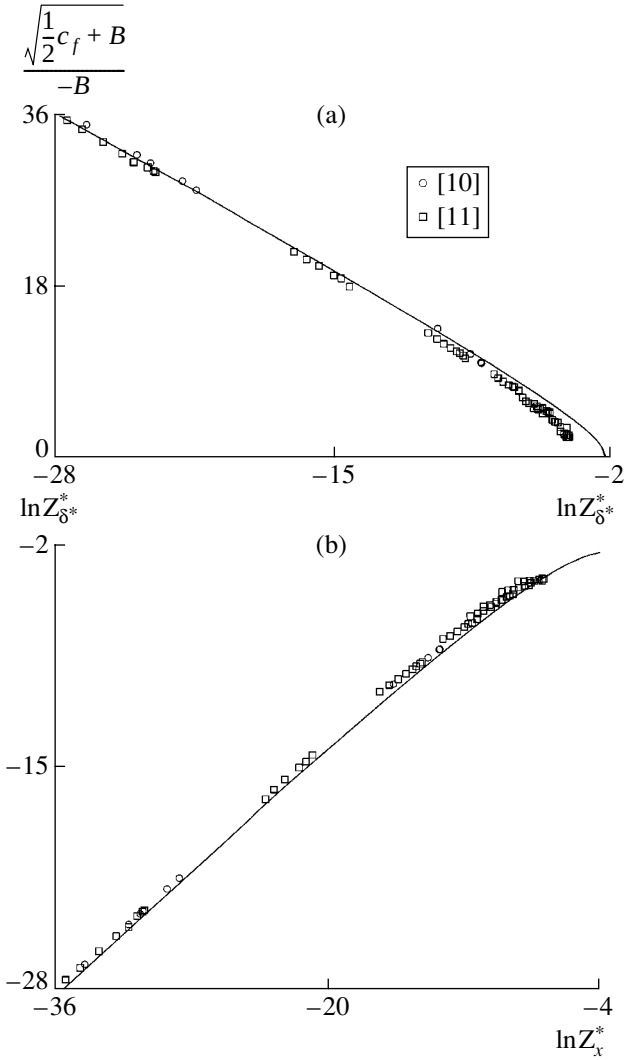

Fig. 2. Theoretical distributions of (a) friction and (b) displacement thickness over the plate in the scaling variables along with the experimental data taken from (○) [10] and (□) [11].

tion with smoothing. The calculation shows that the function $\Omega(\tau)$ is almost constant in the interval $0 \le \tau \le a$ and the iteration procedure can be completed after the third step.

The boundary value problem specified by Eqs. (39)–(41) is solved similarly. After the representation in the form

$$(\eta\sqrt{S}\psi_{\eta\eta})_\eta = -H_1 - \frac{1}{2\sqrt{S}},$$

$$H_1(\lambda, \eta) = \frac{\Omega_1(\lambda\psi_{\lambda\eta} + \psi_\eta)}{h + 2\lambda\eta\sqrt{S}\psi_{\eta\eta}}$$

Eq. (39) is reduced to the integro-differential equation

$$\psi_\eta(\tau, \lambda) = \int_\eta^\infty [h(\eta_1) - h(\eta)]H_1(\lambda, \eta_1)d\eta_1 + f'(\eta).$$

The calculated limiting value of the function $F_1\Omega_1(0)$ coincides with the smallest root of Eq. (45). Thus, the function $-\frac{F_1 d\lambda}{ds}$ is almost constant in the entire range of λ and increases monotonically from $\frac{1}{2\kappa}$ = 1.220 corresponding to $\lambda = \infty$ to 1.423 corresponding to $\lambda = 0$.

Figure 1 shows the calculated profiles for (a) the velocity and (b) shear stress for various values of the scaling parameter q. Figure 2a shows a universal curve specifying the friction distribution over the plate with suction along with the measurement data [10, 11] plotted in the scaling variables given by Eqs. (26). Experiments reported in [10, 11] were carried out in a rather wide region of the parameters: $3.8 \le R_x \times 10^{-5} \le 35$ and $1 \le -B \times 10^3 \le 3.6$. On the whole, the agreement of the theoretical dependence with the measurements is satisfactory. Discrepancy is observed only for large values of the scaling variable $Z^*_{\delta*}$ corresponding to the strong-suction regime. In Fig. 2b, the calculated curve is compared with the data reported in [10, 11] for the displacement thickness distribution. All experimental points plotted in the scaling variables given by Eqs. (26) lie near the theoretical curve.

ACKNOWLEDGMENTS

This work was supported by the Council of the President of the Russian Federation for Support of Young

Scientists and Leading Scientific Schools (project no. NSh-1635.2003.1 for G.G. Chernyĭ's school).

REFERENCES

1. I. I. Vigdorovich, Dokl. Akad. Nauk **392** (3), 340 (2003) [Dokl. Phys. **48**, 528 (2003)].
2. I. I. Vigdorovich, Izv. Akad. Nauk, Mekh. Zhidk. Gaza, No. 4, 106 (1993).
3. I. I. Vigdorovich, Zh. Éksp. Teor. Fiz. **126** (5), 1180 (2004) [JETP **99**, 1028 (2004)].
4. I. I. Vigdorovich, Dokl. Akad. Nauk **331** (4), 443 (1993) [Phys. Dokl. **38**, 335 (1993)].
5. I. I. Vigdorovich, Dokl. Akad. Nauk **356** (1), 42 (1997) [Phys. Dokl. **42**, 506 (1997)].
6. I. I. Vigdorovich, Dokl. Akad. Nauk **396** (1), 47 (2004) [Dokl. Phys. **49**, 303 (2004)].
7. D. Coles, J. Fluid Mech. **1**, 191 (1956).
8. F. H. Clauser, Adv. Appl. Mech. **4**, 1 (1956).
9. I. I. Vigdorovich, Izv. Akad. Nauk, Mekh. Zhidk. Gaza, No. 4, 76 (1999).
10. R. L. Simpson, R. J. Moffat, and W. M. Kays, Int. J. Heat Mass Transf. **12** (7), 771 (1969).
11. K. Depooter, PhD Thesis (Univ. Waterloo, Waterloo, Canada, 1973).

Translated by R. Tyapaev

Doklady Physics, Vol. 50, No. 12, 2005, pp. 663–667. Translated from Doklady Akademii Nauk, Vol. 405, No. 5, 2005, pp. 625–629.

MECHANICS

General Forms of Representation of the Solutions to the Stokes Equations and a Method for the Calculation of Viscous Fluid Flows

O. V. Voinov

Presented by Academician G.G. Chernyi July 4, 2005

Received July 11, 2005

In this paper, we study general solutions to the Stokes equations in hydrodynamics and equations of equilibrium in the elasticity theory, obtain new forms for the representation of general solutions, and construct a numerical method for calculating the Stokes flows of a viscous fluid. By the representation of the solutions to the Stokes equations we mean the expression of these solutions in terms of harmonic functions. The new formulas include the representation in terms of the first order operator and a class of 27 representations. The symmetries of fluid flows with low rates and of elastic media equilibria have been found.

The suggested numerical method involves the above-mentioned representations and a boundary integral equation of a particular type. It is essentially different from the known methods of boundary integral equations based on multipole solutions to the Stokes equations [1–3].

The manner in which the solutions to the Stokes equations and to the equations of the elasticity theory are related to the solutions to the Laplace equations is considered in detail in [4] for the case of plane problems.

REPRESENTATION OF THE VELOCITIES IN TERMS OF THE FIRST ORDER DIFFERENTIAL OPERATOR

The solutions to the Stokes equation

$$\nabla_i p = \mu\Delta u_i, \quad \nabla_j u_j = 0, \quad i, j = 1, 2, 3, \tag{1}$$

are known to be the same as the solutions to the displacement equations of equilibrium in the elasticity theory

$$(1-2\sigma)\Delta u_i + \nabla_i \mathrm{div}\mathbf{u} = 0 \tag{2}$$

at the Poisson coefficient $\sigma = \frac{1}{2}$. Here, summation is taken over repeated subscripts.

It is known that the general solution to the three-dimensional Stokes equations (1) can be represented [5] in terms of the second order differential operator. The representation of the solutions to Eqs. (2) in terms of the second order operator is also known [6].

By contrast, we represent the solution to the Stokes equations in terms of the first order differential operator:

$$u_i = \Gamma_{ij}\varphi_j, \quad \Gamma_{ij} = (2\delta_{ik}x_j + \delta_{ji}x_k - \delta_{kj}x_i)\nabla_k,$$
$$\Delta\varphi_i = 0, \quad p = 2\mu\nabla_j\varphi_j, \tag{3}$$

where δ_{ik} is the Kronecker delta. To solve Eqs. (2), we replace coefficient 2 in representation (3) with $\frac{4(1-\sigma)}{3-4\sigma}$. By analogy with the velocity potential $\mathbf{u} = \nabla\Phi$ of a vortex-free flow of an ideal liquid, we call the harmonic functions in (3) the generalized potentials.

For an arbitrary axisymmetric flow, according to (3), the velocity field may be specified via two harmonic functions φ and Q in the form

$$u_r = 2x_2\nabla_r\varphi - r\nabla_2\varphi + \nabla_r Q,$$
$$u_2 = r\nabla_r\varphi + 2x_2\nabla_2\varphi + \nabla_2 Q, \tag{4}$$
$$\Delta Q = 0, \quad p = 2\mu\nabla_2\varphi, \quad r = \sqrt{x_1^2 + x_3^2}.$$

Consider the Poiseuille flow through a channel with a unit circular cross-section at the unit average velocity

$$u_r = 0, \quad u_2 = 2 - 2r^2, \quad p = -8\mu x_2.$$

The Poiseuille flow is associated with two generalized potentials

$$\varphi = r^2 - 2x_2^2, \quad Q = \frac{8}{3}x_2^3 - 4r^2x_2 + 2x_2. \tag{5}$$

The Oberbeck formula [7, 8] for the solution to the problem of motion of an ellipsoid in a viscous fluid

Institute of Theoretical and Applied Mechanics, Tyumen Branch, Siberian Division, Russian Academy of Sciences, ul. Taĭmyrskaya 74, Tyumen, 625000 Russia
e-mail: o.v.voinov@mtu-net.ru

1028-3358/05/5012-0663$26.00

involving two arbitrary harmonic functions implies, with one of them being neglected and the indices being circularly permuted, the representation of the solutions to the Stokes equations

$$u_i = x_j\nabla_i\varphi_j - (3-4\sigma)\varphi_i, \quad p = 2\mu\nabla_j\varphi_j. \tag{6}$$

Note that formulas (6) and (3) are qualitatively different, because representation (6) involves the functions themselves along with their derivatives.

A formula for the general solutions to Eq. (2), which is similar to (6), has been obtained in works by P.F. Papkovich, H. Neuber, and G.D. Grodskiĭ (see [9, 10]); their formula includes an additional potential vector.

THE CLASS OF GENERAL REPRESENTATIONS OF THE SOLUTIONS TO THE STOKES EQUATIONS

Theorem 1. *An arbitrary solution to the Stokes equations* (1) *or Eqs.* (2) *that is sufficiently smooth in some domain may be represented in the Cartesian coordinates as*

$$u_i = \frac{4(1-\sigma)}{3-4\sigma}x_m\nabla_i\varphi + x_K\nabla_k\varphi\delta_{im} - x_i\nabla_m\varphi + \nabla_i Q + \varepsilon_{ijq}\nabla_j\psi. \tag{7}$$

where φ, Q, *and* ψ *are harmonic functions of* x; *the indices* m, $q = 1, 2, 3$; *and* ε_{ijq} *is the Levi–Civita antisymmetric tensor.*

Theorem 1 is also valid for the representation

$$u_i = x_m\nabla_i\varphi - (3-4\sigma)\varphi\delta_{im} + \nabla_i Q + \varepsilon_{ijq}\nabla_j\psi. \tag{8}$$

In the case of solutions (7) and (8) to the Stokes equations, the pressure $p = 2\mu\nabla_m\varphi$.

Finally, the theorem also holds for the following representation implied by the first two representations:

$$u_i = 4(1-\sigma)\varphi\delta_{im} + x_k\nabla_k\varphi\delta_{im} - x_i\nabla_m\varphi + \nabla_i Q + \varepsilon_{ijq}\nabla_j\psi. \tag{9}$$

In the case of solution (9) to the Stokes equations, the pressure $p = -2\mu\nabla_m\varphi$.

Formulas (7)–(9) form a class of representations consisting of 27 vector formulas. Arbitrary functions in (7) may be called generalized potentials. Note that the three-dimensional character of representation (7) is essential: there is no simple formula for the plane case.

The first terms in (8) are similar to the terms in the Oberbeck formula or the

Papkovich–Neuber–Grodskiĭ formula (see [9, 10]). The first terms in (9) are similar to the formula in paper [9]. It should be emphasized that formulas (8) and (9) are qualitatively different, due to their last terms, from the formulas in the aforementioned works.

SYMMETRIC EQUATIONS FOR THE VELOCITY FIELD

Write the Stokes equations in a certain domain V in the form

$$\Delta u_i = 2\nabla_i\Pi; \tag{10}$$

$$\mathrm{div}\mathbf{u} + 2(1-2\sigma)\Pi = 0, \quad \mathbf{x}\in V. \tag{11}$$

The pressure $p = 2\mu\Pi$. The equations also correspond to Eqs. (2) for the displacement in an elastic medium.

Consider other field equations within domain V and a particular condition on its boundary ∂V, which is a surface S:

$$\Delta u_i = 2\nabla_i\Pi, \quad \Delta\Pi = 0, \quad \mathbf{x}\in V; \tag{12}$$

$$\mathrm{div}\mathbf{u} + 2(1-2\sigma)\Pi = 0, \quad \mathbf{x}\in S. \tag{13}$$

The following theorem asserts the equivalence of the two ways of describing the field (under the conventional assumptions about the smoothness of the fields on the boundary of the domain and about the smoothness of the boundary).

Theorem 2. *Within a simply connected domain V, equation system* (12) *together with the boundary condition* (13) *are equivalent to the equation system* (10), (11).

According to Theorem 2, the solutions to Eqs. (12) under condition (13) satisfy the source system (the converse statement is obvious).

Equations (12) possess the property of symmetry; namely, they are invariant under a transformation that involves four arbitrary harmonic functions:

$$\Pi' = \Pi + \Phi, \quad u_i' = u_i + x_i\Phi + \varphi_i, \quad \Delta\Phi = 0, \quad \Delta\varphi_i = 0. \tag{14}$$

The field symmetry characterized by the invariant transformation (14) is a property of Eqs. (12), which are valid in the framework of the global description of the field in a certain domain under condition (13) on its boundary.

According to (14), in the general case, the velocity field has the form

$$u_i = \Pi x_i + \nu_i, \quad \Delta\Pi = 0, \quad \Delta\nu_i = 0, \quad \mathbf{x}\in V; \quad \mathrm{div}\mathbf{u} = -2(1-2\sigma)\Pi, \quad \mathbf{x}\in S. \tag{15}$$

By the field equations (12), Π and ν_i are arbitrary harmonic functions.

Particular condition (13) on the boundary surface S should be considered together with the conventional

boundary conditions for the velocities (displacements) or stresses in the statement of boundary-value problems. For the case of a viscous fluid, this means the incompressibility of the fluid on the boundary surface. This condition makes sense, because the flow is not affected by the fluid inertia.

Note that Eqs. (12) or the first formulas in (15) are usually considered [5, 8, 10] together with an equation of the type (11), which precludes a simple symmetric description of the field, and are not treated as the field equations.

A NUMERICAL METHOD BASED ON THE GENERAL REPRESENTATIONS OF THE VELOCITIES AND THE INTEGRAL EQUATION

Denote functions φ, Q, and ψ in representations (7)–(9) by Φ_α, $\alpha = 1, 2, 3$. The components of velocity $\mathbf{u}$ on surface S may be expressed in terms of φ and $\nabla\Phi_\alpha|_S$. In the case of representation (7), they are independent of φ. On surface S, the gradient

$$\nabla|_S = \mathbf{n}\nabla_S + \boldsymbol{\tau}_1\nabla_{l1} + \boldsymbol{\tau}_2\nabla_{l2},$$

where $\boldsymbol{n}$, $\boldsymbol{\tau}_1$, and $\boldsymbol{\tau}_2$ are the unit normal and tangent vectors, and l_1 and l_2 are the lengths of the arcs of orthogonal curves on S. Write the normal and tangent stresses P_n, $P_{\tau1}$, $P_{\tau2}$ in the form of linear functions of $\nabla\Phi_\alpha|_S$, $\nabla_{l1}\nabla\Phi_\alpha$, and $\nabla_{l2}\nabla\Phi_\alpha$.

In the axisymmetric case, for representation (7), we have

$$\begin{aligned} u_n &= 2x_2\nabla_n\varphi + r\nabla_l\varphi + \nabla_n Q; \\ u_\tau &= -r\nabla_n\varphi + 2x_2\nabla_l\varphi + \nabla_l Q; \\ \frac{1}{2\mu}P_\tau &= \frac{\partial u_n}{\partial l} - \frac{u_\tau}{R} + \nabla_r\varphi, \end{aligned} \tag{16}$$

where R is the radius of curvature of the contour of surface S. The normal stress

$$P_n = -p - 2\mu\left(\frac{\partial u_\tau}{\partial l} + \frac{u_n}{R} + \frac{u_r}{r}\right). \tag{17}$$

The pressure $p = 2\mu\nabla_2\varphi$. Stress formulas (16) and (17) are also valid for representation (8). Here, the normal velocity

$$u_n = x_2\nabla_n\varphi - n_2\varphi + \nabla_n Q. \tag{18}$$

In the case of the symmetric description of the field, expression (15) for velocity $\mathbf{u}$ implies the formulas for the velocity components on surface S, tangent and normal stresses:

$$P_n = 2\mu(\Pi(1-2\sigma) + \mathbf{x}\cdot\mathbf{n}\nabla_n\Pi + n_j\nabla_n v_j).$$

In the axisymmetric problem, the components of vector $\mathbf{v}$ can be expressed in terms of two harmonic functions: $v_r = \nabla_r Q$, $v_2 = \nabla_2 Q + f$.

The statement of boundary-value problems for the Stokes equations on separate parts of the boundary surface S usually involves the specification of the velocity

$$u_i = u_i^0, \quad \mathbf{x} \in S_0 \subset S \tag{19}$$

($i = 1, 2, 3$), the surface force

$$p_{ij}n_j = P_i, \quad \mathbf{x} \in S_1 \subset S \tag{20}$$

(p_{ij} is the stress tensor), the normal velocity and the tangent stresses

$$\mathbf{u}\cdot\mathbf{n} = u_n, \quad p_{ij}n_j\tau_{1i} = P_{\tau1}, \quad \mathbf{x} \in S_2 \subset S$$

($P_{\tau2}$ is written in the same way). The representation of the general solution via three harmonic functions or the symmetric description of the field, which involves four functions of this kind, allows us to express the boundary conditions in terms of the values of Φ_α on S and in terms of the normal derivatives $\nabla_n\Phi_\alpha$. To make the equations closed, we need a relation between Φ_α and $\nabla_n\Phi_\alpha$. Such a relation is the integral equation (IE) on the boundary surface

$$4\pi K\Phi(\mathbf{x}) = \iint_S \left\{\frac{1}{r}\frac{\partial\Phi}{\partial n}(\mathbf{x}') - (\Phi(\mathbf{x}') - \Phi(\mathbf{x}))\frac{\partial}{\partial n}\frac{1}{r}\right\}dS, \quad \mathbf{x}, \mathbf{x}' \in S, \tag{21}$$

where $r = |\mathbf{x} - \mathbf{x}'|$, $\mathbf{x}'$ is the integration point. This equation was first introduced in [11] for the cases of plane and axisymmetric problems for the surfaces of several cavities in an unbounded liquid. In these cases, coefficient $K = 1$. The problem being posed inside the closed surface S, coefficient $K = 0$. For an arbitrary case, K is determined via calculation of the right-hand side of the main integral relation for the harmonic function const and subtraction of both sides of the obtained identity and relation. For the plane problem, function r^{-1} in (21) is replaced with $\ln r$ and coefficient 4π is replaced with 2π.

If the flow domain is not simply connected, then, following Kelvin [8], we include the partitions that make this domain simply connected into surface S. Function Φ may have a cyclic constant κ on a partition, namely, the increment of Φ in tracing a closed contour partitioned by the partition. The possible contribution of the integral over the partition to (21) is proportional to the cyclic constant κ. Since all the possible partitions are included in surface S, the form of Eq. (21) is preserved.

The coefficient in the main integral relation of the theory of harmonic functions is known to undergo a

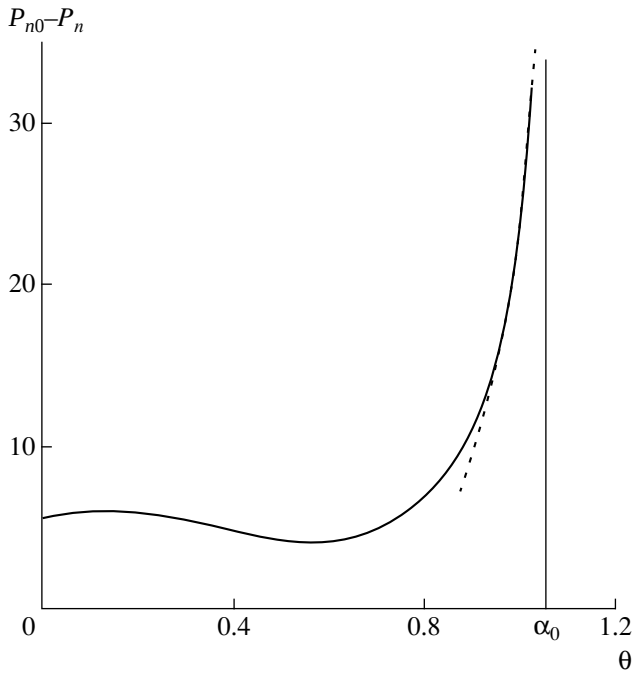

Figure.

jump on S (between close points $\mathbf{x} \notin S$ and $\mathbf{x} \in S$). This jump may be eliminated by subtracting $\Phi(\mathbf{x})$ and $\Phi(\mathbf{x}')$ under the integral sign in (21). Then, the IE may be discretely approximated (by the same scheme) with a much higher accuracy than in the presence of the jump. This is due to the fact that the presence of coefficient $\Phi(\mathbf{x}') - \Phi(\mathbf{x})$ vanishing at $r = 0$ significantly diminishes the impact of the error of approximation of the normal derivative $\nabla_n r^{-1}$ in the close neighborhood of point $r = 0$.

Writing the modified IE (21) for each function Φ_α, together with the boundary conditions on S, we obtain a closed description of the viscous fluid flow.

In the framework of the method, one may also consider operator A of taking the normal derivative, which is defined by IE (21):

$$A(\Phi|_S) = \nabla_n \Phi. \tag{22}$$

With the use of operator A, the normal derivatives $\nabla_n \Phi_\alpha$ may be eliminated from the boundary conditions. As an operator of differentiation, operator A is unbounded.

In the design of numerical algorithms, points of surface S are specified by two parameters, τ and η:

$$\mathbf{x}' = \mathbf{X}(\tau, \eta), \quad \mathbf{x} = \mathbf{X}(\tau_0, \eta_0). \tag{23}$$

Express the singularity of the integrand in (21) in terms of the singularity of the function of the parameters:

$$\frac{1}{r} = \frac{1}{r'} f(\tau, \eta, \tau_0, \eta_0),$$
$$r' = |\mathbf{X}_{\tau 0}(\tau - \tau_0) + \mathbf{X}_{\eta 0}(\eta - \eta_0)|, \tag{24}$$

Here, $\mathbf{X}_{\tau 0}$ and $\mathbf{X}_{\eta 0}$ are the derivatives with respect to τ and η at point τ_0, η_0.

For $r > 0$, the function $f = r' r^{-1}$ in the three-dimensional problem has bounded first derivatives with respect to τ and η. By comparison, note that, in plane and axisymmetric problems [11], transformation (24) with a single parameter τ gives an infinitely differentiable function f in a certain neighborhood of point τ_0 provided that the contour is an analytic curve.

In the two-dimensional problem, substitution (24) replaces the singularity of $\ln r$ with the singularity of $\ln|\tau - \tau_0|$.

Functions Φ and $\nabla_n \Phi$ in (21) are represented by interpolation on a certain number of nodes. For the two-dimensional case, the integrals in the two-dimensional version of (21) are approximated by quadrature formulas with a weight [11]

$$\int_{\tau_1}^{\tau_N} F(\tau) \ln|\tau - \tau_0| d\tau = \sum_{k=1}^{N} c_k F(\tau_k). \tag{25}$$

In three-dimensional problems, we use a similar formula for integration with respect to the parameters with the weight function r'^{-1}.

CALCULATION OF A FLOW WITH A MOVING ANGULAR POINT ON THE BOUNDARY CONTOUR

An axisymmetric flow of a liquid that slowly fills a channel with a circular cross-section, where the free surface is close to a sphere segment intersecting the wall at an angle of α_0, has been calculated. On the sphere, $P_\tau = 0$ and a normal velocity u_n is specified. The velocity on the wall is equal to zero. Away from the sphere, the flow is close to the Poiseuille flow.

In the small neighborhood of the angular point, the problem has been regularized in order that the problem to be calculated have sufficiently smooth boundary conditions. The small neighborhood has a size of 10^{-2} of the channel radius in the example under consideration.

The spacing of the nodes on the contour of the flow boundary S could significantly vary over the boundary, becoming closer near the angular point. The method works even for a gross variation of the grid step (up to 100 times in the case that the total number of nodes is on the order of 100). In the example (figure), the coefficient of the step nonuniformity is 50. The figure shows the difference between the normal stress and its singular part $P_n - P_{n0}$ related to the polar angle θ on the spherical free surface; the contact angle is $\alpha_0 = 30°$. The numerical values of this difference are compared with

the asymptotics near the angular point, according to which the stress

$$P_n = c_1 r^{-1} + c_2 \ln r + \ldots,$$

where the constants are known [14]. The first term P_{n0} is the Taylor stress singularity for a flow in a corner. The values given in Fig. 1 are calculated by the equivalent formula

$$P_n = c_1 \sin\alpha_0 h^{-1} + c_2 \ln h + \ldots,$$

where h is the distance from the wall. It is seen that, near the edge of the spherical segment, the numerical value of the difference between the stresses (the solid line) is close to its asymptotic values (the dotted line). The diagram shows the difference between two values, which are slightly different (about 10%) at the points where the calculations are close to the asymptotic values. The calculated curve is smooth because of the highly accurate calculation of the stress (the error is less than 10^{-3}), which is maintained notwithstanding the strong nonuniformity of the grid.

It is seen in the figure that, subtracting the Taylor singularity from the stress, we do not obtain a bounded function $P_n - P_{n0}$; there is another peak for the stress difference. It is important that both peaks are correctly described by the suggested numerical algorithm.

The numerical calculations employ the symmetric equations for the velocity field with a special boundary condition (13), representation (7) of the velocities via the generalized potentials, and the representation by formula (8). The results obtained by different methods are in good agreement.

The presented calculation results demonstrate that strong nonuniformities of the stress field of a slow flow of a viscous fluid can be calculated with the use of the same integral equation that was used for the calculation of the dynamics of an ideal liquid with a free boundary [11–13].

REFERENCES

1. S. Weinbaum, P. Ganatos, and Z.-Y. Yan, Annu. Rev. Fluid Mech. **22**, 275 (1990).
2. S. Kim and H. Power, J. Fluid Mech. **257**, 637 (1993).
3. D. M. Koch and D. L. Koch, J. Fluid Mech. **287**, 251 (1995).
4. N. I. Muskhelishvili, *Some Basic Problems of Mathematical Theory of Elasticity* (Nauka, Moscow, 1966) [in Russian].
5. J. Happel and H. Brenner, *Low Reynolds Number Hydrodynamics* (Prentice-Hall, Englewood Cliffs, 1965; Mir, Moscow, 1976).
6. V. I. Blokh, *Theory of Elasticity* (Kharkov Gos. Univ., Kharkov, 1964) [in Russian].
7. A. Oberbeck, J. Reine Angew. Math. **81**, 62 (1876).
8. H. Lamb, *Hydrodynamics*, 6th ed. (Cambridge University Press, Cambridge, 1932; Gostekhizdat, Moscow, 1947).
9. M. G. Slobodyanskiĭ, Prikl. Mat. Mekh. **18**, 55 (1954).
10. W. Nowacki, *Teoria sprężystości* (PWN, Warszawa, 1970; Mir, Moscow, 1975).
11. O. V. Voinov and V. V. Voinov, Dokl. Akad. Nauk SSSR **221** (3), 559 (1975) [Sov. Phys. Dokl. **20** (3), 179 (1975)].
12. O. V. Voinov and V. V. Voinov, Dokl. Akad. Nauk SSSR **227** (1–3), 63 (1976) [Sov. Phys. Dokl. **21** (3), 133 (1976)].
13. O. V. Voinov, Prikl. Mekh. Tekh. Fiz., No. 3, 94 (1979).
14. O. V. Voinov, Dokl. Akad. Nauk **394** (2), 473 (2004) [Dokl. Phys. **49** (2), 95 (2004)].

Translated by A. Pankrat'ev

Doklady Physics, Vol. 50, No. 12, 2005, pp. 668–670. Translated from Doklady Akademii Nauk, Vol. 405, No. 6, 2005, pp. 765–767.

MECHANICS

Stability of Two-Dimensional Solitons and the 2D–3D Transition in a Viscous Liquid Film Falling Down on a Vertical Wall

E. N. Kalaidin[1], S. Yu. Vlaskin[1,*], E. A. Demekhin[1], and S. Kalliadasis[2]

Presented by Academician G.G. Chernyi April 4, 2005

Received June 24, 2005

The mechanism of the transition from two-dimensional (2D) waves to a 3D wave regime in a viscous liquid film falling down on a vertical wall has been elucidated for the first time. The linear stability of 2D solitons with respect to 3D perturbations is analyzed. The decomposition of solitary waves and their transformation into localized wave structures is described using numerical methods. The proposed physical mechanism of 2D solitary wave breakage is related to the destabilizing action of capillary forces in the transverse direction and to the development of a Rayleigh instability, which leads to the decomposition of capillary streams.

1. The 3D flow in a thin liquid film falling down on a vertical wall at moderate Reynolds numbers is described by the Kapitza–Shkadov system of equations [1–3]:

$$\frac{\partial q}{\partial t} + \frac{6}{5}\frac{\partial}{\partial x}\frac{q^2}{h} + \frac{6}{5}\frac{\partial}{\partial z}\frac{qp}{h} = \frac{1}{5\delta}\left\{h\left(\frac{\partial^3 h}{\partial x^3} + \frac{\partial^3 h}{\partial x \partial z^2}\right) + h - \frac{q}{h^2}\right\},$$

$$\frac{\partial p}{\partial t} + \frac{6}{5}\frac{\partial}{\partial x}\frac{qp}{h} + \frac{6}{5}\frac{\partial}{\partial z}\frac{p^2}{h} = \frac{1}{5\delta}\left\{h\left(\frac{\partial^3 h}{\partial x^2 \partial z} + \frac{\partial^3 h}{\partial z^3}\right) - \frac{p}{h^2}\right\}, \quad (1)$$

$$\frac{\partial h}{\partial t} + \frac{\partial q}{\partial x} + \frac{\partial p}{\partial z} = 0,$$

where q and p are the liquid flow rates along the gravity force (x axis) and in the normal (z axis) directions, respectively; h is the film thickness; $\delta = \dfrac{\mathrm{Re}^{11/9}}{5\gamma^{1/3}\cdot 3^{7/9}}$ is the modified Reynolds number; Re is the flow-rate-average Reynolds number; $\gamma = \sigma\rho^{-1}\nu^{-4/3}g^{-1/3}$ is the Kapitza number; σ, ρ, and ν are the surface tension, density, and kinematic viscosity of the liquid, respectively; and g is the acceleration of gravity.

System (1) has a one-parametric family of solutions of the 2D soliton type [4]:

$$p = \frac{\partial}{\partial z} = 0, \quad \frac{\partial}{\partial t} = -c\frac{\partial}{\partial x}, \quad q_0 = ch_0 - c + 1,$$

for which $h_0 \longrightarrow 1$ for $x \longrightarrow \pm\infty$ [infinity]. These solitons, which appear due to random perturbations arising at the input and evolving downstream [5], have been observed in experiment [6, 7]. In the case of relatively large Reynolds numbers and sufficiently long channels, the 2D solitons exhibit disintegration with the formation of 2D localized structures [8, 9].

Let us impose a small perturbation on the above 2D soliton-type solution:

$$h = h_0(\xi) + \hat{H}(\xi)e^{i\beta z + \lambda t},$$

$$q = q_0(\xi) + \hat{Q}(\xi)e^{i\beta z + \lambda t}, \quad (2)$$

$$p = i\hat{P}(\xi)e^{i\beta z + \lambda t}, \quad \xi = x - ct.$$

Substituting expressions (1) into Eq. (1) and linearizing the obtained relations, we obtain a boundary-value problem for determining the eigenvalues λ:

$$\lambda\hat{Q} + \frac{d}{d\xi}\left(\frac{12}{5}\frac{q_0}{h_0}\hat{Q} - \frac{6}{5}\frac{q_0^2}{h_0^2}\hat{H} - c\hat{Q}\right) - \frac{6}{5}\beta\frac{q_0}{h_0}\hat{P}$$

$$= \frac{1}{5\delta}\left\{h_0\frac{d^3\hat{H}}{d\xi^3} + h_0'''\hat{H} - \beta^2 h_0\frac{d\hat{H}}{d\xi} + \hat{H} - \frac{1}{h_0^2}\hat{Q} + \frac{2q_0}{h_0^3}\hat{H}\right\},$$

[1] *Southern Scientific Center, Russian Academy of Sciences, Krasnodar, Russia*

[2] *Chemical Engineering Department, Empyreal College, London, UK*

* *e-mail: vlaskin@bk.ru*

1028-3358/05/5012-0668$26.00

$$\lambda\hat{P} + \frac{d}{d\xi}\left(\frac{6}{5}\frac{q_0}{h_0}\hat{P} - c\hat{P}\right)$$
$$= \frac{1}{5\delta}\left\{\beta h_0 \frac{d^2\hat{H}}{d\xi^2} - \beta^3 h_0 \hat{H} - \frac{1}{h_0^2}\hat{P}\right\}, \quad (3)$$
$$\lambda\hat{H} + \frac{d}{d\xi}(\hat{Q} - c\hat{H}) - \beta\hat{P} = 0,$$

where $\hat{H}, \hat{Q}, \hat{P} \longrightarrow 0$ for $\xi \longrightarrow \pm\infty$.

At $\xi \longrightarrow \pm\infty$, the system of equations (3) transforms into a system with constant coefficients, which has solutions of the type $\exp(\sigma x)$, where σ are determined by the dispersion relation

$$(\sigma^4 + ((5c^2 - 12c + 6)\delta - 2\beta^2)\sigma^2$$
$$+ (3 - 10\lambda c\delta + 12\lambda\delta - c)\sigma + 5\lambda^2\delta + \lambda + \beta^4)$$
$$\times((6 - 5c)\delta\sigma + 5\lambda\delta + 1) = 0.$$

Three σ_k correspond to the components with $\mathrm{Re}\{\sigma_k\} > 0$, which decay at $\xi \longrightarrow -\infty$ and yield the solution

$$A_1\exp(\sigma_1 x) + A_2\exp(\sigma_2 x) + A_3\exp(\sigma_3 x).$$

System (3) was numerically integrated from these initial conditions to a region of large $\xi > 0$, which corresponds to the asymptotics at $\xi \longrightarrow +\infty$. This region is described using the remaining two σ_k values with $\mathrm{Re}\{\sigma_k\} < 0$, which decay at $\xi \longrightarrow +\infty$ and yield the solution

$$B_1\exp(\sigma_4 x) + B_2\exp(\sigma_5 x).$$

It was found that, for all δ values, there is a single unstable real eigenvalue $\lambda(\beta)$. In a small vicinity of $\beta = 0$, we have $\lambda = 0$. As β increases, λ grows, passes through a maximum (λ_m at $\beta = \beta_m$), decays to zero at $\beta = \beta_0$, and goes to a stable region of $\lambda < 0$.

Figure 1 shows the plots of β_m and λ_m versus δ. For $\delta \longrightarrow 0$, the problem has an asymptotic solution with $\beta_m \longrightarrow 0.3255(15\delta)^{1/2}$, $\lambda_m \longrightarrow 0.0545(15\delta)^2$, and $\beta_0 \longrightarrow 0.4758(15\delta)^{1/2}$ (dashed lines in Fig. 1). For sufficiently large δ values, the solution exhibits a different asymptotic behavior, which corresponds to $\beta_m \longrightarrow 0.361$, $\lambda_m \longrightarrow 0.2382$, and $\beta_0 \longrightarrow 0.832$.

The recalculation from β_m to a dimensional quantity for water ($\gamma = 2850$) yields an estimate of the most "dangerous" wavelength: $1.42\mathrm{Re}^{1/9}$. For $\mathrm{Re} = 5$–80, this wavelength is on the order of 2 cm, which is in good agreement with experiment [7, 8, 9]. Taking into account that the initial perturbation amounts to 5–10% of the soliton amplitude, the distance traveled by a 2D soliton downstream until its complete disintegration is

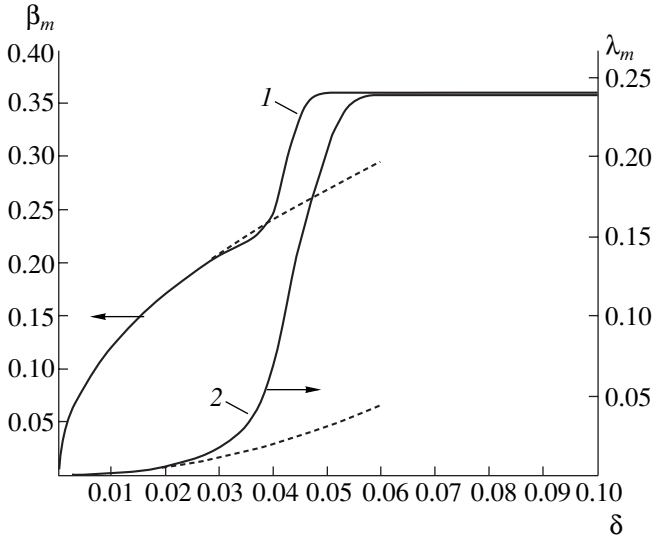

Fig. 1. The plots of (*1*) β_m and (*2*) λ_m versus δ. Dashed lines show the asymptotic behavior for small δ.

$6\mathrm{Re}^{1/9}$. This value also rather weakly depends on the Reynolds number and is on the order of 10 cm [7, 8, 9].

2. We have integrated system (1) using numerical methods. The initial conditions corresponded to a 2D soliton perturbed with respect to z:

$$h = h_0(x - ct) + e^{-bx^2}\sum_{k=1}^{N} A_k\cos(k\beta z),$$
$$q = ch - c + 1, \quad p = 0,$$

where A_k and b are constants. The calculations were performed for $N = 100$, $A_k = 10^{-9}$, and $\beta = \frac{\beta_0}{100}$, which corresponded to a small random noise imposed on the 2D solution. A solution was found in a rectangular domain $x = \pm l$, $z = \pm\frac{\pi}{\beta}$. The boundary conditions at $x = \pm l$ were selected in the form of $h = q - ch = 1$, $p = 0$; the boundary conditions with respect to z were periodic:

$$h(x, z) = h\left(x, z + \frac{2\pi}{\beta}\right), \quad q(x, z) = q\left(x, z + \frac{2\pi}{\beta}\right),$$
$$p(x, z) = p\left(x, z + \frac{2\pi}{\beta}\right).$$

The solution was obtained by the high-order finite difference (lattice-point) method in a coordinate system moving at a 2D soliton velocity, with an implicit finite difference scheme in the time domain.

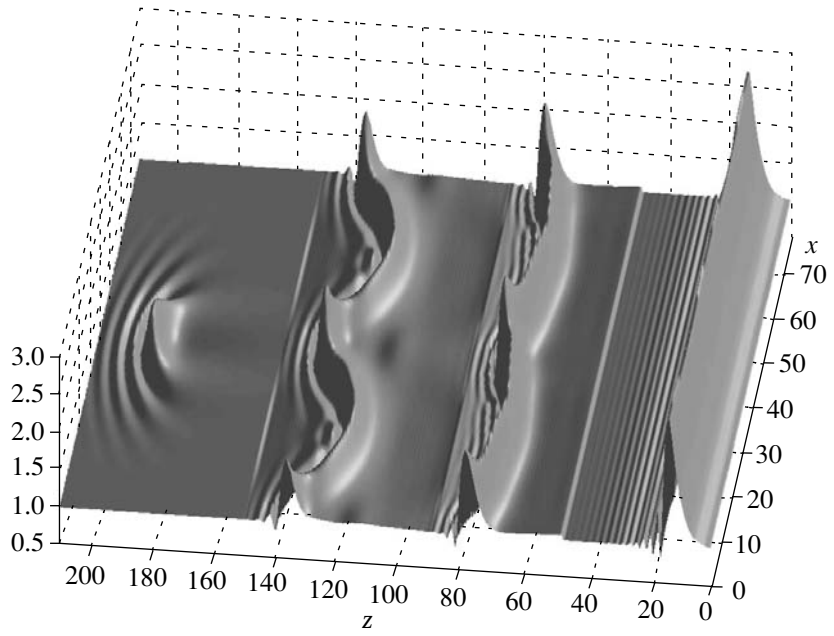

Fig. 2. Decomposition of a 2D soliton with the formation of 3D solitons ($\delta = 0.05$).

The results of our calculations showed that, for $\delta < \delta_* \simeq 0.05$–$0.07$ (for water, this corresponds to $\mathrm{Re}_* \simeq 6$), 2D solitons do not exhibit complete disintegration and the signal acquires a stationary quasi-2D shape slightly curved in the z direction. For $\delta > \delta_* \simeq 0.05$, a Rayleigh instability is developed that leads to the complete decomposition of 2D solitons with the formation of 3D solitons (Fig. 2).

ACKNOWLEDGMENTS

This study was supported by INTAS (grant no. 99-1107).

REFERENCES

1. V. Ya. Shkadov, Izv. Akad. Nauk SSSR, Mekh. Zhidk. Gaza, No. 1, 43 (1967).
2. V. Ya. Shkadov, Izv. Akad. Nauk SSSR, Mekh. Zhidk. Gaza, No. 2, 20 (1968).
3. E. A. Demekhin and V. Ya. Shkadov, Mekh. Zhidk. Gaza, No. 5, 21 (1984).
4. E. A. Demekhin and V. Ya. Shkadov, Mekh. Zhidk. Gaza, No. 3, 63 (1985).
5. H.-C. Chang, E. A. Demekhin, and E. N. Kalaidin, AIChE J. **42** (6), 1553 (1996).
6. P. L. Kapitza and S. P. Kapitza, Zh. Éksp. Teor. Fiz. **19** (2), 105 (1949).
7. S. V. Alekseenko, V. E. Nakoryakov, and B. G. Pokusaev, Prikl. Mekh. Tekh. Fiz., No. 6, 77 (1979).
8. S. R. Tailby and S. Portalski, Trans. Inst. Chem. Eng., No. 38, 324 (1960).
9. C. D. Park and T. Nosoko, AIChE J. **49** (11), 2715 (2003).

Translated by P. Pozdeev